Investigation of Innovative Scintillating Nanomaterials featuring very fast Timing with potential Applicability in Calorimetry

Isabel Julia Christine Frank

Munich 2024

Investigation of Innovative Scintillating Nanomaterials featuring very fast Timing with potential Applicability in Calorimetry

Dissertation
an der Fakultät für Physik
der Ludwig–Maximilians–Universität
München

vorgelegt von
Isabel Julia Christine Frank
aus Hanau

München, den 22. April 2024

"Everything is possible. The impossible just takes longer."

<div style="text-align: right;">– Dan Brown, Digital Fortress</div>

Zusammenfassung

Teilchendetektoren werden in Experimenten in der Hochenergiephysik zur Identifikation von Teilchen und der Suche nach neuer Physik eingesetzt. Für zukünftige Experimente werden Detektoren mit hoher Zeitauflösung benötigt, um mit dem hohen Eventaufkommen umgehen zu können und die Fähigkeiten der Teilchenidentifikation zu verbessern. Szintillierende Kristalle finden traditionell Anwendung sowohl in homogenen als auch in sogenannten sampling Kalorimetern. In den letzten Jahren wurden bedeutende Fortschritte im Bereich szintillierender Materialien erzielt, insbesondere im Hinblick auf die Entwicklung von neuartigen und innovativen Materialien mit schnellen Lichtemissionsprozessen. Diese Forschung und Entwicklung ist entscheidend, um die anspruchsvollen Anforderungen an künftige Detektoren zu erfüllen, die für Collider mit hoher Luminosität entwickelt werden und wo außergewöhnliche Strahlenbeständigkeit und ultraschnelles Timing erforderlich sind. Halbleiternanostrukturen basierend auf Quantenpunkten zeigen aufgrund von Quanteneffekten ein hohes Potenzial für die Emission von prompten Photonen und zeichnen sich durch kostengünstigere Produktion aus, was das Interesse im Bereich der Hochenergiephysik weckt. Diese Nanomaterialien sind bereits in verschiedenen Bereichen zu finden und sind für Anwendungen in Solarzellen, LEDs, Displays und Lasern bekannt, jedoch weniger in Bezug auf ihre Verwendung als Szintillationsdetektoren. Das Ziel dieser Arbeit ist es, das Potenzial dieser innovativen szintillierenden Nanomaterialien zu untersuchen, wobei ein besonderer Schwerpunkt auf hohe Zeitauflösung und auf ihrer Verwendungbarkeit in zukünftigen Kalorimetern liegt. In dieser Arbeit werden szintillierende Nanomaterialien hinsichtlich ihrer optischen Eigenschaften, ihres Szintillationsverhalten und ihrer Lichtausbeute detailiert untersucht. Sie zeigen Photonenabklingzeiten im subnanosekunden Bereich und sind vereinzelt bereits durch ihre exzellente Zeitauflösung und hohe Lichtausbeute wettbewerbsfähig mit konventionellen Plastikszintillatoren. Allerdings haben viele dieser Nanomaterialien immer noch eine zu geringe Absorptionsfähigkeit und Konvertierbarkeit, damit einhergehend eine zu geringe Lichtausbeute, und damit eine einschränkte Verwendbarkeit in der Kalorimetrie. Zur Charakterisierung solcher Materialien, die sich durch geringe Absorptionsfähigkeit, aber ultraschnelle Szintillation auszeichnen, wurde eine Charakterisierungsmethode mit Röntgenstrahlen entwickelt. Vielversprechende Nanomaterialien wurden mit dem Fokus auf ihre Zeitauflösung auch unter Bestrahlung mit hochenergetischen Teilchen untersucht, um ihre mögliche Anwendbarkeit in der Kalorimetrie abzuschätzen. Im Rahmen des AIDAinnova Blue Sky Projekts "NanoCal" wurden erste Kalorimeter-Prototypen unter Verwendung dieser innovativen Nanomaterialien auf Basis von Perowskit Nanokristallen entwickelt. Erste Messungen mit hochenergetischen Teilchen wurden durchgeführt um ihre Leistungsfähigkeit im Vergleich zu herkömmlich verwendeten Szintillatoren zu erforschen.

.

Abstract

Particle detectors are commonly used in high energy physics experiments for the identification of particles and the search for new physics. For future particle physics experiments, fast timing detectors are needed to cope with high event pileup and to enhance particle identification capabilities.

Scintillating crystals are often used in both homogeneous and sampling calorimeters. In recent years, significant progress has been made in the development of scintillators, particularly novel and innovative materials, exhibiting fast light emission. This ongoing R&D is crucial to meet the demands of future detectors designed for high luminosity colliders, where exceptional radiation tolerance and ultra-fast timing are required.

Direct band gap engineered semiconductor nanostructures show a high potential for the emission of prompt photons due to quantum confinement, standing out for their low-cost production and thus also triggering interest in the high energy physics community. These nanomaterials can already be found in various fields and are well known for applications in solar cells, LEDs, displays and lasers, but less in terms of their use as scintillation detectors. The objective of this work is to investigate the potential of these interesting scintillating nanomaterials with particular focus on fast timing and their applicability in future calorimetry.

In this work scintillating nanomaterials are investigated in terms of their optical and scintillation properties, timing and light output. They show photon emission decay times in the subnanosecond range and are in some cases already competitive with conventional plastic scintillators. Although these nanomaterials are characteristic for their very fast timing, many of these materials still have low stopping power and low light output, which limits their use in calorimetry. For the evaluation of such scintillating materials new characterization method was investigated using X-rays. Promising nanomaterials were also explored in terms of timing under high energy particle irradiation to investigate their applicability in calorimetry. As part of the AIDAinnova Blue Sky project "NanoCal", first calorimeter prototypes were developed at low cost using these interesting nanomaterials based on perovskite nanocomposites. First measurements were made with these prototypes under high energy particle irradiation to access their performance in comparison with conventionally used scintillators.

.

Contents

Particle detectors are central in the identification of particles and the search for new physics. To meet the challenges posed by the expected increase in particle flux at future particle physics experiments, future particle detectors rely on fast timing and radiation resistant detectors to cope with high event pileup and to enhance particle identification capabilities, as illustrated in Figure 1.1.

Scintillating crystals are traditionally found in high energy physics experiments and are used in both homogeneous and sampling calorimeters. Standard inorganic scintillators, due to their high density, are often used in large homogeneous calorimeters, where they serve simultaneously as converter and active detector medium. Some are radiation hard and can provide both high light efficiency and fast light emission, resulting in optimal energy resolution. However, these materials are very costly.
Organic scintillators, such as plastic scintillators, can be an alternative and are more competitive in terms of costs. They can provide relatively high light output and fast timing, but they are not particularly radiation hard. Due to their lower density and thus lower energy resolution, they are typically used in sampling calorimeters.
In recent years, significant progress has been made in scintillator R&D, particularly with regard to novel, fast light emission processes and innovative materials.

Figure 1.1: Pileup events per bunch crossing in proton-proton collisions at the CERN LHC. The number of individual proton-proton collisions in each event increases with increasing luminosity. Figure from Groom et al. [1].

CERN: European Organisation for Nuclear Research. The acronym CERN comes from "Conseil Européen pour la Recherche Nucléaire".

LHC: Large Hadron Collider

R&D: Research and Development

Nanomaterials

The nanoworld, illustrated in Figure 1.2, is limited by the size of the nanoparticles, ranging from 1 to 100 nm. Nanocrystals are tiny crystals of metals, semiconductors, insulators, and magnetic materials, whose properties and band structures can be described as the quantum mechanical coupling of over hundreds to thousands of atoms.
Direct band gap engineered semiconductor nanostructures show a high potential for the emission of prompt photons due to quantum confinement, leading to size dependent and tunable optoelectronic properties and ultra-fast timing.
Scintillating nanomaterials can already be found in various fields and are well known for applications in solar cells, LEDs, displays and lasers, but less in terms of their use for scintillation detectors. Their excellent luminescent properties such as high quantum efficiency, narrow emission bands and fast decay times are ideal prerequisites for scintillation detectors with a particular focus on their specific size-dependent and tunable properties that may be significantly different from the physical properties of their solid state bulk counterparts. However, a persistent challenge is to exploit their promising optoelectronic properties in a complete detector in view of their size and instability. Embedding nanocrystals in solid matrices such as organic polymers can provide the required stability and lead to nanoscintillators with very fast timing.
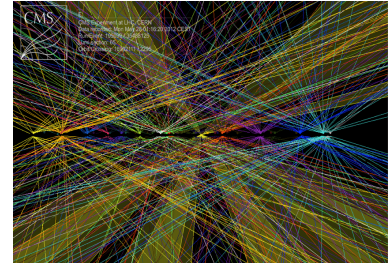
This work focuses on the investigation of innovative scintillating nanomaterials featuring very fast timing with potential application in calorimetry.
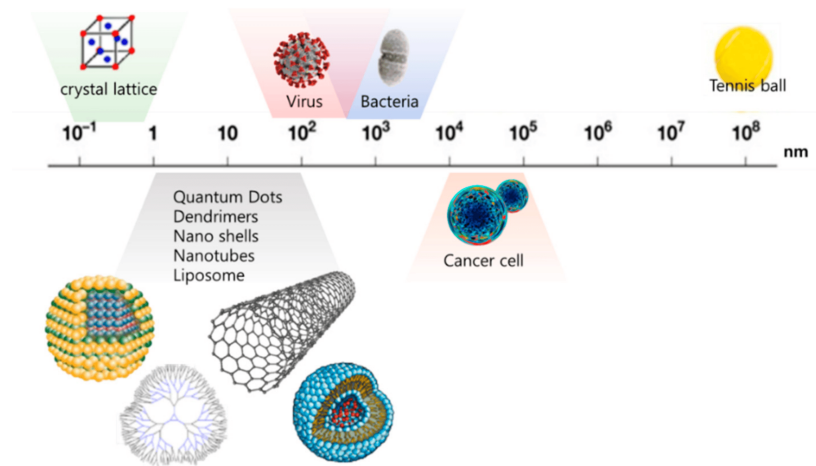

Figure 1.2: Illustration for classifying the size of nanomaterials, whereby there are different nanostructures. Quantum dot are the most important example of zero-dimensional nanostructures. Figure from Min et al. [2].

On the Content of this Thesis

The relevant topics of this work, discussed in the different chapters, are discussed below.

Chapter 2 – Theoretical Background
The principle and the underlying processes of the interaction of charged particles and photons with matter are described. The chapter also gives an introduction to calorimetry in particular electromagnetic calorimetry. The chapter concludes with a description of sampling and homogeneous electromagnetic calorimeters.

Chapter 3 – Scintillation and Scintillators
General characteristics and properties of scintillating materials are presented. The chapter gives a brief introduction to inorganic and organic scintillators, and their different scintillation mechanisms are explained. Scintillation characteristics such as photoluminescence, light transmission and absorption, light yield and light output, as well as the scintillation kinetics and time resolution are explained.

Chapter 4 – Nanomaterials
The chapter addresses scintillating nanomaterials with focus on fast timing and high light yield and also with the view to production costs. This chapter briefly asses the suitability of these materials in high energy physics and medical applications. Semiconductor nanocrystals are introduced. Quantum confinement leads to their size-dependent tunable optoeclectronic properties. Scintillating nanocomposites are proposed as ultrafast scintillators. The chapter concludes with a description of the studied nanoscintillators and their manufacture.

Chapter 5 – Characterization Methods
Tools and methods for the characterization of nanomaterials are presented. The chapter also gives a brief overview of the readout electronics used for very high-resolution time measurements, followed by a description of the functional principles of photodetectors such as photomultiplier

tubes (PMTs) and silicon photomultipliers (SiPMs). The measurement setups and analysis techniques are explained in detail. This comprises their optical properties such as photoluminescence, radioluminescence and transmission, their light yield with gammas, as well as their timing performance with X-rays, such as scintillation kinetics and time resolution.

Chapter 6 – Characterization Results
The chapter presents the evaluation results of the individual, studied nanoscintillators and concludes with a summary and discussion of all results. It also gives an outlook for possible applications of these materials in calorimetry.

Chapter 7 – Nanomaterials in Calorimetry
Possible applications of nanomaterials in calorimetry are presented. A new concept of using these materials in a so-called chromatic calorimeter is explained, followed by measurement in terms of time performance measured with high energy particles. The measurement setups and analysis techniques are explained in detail, followed by results of these measurements. Furthermore the so-called NanoCal project, a part of the European Union's Horizon 2020 Research and Innovation programme (AIDAinnova) is introduced. In the frame of this project shashlik calorimeter prototypes using nanomaterials were constructed, and first measurements made in testbeams at CERN.

Chapter 8 – Summary and Outlook
The work concludes with a summary and conclusion with an outlook on the applicability of nanomaterials in calorimetry. It addresses also the limitation of this concept and motivate research interests for further developments.

Theoretical Background | 2
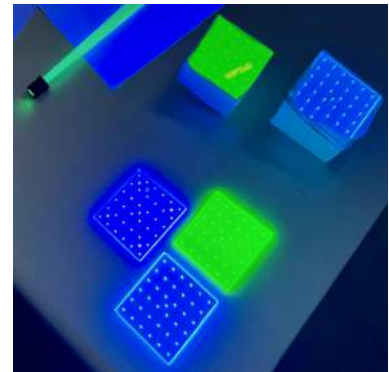
In this chapter the underlying physics processes of particle interaction with matter are described.

2.1 Particle Interaction with Matter

Charged Particles

Charged particles ionize the medium in which they travel. The mean energy loss per unit distance is described by the Bethe-Bloch formula [3], given by

$$\left\langle -\frac{dE}{dx} \right\rangle = K z^2 \frac{Z}{A} \frac{1}{\beta^2} \left(\frac{1}{2} \ln \frac{2 m_e c^2 \beta^2 \gamma^2 W_{max}}{I^2} - \beta^2 - \frac{\delta(\beta\gamma)}{2} \right), \quad (2.1)$$

with constants and variables listed in Table 2.1. An illustration of the mean energy loss of muons in copper is shown in Figure 2.1.

Variable	Value	Description
K	$4\pi N_A r_e^2 m_e c^2$	constant
r_e		classical electron radius
m_e		electron mass
c		speed of light
N_A		Avogadro number
Z		atomic number of the target material
A		atomic mass of the target material
z		charge number of the incident particle
β	v/c	velocity of the incident particle
γ	$1/\sqrt{1-\beta^2}$	Lorentz factor
I		mean excitation energy of the target material
W_{max}	$2 m_e c^2 \beta^2 \gamma^2$	maximum possible energy transferable to an electron in a single collision
$\delta(\beta\gamma)$		density effect correction to ionization energy loss

Table 2.1: Constants and variables for calculating the mean energy loss in Equation 2.1 according to Bethe-Bloch [3].
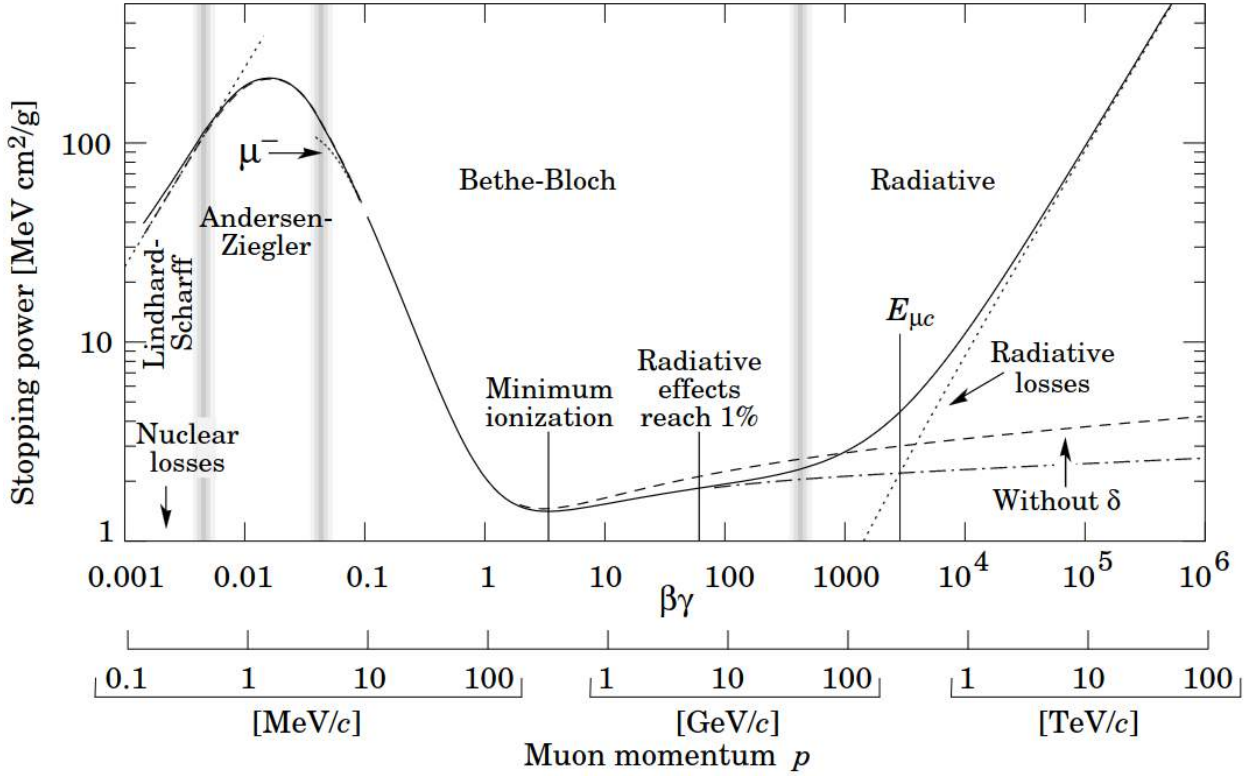
Figure 2.1: Mean energy loss $\langle -dE/dx \rangle$ for positive muons in copper as a function of $\beta\gamma$ and momentum p. Figure from Groom et al. [4].

At low energies electrons and positrons primarily lose energy by ionization, and the energy loss increases logarithmically with energy:

$$\left\langle -\frac{dE}{dx} \right\rangle_{\text{ionization}} \propto \log(E) \,, \tag{2.2}$$

where E is the electron energy.

At higher energies, above the critical energy, bremsstrahlung[1] becomes the most dominant interaction, and the energy loss increases linearly:

$$\left\langle -\frac{dE}{dx} \right\rangle_{\text{brems}} \propto E \,. \tag{2.3}$$

The energy loss per radiation length in lead is shown in Figure 2.2.

The critical energy E_c is often defined as the energy where both the energy loss by ionization and the loss by bremsstrahlung are equal:

$$\left\langle -\frac{dE}{dx} \right\rangle_{\text{ionization}} = \left\langle -\frac{dE}{dx} \right\rangle_{\text{brems}} \,. \tag{2.4}$$

On the other hand, Rossi [5] defines it as the energy per radiation length X_0 at which the ionization loss is equal to the electron energy E:

$$\left\langle -\frac{dE}{dx} \right\rangle_{\text{ionization}} \approx \frac{E}{X_0} \,. \tag{2.5}$$

1: Bremsstrahlung is an electromagnetic radiation produced by the sudden deceleration or deflection of charged particles (especially electrons) near the strong electric fields of atomic nuclei as they pass through matter.

The difference of both definitions is shown in Figure 2.3. As shown both definitions converge at high energies where the ionization losses become negligible. Nevertheless, the critical energy is relevant for applications in calorimeter as it determines the transition from bremsstrahlung to ionization loss at the end of a shower cascade.
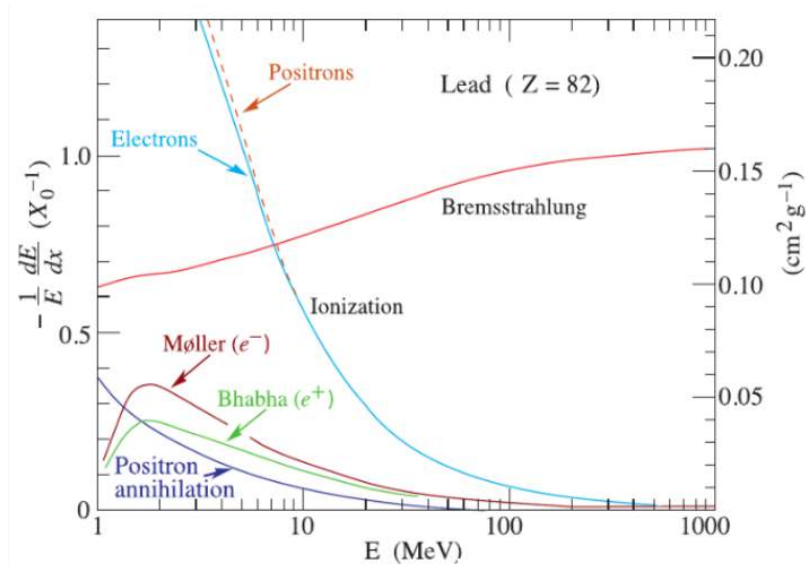
Figure 2.2: Energy loss per radiation length in lead as a function of energy for electrons and positrons, where ionization is the dominant interaction at low energies, although other processes (Møller scattering, Bhabha scattering, e^+ annihilation) occur and bremsstrahlung becomes the most dominant interaction at higher energies. Figure from Workman et al. [3].
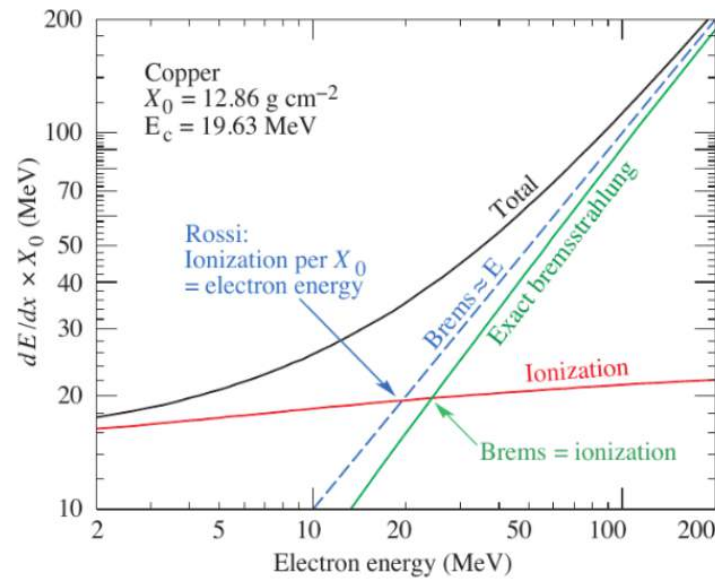
Figure 2.3: Two definitions of the critical energy. One in which the energy loss by ionization is equal to the loss by bremsstrahlung, and the second according to Rossi, in which the energy loss by ionization per radiation length is equal to the electron energy. Figure from Workman et al. [3].

Photons

The interaction mechanism of photons, which neither carry electric charge nor have a mass, is completely different from charged particles. Photons either interact with matter and are lost or re-emitted at lower energy, or scattered out, or do not interact at all.

The energy E of a photon [3] is given by

$$E = h \cdot \nu = \frac{h \cdot c}{\lambda} \qquad \text{with} \qquad \nu = \frac{c}{\lambda} \, , \tag{2.6}$$

where ν is the frequency, λ the wavelength and h the Planck constant.

The interaction of photons with matter is dominated by three main mechanisms, depending on the energy of the photon: Photoelectric effect, Compton scattering and pair production, as shown in Figure 2.4.

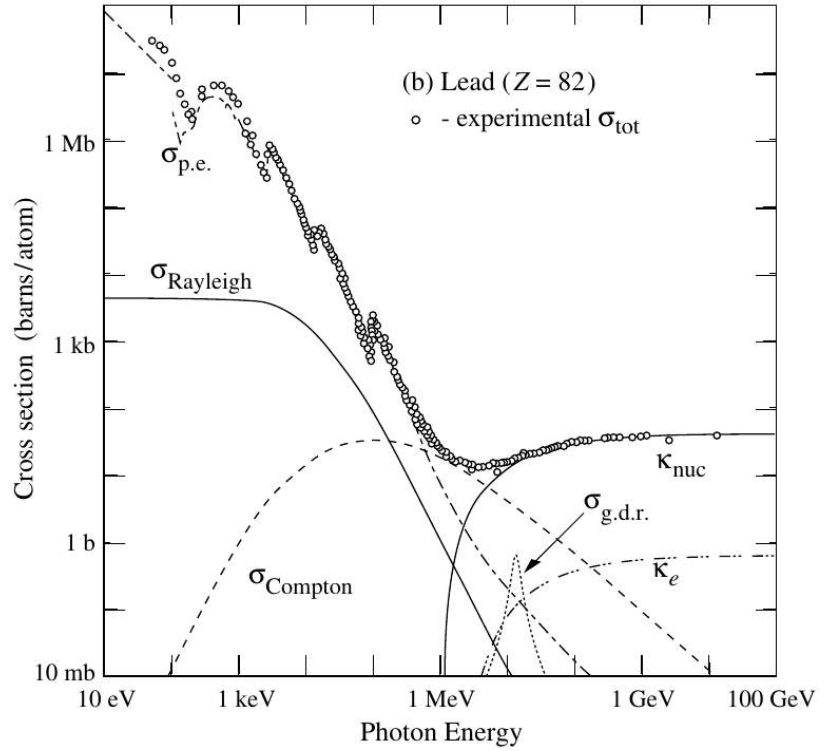**Figure 2.4:** Photon interaction cross sections in lead as a function of energy, where $\sigma_{\text{p.e.}}$ denotes the photoelectric effect, σ_{Rayleigh} the Rayleigh coherent scattering, and σ_{Compton} the Compton scattering. Whereas κ_{nuc} and κ_{e} describe the pair production probability in the presence of a nuclear field and electron field, respectively, and $\sigma_{\text{g.d.r.}}$ resonant photonuclear interactions leading to the break up of the nucleus. Figure Workman et al. [3].

The Photoelectric effect is the absorption of a photon by an atom, accompanied by the release of a shell electron, and dominates the interaction cross section at low photon energies up to a few hundreds of keV.

The emitted electron energy E_{e} is given by

$$E_{\text{e}} = E_\gamma - E_{\text{b}} \, , \tag{2.7}$$

where E_γ is the energy of the photon and E_{b} the binding energy of the electron.

The Compton effect can be interpreted as elastic scattering of a photon by an electron, as illustrated in Figure 2.5. From the conservation of energy and momentum, the energy of the scattered photon can be calculated as

Figure 2.5: Illustration of the Compton scattering.

$$E'_\gamma = \frac{E_\gamma}{1 + (1 - \cos\theta)E_\gamma / m_{\text{e}}c^2} \, , \tag{2.8}$$

where θ is the scattering angle.

The scattered electron thus has a maximum kinetic energy $W'_{e,\mathrm{max}}$ of

$$W'_{e,\mathrm{max}} = E_\gamma \cdot \frac{2E_\gamma/m_e c^2}{1 + 2E_\gamma/m_e c^2} , \tag{2.9}$$

which leads to the so called Compton edge in the energy spectrum.

Electron pair production becomes the dominant interaction once the photon energy exceeds $E_\gamma \geq 2m_e c^2$, where a photon can create an electron-positron pair in the proximity of a nucleus or electron coulomb field. The total cross section can be approximated by [3]

$$\sigma = \frac{7}{9} \frac{A}{X_0 N_A} , \tag{2.10}$$

where A is the atomic mass, X_0 the radiation length in $\mathrm{g\,cm^{-2}}$ and N_A the Avogadro number.

Radiation Length

The radiation length X_0 is a characteristic of a material, related to the energy loss of high energy particles electromagnetically interacting with it. It is defined as the average travel length into the material at which the energy of an electron is reduced to $\frac{1}{e}$ (to about 36.8 %) due to bremsstrahlung and for a photon to $\frac{7}{9}$ of the average travel length for pair production, usually expressed in $\mathrm{g\,cm^{-2}}$. It can be parameterized as [3]

$$X_0 = \frac{716.4\,A}{Z(Z+1)\ln\left(287/\sqrt{Z}\right)} , \tag{2.11}$$

where Z is the atomic number and A mass number of the nucleus.

The radiation length is a crucial parameter in particle physics experiments to describe and characterize the interactions of high-energy electrons and photons passing through matter. It is particularly important for the development of calorimeters in particle experiments.

Electromagnetic Shower

High-energy electrons or photons incident on a dense absorber produce an electromagnetic cascade, called shower, in which further electrons and photons with lower energy are generated via bremsstrahlung and pair production. The process continues for photons until their energy falls below the threshold for pair production. When the electron energy falls below the critical energy, the electrons release their energy by ionization and excitation, rather than by creating more shower particles. Figure 2.6 illustrates the development of an electromagnetic shower initiated by an electron.
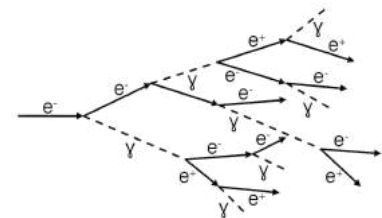

Figure 2.6: Illustration of an electron initiated electromagnetic shower.

The longitudinal development of a shower is determined by the high-energy part of the cascade and therefore scales with the radiation length X_0 of the absorber. Figure 2.7 shows the longitudinal shower profile for electron showers in copper at different energies.

Figure 2.7: Longitudinal shower profile for electron showers in copper at different energies, energy deposit as function of depth, obtained from Monte Carlo simulations. The integrals of the curves are normalized to the same value in order to compare the different profiles. Figure from Wigmans [6].
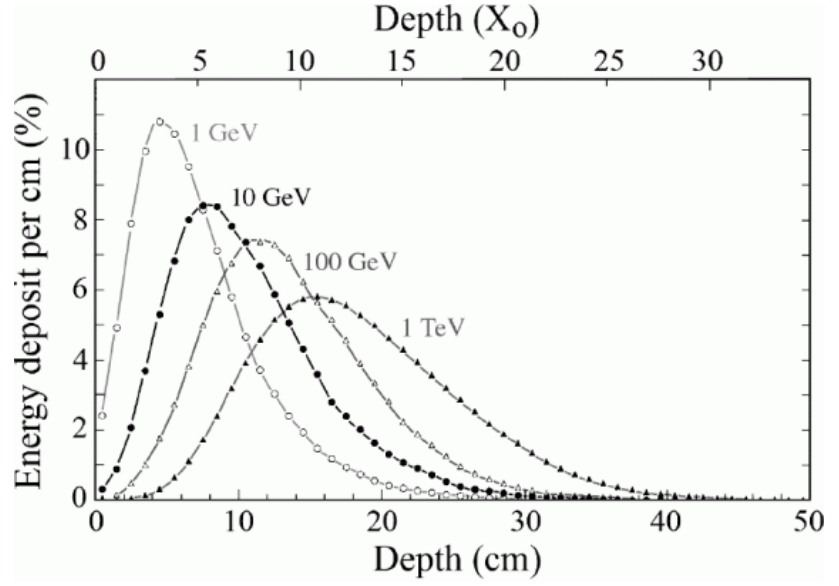
The mean longitudinal profile of the energy deposition can be described by a gamma distribution [3] with

$$\frac{dE}{dt} = E_0\, b\, \frac{(bt)^{a-1} \exp{(-bt)}}{\Gamma(a)} \,, \qquad (2.12)$$

where $t = x/X_0$ with distance x, X_0 is the radiation length in cm, a the shape parameter, $b \approx 0.5$ the scaling parameter, and Γ the Gamma function.

Gamma function:
$\Gamma(a) = (a-1)!$ for $a \in N$

Therefore the shower maximum, the depth at which the largest number of secondary particles is produced, is located at $t_{\text{max}} = (a-1)/b$ [3], approximately at

$$t_{\text{max}} \simeq \ln\frac{E_0}{E_c} - 0.5 \qquad \text{for electrons}\,,$$

$$\qquad (2.13)$$

$$t_{\text{max}} \simeq \ln\frac{E_0}{E_c} + 0.5 \qquad \text{for photons}\,,$$

where t_{max} is measured in radiation lengths and E_0 is the energy of the incident particle.

Hence photon-induced showers penetrate on average one $1\,X_0$ deeper than than those induced by electrons.

The transverse size of a shower scales with the Molière radius R_M [3] and is given by

$$R_M = \frac{E_S}{E_c}\, X_0 \,, \qquad (2.14)$$

which scales with energy $E_S = m_e c^2 \sqrt{4\pi/\alpha} = 21.2\,\text{MeV}$, where α is the fine structure constant. E_c is the critical energy defined by Rossi, and X_0 the radiation length.

The physical processes of hadronic showers are different from those of electromagnetic showers due to nuclear interactions. Since they are not relevant for this work, they are not described any further. A detailed description can be found in Wigmans [6].

2.2 Calorimetry

Calorimeters are detectors, designed to measure the energy of incident particles. They can be also used for particle identification. They usually consist of blocks of material in which particles lose energy until they are completely absorbed and a medium in which their energy is converted into a measurable quantity. They are sensitive to both charged and neutral particles and can detect non-interacting particles such as neutrinos indirectly via missing energy.

Calorimeters can be divided into electromagnetic calorimeters (ECALs), which are used to measure mainly electrons and photons through their electromagnetic interactions such as bremsstrahlung and pair production, and hadronic calorimeters (HCALs), which mainly measure hadrons, such as protons, neutrons, pions and kaons, through their strong and electromagnetic interactions. ECALs are characterized by the radiation length X_0 and HCALs by nuclear interaction length λ.

Energy Resolution

The energy resolution of a calorimeter determines the precision with which the energy of a given particle can be measured. It is an important characteristic for the performance of a calorimeter.

In general, the deposited energy E is proportional to the number of interactions N occurring in the detector volume:

$$E \propto N \,. \tag{2.15}$$

Therefore the width of the deposited energy σ_E, as in a Poisson process, is given by

$$\sigma_E \propto \sqrt{N} \,. \tag{2.16}$$

Resulting in a energy resolution of

$$\frac{\sigma_E}{E} \propto \frac{\sqrt{N}}{N} = \frac{1}{\sqrt{N}} \propto \frac{1}{\sqrt{E}} \,, \tag{2.17}$$

where E is the deposited energy and σ_E the width of the deposited energy.

Therefore calorimeters are very well suited to high-energy physics experiments.

In reality, the energy resolution of a calorimeter is also influenced by other factors, such as contributions from electronic noise in the readout of the detector and instrumental deficiencies such as the calibration of the detector. The energy resolution can be then expressed as

$$\frac{\sigma}{E} = \frac{a}{\sqrt{E}} \oplus \frac{b}{E} \oplus c \,, \tag{2.18}$$

Quadratic sum:
$$a \oplus b \oplus c = \sqrt{a^2 + b^2 + c^2}$$

where $\oplus$ is the quadratic sum, E the energy, and a, b and c are parameters.

The first term in Equation 2.18 is the stochastic term, and includes the shower intrinsic fluctuations mentioned above, the second term is the noise term, and the third term is the constant term and describes the calibration precision.

Calorimeters can be further classified according to their construction technique, divided into sampling calorimeters and homogeneous calorimeters.

Sampling Calorimeters

Sampling calorimeters consist of alternating layers of an absorber and an active material. A schematic of such a calorimeter is shown on the left in Figure 2.8. The absorber, especially in electromagnetic calorimeters, is a dense material with a high atomic number Z to slow down the incident particles to such an extent that they lose all their energy in the detector. The active materials provides the detectable signal that is proportional to the energy deposit in this material. Typical absorbers are iron, lead, tungsten or uranium, whereas active materials are made of organic scintillators, silicon, liquid or gaseous detectors. Usually, sampling calorimeters provide inferior energy resolution compared to homogeneous calorimeters. However, their advantages lie in offering very good spatial resolution due to longitudinal and transverse segmentation. They are also more cost-effective and more flexible in the design with a larger variety of geometries. Examples of sampling electromagnetic calorimeters in high energy physics are found in the KLOE experiment [7] at the Laboratori Nazionali di Frascati (INFN) and in the ATLAS experiment [8] of the LHC at CERN.

Homogeneous Calorimeters

Homogeneous calorimeters consist entirely of a high-density material that fulfills both tasks, energy absorption and signal generation, serving both as an absorber and active material. A schematic of such a calorimeter is shown on the right in Figure 2.8.
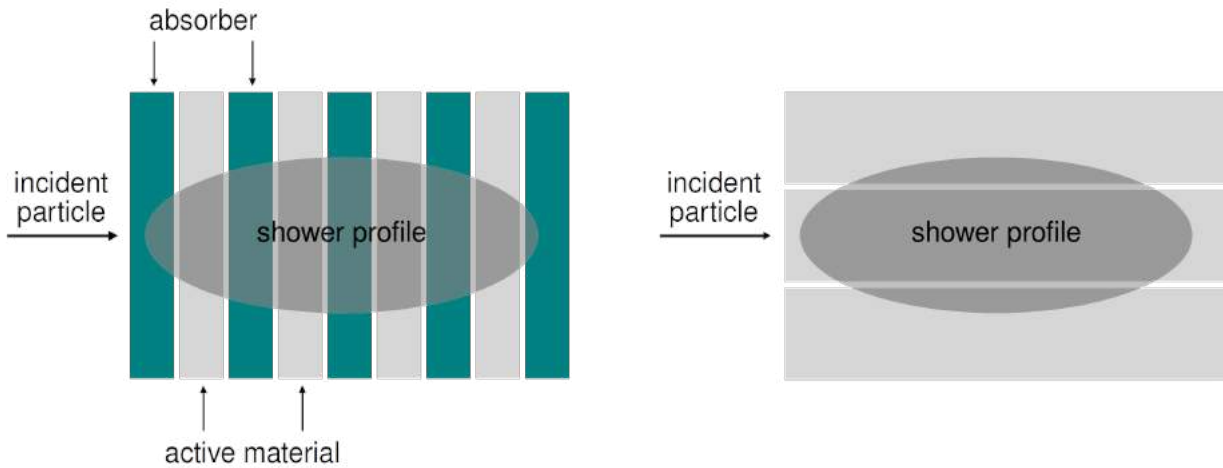
Figure 2.8: On the left, schematic of a sandwich calorimeter as example of a sampling calorimeter, consisting of alternating layers of an absorber and an active material. On the right, schematic of a homogenous calorimeter, consisting of a material that acts as an absorber and active material.

Typical materials are heavy scintillating materials such as BGO, CsI, and $PbWO_4$. Such calorimeters have an excellent energy resolution, because unlike sampling calorimeters the whole energy of an incident particle is deposited in the active medium. On the other hand, homogeneous calorimeters can not be segmented as easily as sampling calorimeters, which is an intrinsic drawback when it becomes to position measurements and particle identification. An other disadvantage are the relatively high costs. The CMS electromagnetic calorimeter [9] of the LHC at CERN, built of crystal blocks made of lead tungstate (PWO), is a predominant example of a homogeneous calorimeter.

Depending on the global detector concept, a sampling calorimeter or a homogeneous calorimeter should be selected. Concepts of using nano-materials in calorimetry are introduced in Section 4.5 and discussed in detail in Chapter 7.

.

Scintillation and Scintillators | 3

Scintillation is a physical process where a material, called a scintillator, emits ultraviolet (UV) or visible (VIS) light due to interaction with ionizing radiation, such as gamma rays, X-rays, or charged particles (e.g. electrons). For applications in detectors in high energy physics, there are many desired properties of scintillators, such as high density, fast timing, low cost, radiation hardness, production capability, and durability of operational parameters.

In this chapter, a brief introduction to the different types of scintillators is given first, followed by the discussion of general characteristics and properties of scintillators.

3.1 Scintillation Materials

Scintillators are materials that are able to emit photons when excited with ionizing radiation. The most commonly used scintillation materials are classified as inorganic and organic scintillators.

Inorganic Scintillators

Inorganic scintillators are scintillating materials composed of inorganic compounds and minerals. These materials often contain elements such as sodium, iodine and cesium. Inorganic crystals, compared to organic crystals, have higher stopping power owing to higher densities, typically between 4 and $8\,\mathrm{g\,cm^{-3}}$, and a larger content of high-Z elements [3]. This makes them well suited to electromagnetic calorimeters, in particular homogeneous calorimeters. Compared to organic scintillators, inorganic scintillators benefit from a higher light yield, are more resistant to radiation damage, albeit at the expense of slower decay times. Common examples are sodium iodide (NaI), cesium iodide (CsI), bismuth germanate (BGO), lutetium oxyorthosilicate (LSO), lutetium–yttrium oxyorthosilicate (LYSO), barium fluoride (BaF_2) and lead tungstate (PWO). Some inorganic scintillators are intrinsic scintillators, and others require the addition of a dopant of fluorescent ions such as thallium (Tl) or cerium (Ce), which generate the scintillation light. However, the scintillation mechanism is the same in both cases. Energy is deposited in the scintillator by ionization and is transferred to the luminescent centers which then emit scintillation photons.

Organic Scintillators

Organic scintillators are scintillating materials composed of organic (carbon-based) molecules. They are divided into single crystals, plastics, liquids, and even glasses [3]. Plastic scintillators are known for their high

speed and commonly used because of their low cost and ease of manufacture. They can be manufactured not only in large sizes but also in various shapes. They consist of a polymer matrix, such as polystyrene (PS) or polyvinyltoluene (PVT), in which organic dyes are embedded. They can also be in the form of scintillating, wavelength-shifting or just clear fibers. These fibers can be useful as light guides for photodetectors. Plastic scintillators have lower densities, typically between 1.03 and 1.20 g cm^{-3}, and lower Z elements. Thereby the light yield of organic scintillators is lower than for inorganic scintillators. For most scintillators typical light yields are in the range of 10 000 photons per MeV, with usually faster decay times than inorganic scintillators, in the range of a few nanoseconds [4] [10]. On the other hand they are more prone to radiation damage. They are often used for particle detectors and sampling calorimeters, but are less suitable for applications requiring high stopping power, such as in homogeneous calorimeters or gamma spectroscopy.

Typical representatives of plastic scintillators are, for example, products from ELJEN Technology, USA, as shown in Figure 3.1. The EJ232 scintillator [11] from this company is known to be a fast timing plastic scintillator, and is used as the reference in this work to evaluate the performance of the nanomaterials.
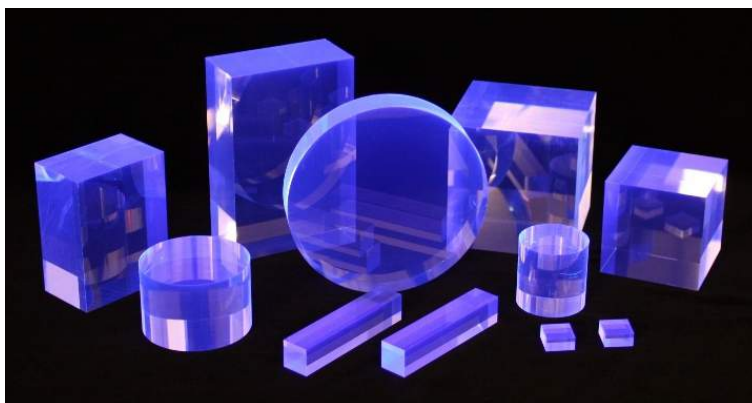

Figure 3.1: Plastic scintillators from ELJEN Technology as example for organic scintillators. Figure from ELJEN Technology [11].

Table 3.1 shows the properties of a few commonly used conventional inorganic and organic scintillators.

Table 3.1: Properties of some commonly used conventional, inorganic and organic, scintillators.

Name	Material	Density [g cm^{-3}]	Emission Peak [nm]	Light Yield [ph MeV^{-1}]	Decay Time [ns]
LSO [12]	Lu$_2$SiO$_5$:Ce	7.4	420	27 000	40
BGO [12]	Bi$_4$Ge$_3$O$_{12}$	7.13	505	8 200	300
PWO [12]	PbWO$_4$	8.28	420	100	6
BaF$_2$ [12]	BaF$_2$	4.88	220/310	1 430/9 950	0.6/620
NaI:Tl [12]	NaI:Tl	3.67	415	43 000	230
CsI:Tl [12]	CsI:Tl	4.51	560	51 800	1000
EJ232 [11]	plastic	1.023	370	8 400	1.6

3.2 Scintillation Mechanism

Scintillators are classified as inorganic or organic scintillators depending on their chemical composition. Inorganic scintillators exhibit luminescence either intrinsically or through the introduction of luminescent ions via doping. In organic scintillators the transition of exhited valence electrons, occupying molecular orbits, lead to luminescence.

Inorganic Scintillators

The luminescent properties of scintillators are based on their band structure containing only specific energy levels. Due to their crystalline structure, scintillators comprise a core band, a valence band and a conduction band, each with corresponding sub-bands. The region between the conduction band and the valence band is known as the bandgap with energy E_g, the so-called forbidden gap. A schematic of the scintillation process in ionic scintillators is shown in Figure 3.2.
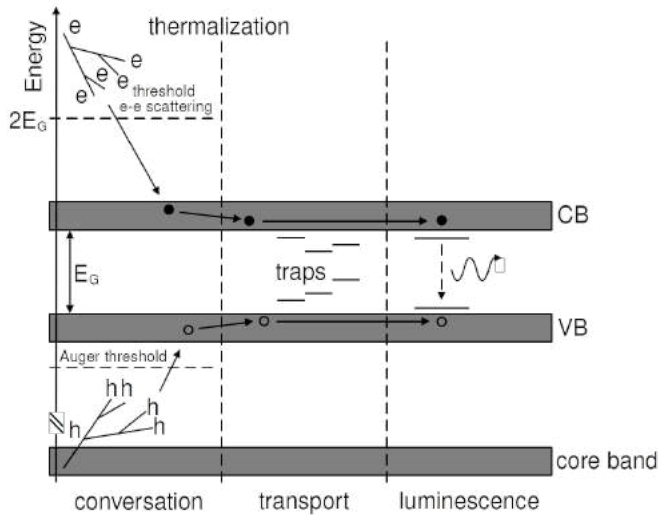

Figure 3.2: Illustration of the scintillation mechanism of ionic scintillators with electrons (e), holes (h), conduction band (CB), valence band (VB), and bandgap E_g, the energy difference between the conduction band and the valence band. Figure adapted from Nikl [13].

In the first stage, when energetic particles or photons interact with a scintillating crystal, atoms in the crystal are ionized, creating holes in the core band and "hot" highly energetic electrons in the conduction band, releasing them from their bound states. Immediately after the interaction, within the first femtoseconds, these electrons lose energy through inelastic electron-electron scattering in a process called "cool down", generating further electron-hole pairs. This process continues until the electron energy drops below the inelastic electron-electron scattering threshold, which is usually twice the bandgap energy. The holes in the core band move towards the valence band through Auger processes until their energy passes the Auger threshold. However, electrons and holes generated at this stage are still too energetic to occupy the luminescence centers of the scintillating crystal.

In the subsequent phase, both the electrons and the holes undergo thermalization over a time range of a few femtoseconds to picoseconds by phonon scattering, which are essentially lattice vibrations, leading to low kinetic energy electrons in the bottom of the conduction band and holes in the top of the valence band.

The Auger effect describes the filling of a vacancy in the inner shell of an atom, followed by the emission of an electron from this atom. An incident electron (or photon) creates a core hole in the 1s level. An electron from the 2s level fills the 1s hole and the transition energy is passed on a 2p electron which is emitted as Auger electron. The final atomic state thus has two holes, one in the 2s orbital and the other in the 2p orbital.

In the next stage within the next 100 ps, the so-called localization process, electrons and holes are trapped by defects and impurities (traps) in the crystal. Excitons, self-trapped excitons, and self-trapped holes, can be formed still with the emission of phonons.

In the following stage, recombination of electrons with self-trapped holes (V_k) leads to the excitation of nearby luminescence centers. Similarly self-trapped excitons can produce luminescence through recombination with energy transfer to the luminescent centers. With the recombination of the localized excitations the scintillation light is emitted, approximately after 10 ns [12].

The above process describes the scintillation mechanism in ionic crystals. In such crystals, the final process of light emission is in most cases very inefficient, also in combination with too large a gap width to produce photons in the visible range. In order to emit light in the visible range, impurities based on rare earths such as cerium (Ce), also known as activators, are added to serve as luminescence centers. Doping with rare earths is also known to improve the intrinsic light yield, whereas co-doping with calcium (Ca) or aluminum reduces the decay time of the crystal without impairing the light yield.

Another method to improve the timing performance of scintillating crystals is the use of cross-luminescence as a scintillation process. Cross-luminescence, also known as Auger-free luminescence, only occurs in crystals with a bandgap difference between the top of the core band and the valence band of less than the energy difference E_g, the bandgap difference between the valence band and the conduction band. Cross-luminescence is then the result of holes in the core band recombining with electrons in the densely populated valence band. Since the recombination probability is high, cross-luminescence is intrinsically fast, with typical decay times of the order of nanoseconds or less [14]. A typical example of a cross-luminescence emitter is BaF_2. A detailed description of the corresponding scintillation processes can be found, for example, in Lecoq et al. [12].

The total number of electron-hole pairs N_{eh} participating in the recombination process does not only depend on the deposited energy, but also on the characteristics of the scintillation material [12]. It is given by

$$N_{eh} = \frac{E_0}{E_{eh}} = \frac{E_0}{\beta E_g}, \tag{3.1}$$

where E_0 is the deposited energy in the material and E_{eh} the average energy to produce an electron-hole pair in the material.

The average energy E_{eh} is related to the bandgap energy E_g of the material by the β factor [12], expressed by

$$E_{eh} = \beta \cdot E_g. \tag{3.2}$$

The intrinsic light yield LY [12] describes the amount of photons N_{ph} produced when a certain amount of energy E_0 is deposited in the material, and is given by

$$LY = N_{ph} = N_{eh} \cdot S \cdot Q = \frac{E_0}{E_{\text{eh}}} \cdot S \cdot Q \,, \qquad (3.3)$$

where S is the energy transport efficiency to the luminescence centers, and Q the luminescence quantum yield.

Organic Scintillators

The scintillation mechanism of organic scintillators differs from that of inorganic scintillators. The electronic states of organic molecules are illustrated in Figure 3.3. A series of singlet (spin 0) states are labeled with S_0, S_1, S_2, a series of triplet (spin 1) states with T_1, T_2, T_3. For organic scintillators the energy spacing between S_0 and S_1 is 3 to 4 eV, whereas spacing between higher lying states is usually smaller. Each S level is subdivided into a series of sublevels with a finer structure, each of the order of 0.15 eV, corresponding to the vibrational states of the molecules and labeled with a second subscript [15]. At room temperature all molecules are in the S_{00} state, since the average thermal energy is approximately 0.025 eV and the spacing between the vibrational states is large compared to this.
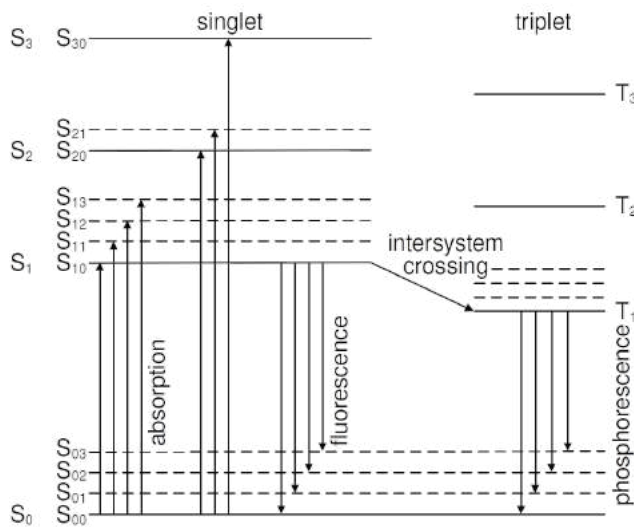

Figure 3.3: Electronic states of organic molecules. The singlet states (spin 0) are represented by S_1, S_2, and S_3, the triplet states (spin 1) by T_1, T_2, T_3. Each S level is subdivided into a series of sublevels with a finer structure, corresponding to the vibrational states of the molecules. The absorption of energy by the molecules is represented by up arrows. Fluorescence, as principal scintillation light, is emitted in transitions between the S_{10} state and the vibrational states of the ground electronic state S_0. Through an intersystem crossing, some excited singlet states can convert into triplet states. Phosphorescence is emitted in transitions between the T_1 state and the vibrational states of the ground electronic state S_0. Figure adapted from Knoll [15].

When charged particles or photons pass through the scintillator, their kinetic energy is absorbed by the molecules and electrons are excited to various electronic states, as shown in Figure 3.3. As the figure shows two types of radiative transitions occur, one fast transition between the singlet states S_1 and the vibrational states of the ground state S_0 in terms of fluorescence, and, due to an intersystem crossing from a singlet to a triplet state, a delayed slower transition from the lowest triplet T_1 state to the vibrational states of S_0 in terms of phosphorescence [15].

In organic scintillators, the fluorescence is of primary interest and its intensity I [15] over time is given by

$$I = I_0 \cdot e^{-\frac{t}{\tau}} , \tag{3.4}$$

where t is the time after excitation, I_0 the maximum intensity, and τ the decay time. In most organic scintillators τ is in the order of nanoseconds.

Figure 3.4 shows the absorption and emission spectra of typical organic scintillators. A common requirement for the choise of scintillators is that both spectra overlap as little as possible in order to avoid reabsorption. This is commonly expressed as the Stokes shift.
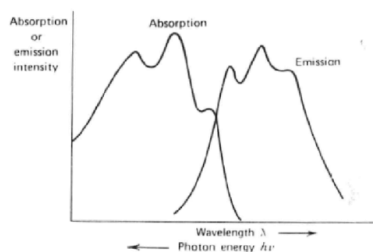
Since the molecules in organic scintillators emit primarily in the ultraviolet (UV), these scintillators have one or several fluorescent dyes as dopants. There are two mechanisms that transfer the energy from the excited organic molecules to the fluorescent dyes which are either radiative via photon transfer or non-radiative via the Förster mechanism. Common fluorescent dyes include 2,5-diphenyloxazole, p-terphenyl, 9,10-diphenylanthracene (9,10-DPA), 1,4-bis(2-methylstyryl)benzene (bis-MSB) and 1,4-bis(5-phenyl-2-oxazolyl)benzene (POPOP). Typical concentrations of "primary" dyes are 1 to 3 wt %, which is high enough to ensure that energy transfer occurs mainly via the Förster mechanism. A "secondary" (and sometimes a third) dye is added with typical concentrations of 0.01 to 0.2 wt % to reduce the self-absorption of the emitted light by the organic molecules or the primary dyes and to shift the emitted light to longer wavelengths into the regime of the optimum quantum efficiency window of photodetectors. The energy transfer from the primary to the secondary dyes is generally radiative [3].

Figure 3.4: Absorption and emission spectra of typical organic scintillators. Since the emission and excitation spectra overlap only slightly, the self-absorption of the fluorescence is low. Figure adapted from Knoll [15].

Fluorescent dyes, also known as fluorophores, are molecules absorbing light at given wavelengths and re-emitting it at longer wavelengths.

Förster (fluorescence) resonance energy transfer (FRET) describes a resonant dipole-dipole energy transfer through a non-radiative process. This process is highly distance-dependent and decreases at the sixth power of the distance between the molecules [4].

3.3 Scintillation Characteristics

Photoluminescence

Photoluminescence (PL) of a scintillator is the emission of light that occurs when the scintillator is excited by external light sources (UV and visible light). It differs from scintillation in that it is not induced by ionizing radiation. The emission spectrum gives the intensity of the emitted light as a function of wavelength. This spectrum offers important information on the energy levels involved in the luminescence.

The Stokes shift $\Delta\lambda$ is the difference between the maximum absorption and emission wavelengths [15], as illustrated in Figure 3.5:
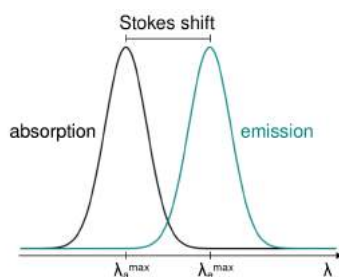
$$\Delta\lambda = \lambda_a^{max} - \lambda_e^{max} . \tag{3.5}$$

Figure 3.5: The Stokes shift is the difference between the maximum absorption and emission wavelengths.

Transmission and Absorption

The transmission of a scintillator is defined as the fraction of light intensity that passes through a scintillator with a given monochromatic light beam of intensity I_0 and wavelength λ:

$$T(\lambda) = \frac{I(\lambda)}{I_0(\lambda)} \, , \qquad (3.6)$$

with I the light intensity observed after the transit of light through the sample.

The absorption of light by the scintillator is defined as the logarithm of the ratio of incident to transmitted light intensity:

$$A(\lambda) = \log_{10} \frac{I_0(\lambda)}{I(\lambda)} = -\log_{10} T(\lambda) \, , \qquad (3.7)$$

where I_0 is the incident and I the transmitted light intensity.

Emission and excitation spectra provide important information on the energy levels of the scintillating material, while transmission and absorption quantitatively assess the quality of the scintillator.

Light Yield and Light Output

Light yield refers to the amount of light produced by a scintillator in response to a certain amount of incident radiation such as gamma rays, X-rays, or charged particles. It is defined as the average number of photons produced per unit energy deposited in the scintillator.

The measurement of light yield is difficult and often confused with the so called light output used to indicate the number of photoelectrons collected at the photodetector. Contrary to light yield the light output depends on several factors such as the refractive index of the scintillator, its geometry, its surface and its light transport, bulk conditions and the photodetector coupling, and is expressed as number of photoelectrons per unit energy deposited in the scintillator.

The relation between light yield LY and light output LO [3] is given by

$$LO = LY \cdot LC \cdot QE \, , \qquad (3.8)$$

where LC is the light collection efficiency and QE the quantum efficiency.

The light collection efficiency depends on the size and shape of the scintillator and includes effects such as transmission and absorption of scintillation light within the scintillator, reflections and scattering from the scintillator surfaces and rebound into the scintillator through wrapping or reflector materials.

The quantum efficiency depends on the type of photodetector used to detect the scintillation light. It is usually dependent on the wavelength and should be adapted to the respective scintillator response in order to

achieve the highest light output at the wavelength corresponding to the peak of the scintillation emission.

Self-absorption due to small Stokes shifts can lead to a loss of light.

Scintillation Kinetics

The scintillation kinetics are defined as the time evolution of the scintillation intensity $I(t)$. It is affected by the dynamics of the carriers and of the luminescence centers. It is often described by sets of differential equations solved numerically. A common first-order approximation is to describe $I(t)$ as a sum of bi-exponential functions [16] by

$$I(t \mid \theta) = \Theta(t - \theta) \sum_{i=1}^{N} \frac{\exp\left(-\frac{t-\theta}{\tau_{d,i}}\right) - \exp\left(-\frac{t-\theta}{\tau_{r,i}}\right)}{\tau_{d,i} - \tau_{r,i}} \cdot R_i , \qquad (3.9)$$

where t is the time, θ the time of onset of scintillation, and Θ the Heavyside step function. The parameters $\tau_{r,i}$ and $\tau_{d,i}$ denote the rise and the decay time of the photon distribution, respectively, and R_i being the i-th component of the abundance.

Heavyside step function:

$$\Theta(t - \theta) = \begin{cases} 1, & t - \theta \geq 0 \\ 0, & t - \theta < 0 \end{cases}$$

Often scintillators feature multiple fast and slow decay times. The effective decay time $\tau_{d,eff}$ [17], as the weighted harmonic average of the decay times, is a figure of merit that allows comparison of different materials and is defined by

$$\frac{1}{\tau_{d,eff}} = \sum_{i=1}^{N} \frac{R_i}{\tau_{d,i}} \qquad \text{with} \qquad \sum_{i=1}^{N} R_i = 1 . \qquad (3.10)$$

A schematic of two scintillation distributions is shown in Figure 3.6, as examples of slow and fast decay processes.
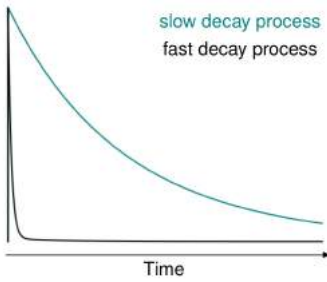

Figure 3.6: Two scintillation distributions as examples of slow and fast decay processes. Slower decay processes have longer tails.

Time Resolution

Fast timing has become an important feature in several domains in the last few years and is a crucial requirement in the choice of scintillators used in timing experiments. For example, particle physics experiments running at future high luminosity accelerators will rely on fast timing detectors to cope with high event pileup and to enhance particle identification capabilities.

The possibility of time-tagging the arrival of a particle with a precision of about 10 ps will be crucial to deal with pile-up at high-luminosity colliders. Besides applications in HEP, fast timing materials can also be used in time-of-flight positron emission tomography (TOF-PET) to benefit from similar time resolutions. The time-of-flight information in PET significantly reduces the background and, ideally, leads to a three-dimensional determination of the gamma vertex of the order of millimeters.

The timing measurement is made by assigning time stamps to a particular event. For example in HEP typical time stamps are the beam crossing to provide a fast trigger for data filtering. On the other hand, in PET

where no independent timing information is available two correlated time stamps are provided by two co-linear back-to-back gammas from the positron-electron annihilation. In order to get the most precise timing information the signal pulses must exceed a preset threshold as early as possible. Commonly used techniques include leading edge discrimination where the timestamp is determined when the signal pulse passes a given amplitude threshold, or constant fraction discrimination (CFD) where a threshold is set to a specific fraction of the pulse amplitude.

The time resolution is then derived from a Gaussian fit either in terms of its standard deviation σ, common in HEP applications, or in terms of the full width at half maximum (FWHM), common in optical physics. Both are linked by

$$FWHM = 2\sqrt{2\ln 2}\,\sigma \approx 2.36\,\sigma\,. \tag{3.11}$$

Vinogradov [18] has demonstrated that the time resolution achieved by a scintillator can be approximated by

$$\sigma_{\mathrm{t}} \propto \sqrt{\frac{\tau_{\mathrm{r}}\tau_{\mathrm{d}}}{LO}}\,, \tag{3.12}$$

where τ_{r} and τ_{d} are the rise and decay times, and LO is the light output of the scintillator.

If a scintillator features multiple decay times that are of the same order of magnitude, the decay time τ_{d} can be replaced in Equation 3.12 by the effective decay time $\tau_{\mathrm{d,eff}}$. However, if there are large differences between the decay times, the shorter ones dominate, as the photon density at the beginning of the scintillation process is determinant for the timing. This shows that scintillators for fast timing require both a high light yield and fast rise and decay times.

Coincidence time resolution (CTR) and detector time resolution (DTR), the latter also known as single time resolution as opposed to CTR where a pair of detectors is used, are the standard terms for specifying the timing performance of scintillating materials.

If two similar detectors are used, the relationship between CTR and DTR is expressed by

$$DTR = \frac{CTR}{\sqrt{2}}\,. \tag{3.13}$$

Surface State, Wrapping and Optical Coupling

The surface state of a scintillator plays an important role in its performance.

Fresnel reflection occurs when a photon impinges on an interface between different optical media, for instance at the interface of a scintillator. According to Snell, the law of refraction [19], as illustrated in Figure 3.7, describes the relationship between the angles of incidence and refraction, passing a boundary between two different media with different refractive indices:

$$n_1 \cdot \sin \theta_1 = n_2 \cdot \sin \theta_2 \, , \tag{3.14}$$

where n_i is the refractive index of the i-th medium, θ_i the incidence angle of the photon in the i-th medium.

The critical angle θ_c is defined as the value of the angle θ_1 for which $\theta_2 = 90°$:

$$\theta_c = \arcsin \frac{n_1}{n_2} \cdot \sin \theta_2 = \arcsin \frac{n_1}{n_2} \qquad \text{with} \qquad \sin(90°) = 1 \, . \tag{3.15}$$

Refraction occurs at angles smaller than θ_c, reflection at angles larger than θ_c. The phenomenon is called total internal reflection.
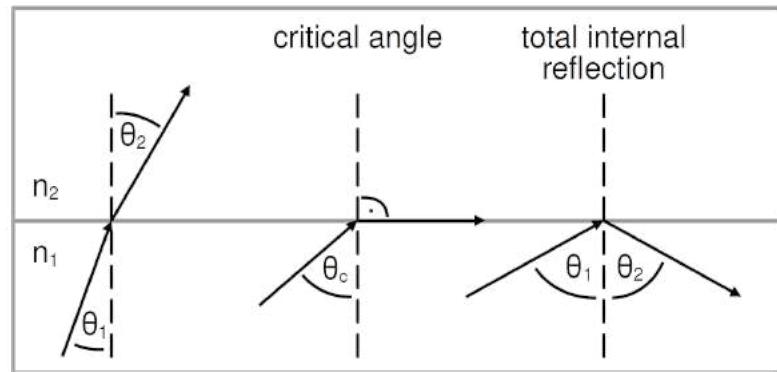
Figure 3.7: Refraction of light at the interface between two different media with different refractive indices, according to Snell. Total internal reflection occurs at angles $\theta_1 > \theta_c$.

For efficient light collection, it is important that the surface of a scintillator facing the photodetector must be flat and that the entire scintillator be as transparent as possible. Optical polishing of the lateral surfaces allows, via total internal reflection within the critical angle, the optimum transport of scintillation light towards the readout surface of the scintillator and simultaneously to avoid photon diffusion at the surfaces. It is also common to wrap scintillators with a reflector such as Teflon, also known to improve light yield. In order to avoid light losses due to different refractive indices at the scintillator/photodetector interface, optical coupling agents such as Rhodorsil grease or Meltmount glue are used.

Radiation Hardness

The use of scintillators in high energy physics requires that the scintillators are resistant to high radiation. The interaction of ionizing radiation with the scintillator changes the composition of the material and creates traps and defects, which can be of different nature. This may lead to a deterioration of the scintillator properties. The ability of a scintillator to retain its properties unchanged after irradiation and to be resistant to radiation damage is referred to as radiation hardness.

This is of particular importance for scintillators used in experiments running at future high luminosity colliders which are exposed to very high rates of ionizing particles.

Nanomaterials | 4

In this chapter novel scintillating nanomaterials are described. These nanoscintillators are the focus of this thesis. They are supposed to have fast timing and high light yield with potentially low cost production, and can thus be suitable candidates for future detectors in high energy physics and for medical applications.

A material is called a nanomaterial when is has structures or features at the nanometer scale. What makes these nanomaterials special is that their properties depend on their size. This feature is also explained in this chapter.

4.1 Nanocrystals

Semiconductor nanocrystals (NCs) are nanometer-sized crystalline particles, which are characterized by the same crystal lattice structure as the corresponding bulk semiconductors. Their size is of the order of the Bohr radius for a bulk semiconductor, typically in a range of 1 to 100 nm for most materials. When their size is smaller or comparable to the Bohr radius, electron-hole pairs and excitons can no longer be considered as free particles but, due to the effect of quantum confinement, can only occupy specific and quantized energy levels.

Semiconductors such as silicon and germanium are materials with electrical conductivity lying between the conductivity of pure conductors (e.g. copper) and pure insulators (e.g. glass).

This is defined by the density of states ρ being defined as the number of states per energy E and per unit volume. The density of states describes the energy and momentum distribution of electrons and holes within a sub-band. It can be expressed by

The Bohr radius a_0 is a physical constant which represents the most probable distance between the electron and the nucleus in a hydrogen atom in its ground state. It is defined as $a_0 = \frac{4\pi\epsilon_0\hbar^2}{m_e e^2} = \frac{r_e}{\alpha^2}$.

$$\rho(E) = \frac{dN}{dE} \ , \tag{4.1}$$

where N is the number of states, and E the energy.

An exciton is a bound state of an electron and a hole that are attracted to each other by the Coulomb force.

The quantization of the energy or the reduction of the dimensionality of the system is directly reflected by the dependence of the density of states on the energy [20], as shown in Figure 4.1.

The density of states ρ for a 3D system system, called bulk semiconductor, is given by

Three-dimensional (3D)

$$\rho(E) = \frac{dN}{dE} \propto \frac{d}{dE} E^{3/2} = E^{1/2} \ . \tag{4.2}$$

For nanostructures ρ for a 2D system, called quantum well, is a step function

Two-dimensional (2D)

$$\rho(E) = \frac{dN}{dE} \propto \frac{d}{dE} \sum_{\epsilon_i < E}(E - \epsilon_i) = \sum_{\epsilon_i < E} E^0 = \sum_{\epsilon_i < E} 1 \ , \tag{4.3}$$
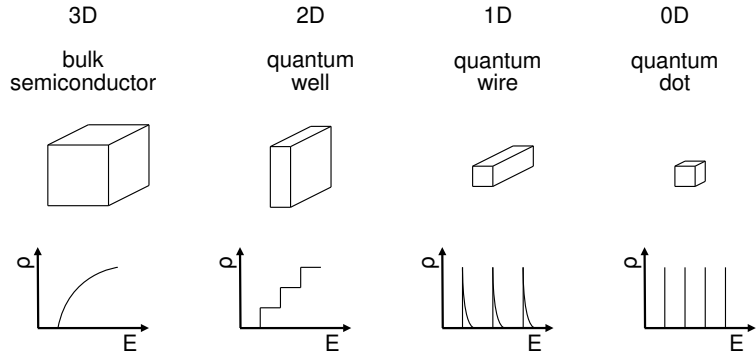
Figure 4.1: Density of states as function of energy in systems with different numbers of spatial dimension: 3D bulk material or bulk semiconductor (continuous spectrum), and semiconductor nanostructures such as 2D quantum well, 1D quantum wire and 0D quantum dot (discrete spectrum). Figure adapted from Rabouw et al. [21].

One-dimensional (1D)

for a 2D system system, called quantum wire, $\rho(E)$ is given by

$$\rho(E) = \frac{dN}{dE} \propto \frac{d}{dE} \sum_{\epsilon_i < E} (E - \epsilon_i)^{1/2} = \sum_{\epsilon_i < E} (E - \epsilon_i)^{-1/2} , \qquad (4.4)$$

Zero-dimensional (0D)

and for a 0D system system, called quantum dot, $\rho(E)$ has the shape of δ peaks

$$\rho(E) = \frac{dN}{dE} \propto \frac{d}{dE} \sum_{\epsilon_i < E} \Theta(E - \epsilon_i) = \sum_{\epsilon_i < E} \delta(E - \epsilon_i) , \qquad (4.5)$$

Heavyside step function:
$$\Theta(E - \epsilon_i) = \begin{cases} 1, & E - \epsilon_i \geq 0 \\ 0, & E - \epsilon_i < 0 \end{cases}$$
Dirac function:
$$\delta(E - \epsilon_i) = \begin{cases} \infty, & E - \epsilon_i = 0 \\ 0, & E - \epsilon_i \neq 0 \end{cases}$$

where ϵ_i are the discrete energy levels, E is the energy, Θ the Heavyside step function, and δ the Dirac function.

4.2 Quantum Dots

As already outlined above, quantum dots (QDs) are nanometer-sized semiconductors with sizes of the order of 1 to 10 nm, where electrons and holes are confined in all three dimensions, occupying specific and quantized energy levels. The resulting effects of the confinement are shown in Figure 4.2. First, it leads to a collapse of the continuous energy bands in the bulk material into discrete, atomic-like energy states, resulting in discrete absorption spectra of the QDs, represented by vertical bars in Figure 4.2. It is in contrast to the continuous absorption spectra of bulk semiconductors. Furthermore, the confinement also causes a material and size-dependent QD energy bandgap. This bandgap E_g is the energy difference between the lowest electron and hole QD state, obtained by using the 'quantum box' model [22], as illustrated in Figure 4.3, and expressed by

$$E_g(QD) \approx E_{g,0} + \frac{\hbar^2 \pi^2}{2m_{eh}R^2} \quad \text{with} \quad m_{eh} = \frac{m_e \cdot m_h}{m_e + m_h} , \qquad (4.6)$$

where m_e and m_h are the masses of electrons and holes, respectively, $E_{g,0}$ is the bandgap of the bulk semiconductor, and R is the radius of the QD.
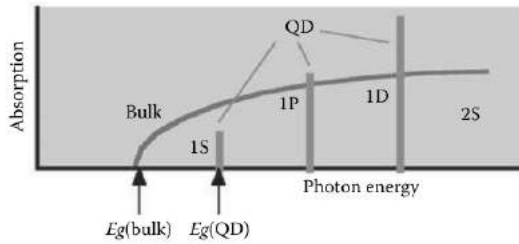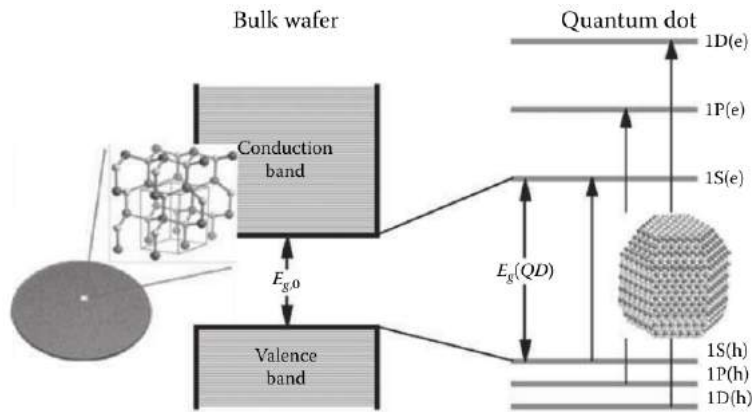
Figure 4.3: Band structure of bulk semiconductors with continuous conduction and valence bands separated by the energy band gap $E_{g,0}$ (left), whereas QDs are characterized by discrete atomic-like states with a material- and size-dependent band gap E_g, the energy difference between the lowest electron [1S(e)] and hole [1S(h)] QD state (right). Figure from Klimov [22].

With decreasing QD size, the energy bandgap increases, leading to a blue shift in the emission wavelength, as illustrated in Figure 4.4, as the frequency of the emitted light is directly proportional to the energy (Equation 2.6). As a result larger QDs of 5 to 6 nm diameter with smaller band gaps emit longer wavelengths, with colors such as orange or red, while the smaller QDs of 2 to 3 nm diameter having larger bandgap produce shorter wavelengths in the green and blue, as illustrated in Figure 4.4. However, the specific color of QDs also depends on their composition.
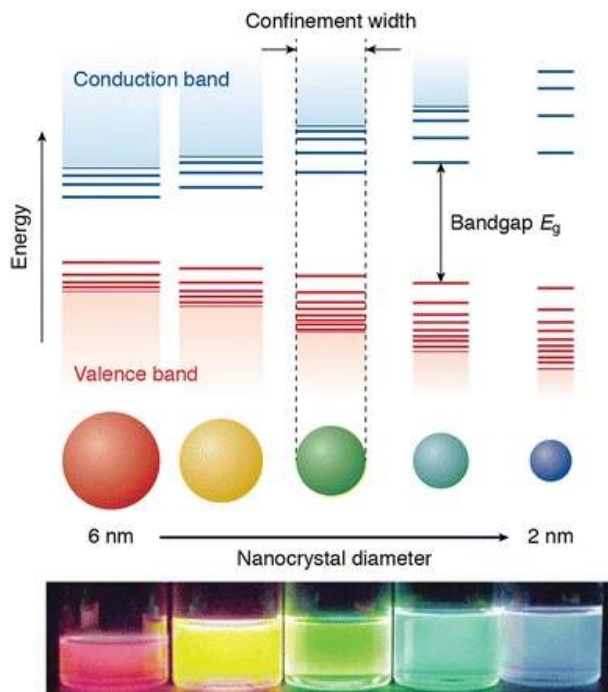

Figure 4.4: Due to quantum confinement, the bandgab of QDs increases with decreasing QD size, leading to a blue shift in the emission wavelength. The photograph below shows the fluorescence of five dispersions of cadmium selenide (CdSe) QDs of different sizes under UV excitation. Figure adapted from Rabouw et al. [21].
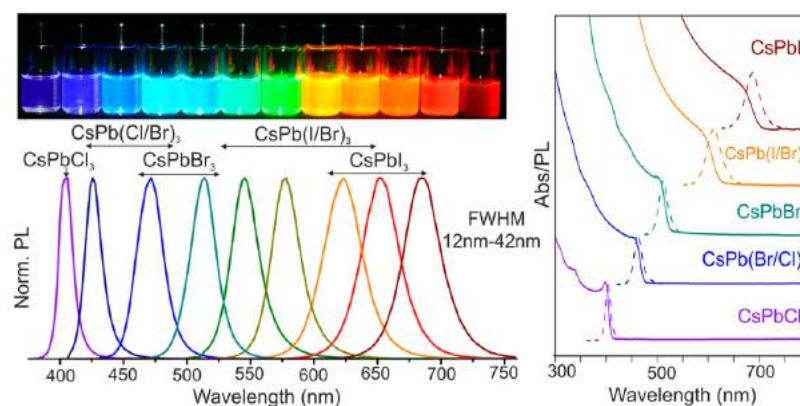
The World of Scintillating Nanomaterials

The world of scintillating nanomaterials comprises a large number of different materials and covers many different categories. Only a small selection is dealt with in this work.

Perovskites, especially caesium lead halide perovskites with the chemical formula CsPbX$_3$, where X denotes the halogen (Cl, Br, I) exhibit many interesting properties, including low cost and ease of synthesis with certain limitations. These semiconducting materials have size- and composition-tunable bandgap energies covering the entire visible spectrum, as shown in Figure 4.5, and are characterized by fast decay times and high light output.

Figure 4.5: Caesium lead halide perovskite (CsPbX$_3$ with X = Cl, Br, I) nanocrystals exhibit size- and composition-tunable bandgap energies covering the entire visible spectrum. ' The top photograph shows solutions of CsPbX$_3$ perovskites in toluene under UV irradiation with $\lambda = 365$ nm. On the left, representative photoluminescent (PL) emission spectra with excitation wavelengths 350 nm for CsPbCl$_3$, and 400 nm for for all others. On the right, typical optical absorption and PL spectra are shown, where the absorption spectra are continuous as dashed lines and the PL emission spectra as plotted lines. The spectra are shifted vertically for clarity. Figure adapted from Protesescu et al. [23].

The control over the properties of NCs can be extended further. To improve their optical properties, NCs consisting of two (or more) different semiconductors can be connected by heterointerfaces, such as core/shell or core/crown structures. Core/shell is a term used for nanomaterials that consist of an inner material that forms a core and an outer material that forms a shell around the core material, whereby the bandgap energies of the shell semiconductors are greater than those of the coated semiconductors. Examples of such structures are CdSe/ZnS or CdSe/CdS.

4.3 Scintillating Nanocomposites

Semiconductor nanocrystals (NCs) are usually produced in the form of solutions and then embedded in host materials such as polymers to form scintillating nanocomposites. As most NCs are sensitive to environmental conditions, for example temperature and humidity, this process forms stable compounds that, to a certain degree, are resistant to external influences, and thus makes them more suitable for wide range of applications. A careful choice of host materials is therefore necessary to fully exploit the properties of nanocrystals in radiation detectors.

In this work different types of scintillating nanocomposites were characterized. These nanocomposites were not produced as part of this work, but were manufactured and provided by collaborating partners. A detailed description of the studied nanocomposites is given in Section 4.4.

Synthesis of Nanocomposites

There are numerous techniques for the production of nanoscintillators. This chapter is limited to the synthesis of nanocomposites selected in the context of this thesis. Some aspects of the synthesis are briefly addressed here so that some characteristics and properties of the scintillating nanocomposites and their behavior can be discussed later. Other techniques as well as the fabrication of QDs and NCs are not explained here. A detailed description can otherwise be found, for example, in Jacak [20] or in Baig [25].

To form a nanocomposite, NCs are embedded in a host polymer or polymer matrix such as polystyrene (PS), poly(vinyltoluene) (PVT) or poly(methylmeth-acrylate) (PMMA). Two main techniques were used for embedding NCs in polymers, as illustrated in Figure 4.6.
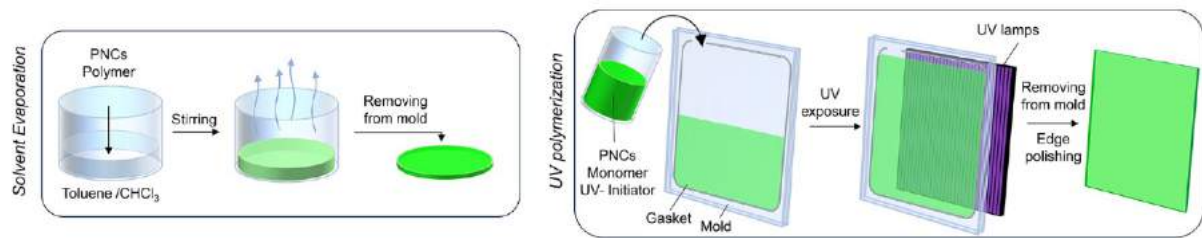
Well-established techniques for NC synthesis are for example the hot injection (HI) and ligand-assisted reprecipitation (LARP) methods [24].

Figure 4.6: Two synthesis techniques, solvent evaporation on the left, "direct polymerization" with UV light on the right. Figure adapted from Anand et al. [26].

The first, and one of the most common and simple techniques, is "solvent evaporation". Synthesized NCs are mixed with a polymer, that is dissolved in a highly volatile solvent such as toluene, filled in a container. The nanocomposite scintillator is obtained by evaporating the solvent, to form a film of hundreds of µm thickness. It is possible to obtain thicker scintillators by adding more solution to the container. However, this method prevents the solvent from easily escaping the solution such that the composite swells, resulting in an irregular thickness and surface with a bubble texture, and possibly not completely dried zones. This constitutes already the biggest disadvantage of this technique. It is not yet possible to produce large and thick scintillators, which makes it difficult for use in calorimetry where large scintillators are required. On the other hand, this technique allows the production of nanocomposites with higher NC concentrations compared to other techniques. However, it should be noted, that higher NC concentrations result in lower transparency of the scintillator. In this work, nanocomposites of perovskites produced by this technique were characterized.

A second common technique is "direct polymerization". In this case the synthesized NCs are mixed with a monomer and filled in a container. The polymerization is then induced either by irradiation of UV light or by thermal curing. In case perovskites are used as nanocrystals temperature curing is excluded since their are very sensitive to heat. However, if UV polymerization is used for the curing process, the NC concentration in the polymer is limited, due to the fact, that high concentration would lead to a high absorption of UV light by the NCs themselves, such that the monomer would not polymerize entirely, resulting in an uneven composite. In this work, nanocomposites of perovskites produced by this technique were evaluated. Figure 4.7 shows these perovskites in solution,

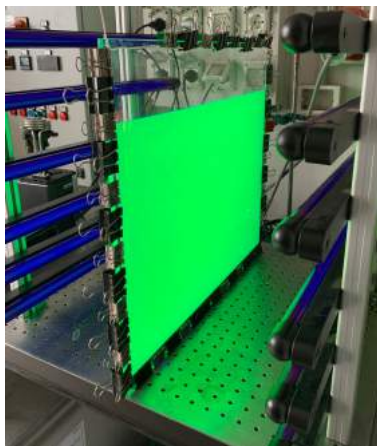**Figure 4.7:** CsPbBr$_3$ perovskite nanocrystals in solution.

Figure 4.8: Polymerization process under UV curing of CsPbBr$_3$ perovskite nanocrystals in a monomer. Figure from Erroi, Frank et al. [27].

Figure 4.9: CsPbBr$_3$ perovskite nanocrystals in a polymer in ambient light. Figure from Erroi, Frank et al.,[27].

while the polymerization process under UV curing is shown in Figure 4.8. The resulting nanocomposite is shown in Figure 4.9. Furthermore, nanocomposites made of cadmium-doped zinc sulfide (CdZnS) and zinc sulfide (ZnS) or hafnium oxide (HfO$_2$) and polymerized using thermal curing, were also characterized.

Ligands are molecules or organic ions that bind to metal atoms or ions. They are essential components for synthesis, processing and applications of nanomaterials, where they bind to the surface of NCs in order to stabilize them and compensate for their high surface-to-volume ratio. The interaction between NCs and ligands is crucial for the optoelectronic properties of QDs. Therefore, the variation of ligand concentration, type and chain length, can significantly influence the structure, size, shape, and optical properties and stability of NCs. Long-chain organic molecules, by acting as surface ligands, especially oleic acid (OA) and oleylamin (OLAM), are typically used in the synthesis of NCs to adjust their size and shape. On the other hand, these long-chain ligands act as electronic insulators impeding charge carrier injection and transport at the NC/ligand interface. Therefore, these insulating, weakly bound, long-chain molecules must be exchanged for shorter ones if better charge transfer is required, or for ligands having a stronger bond to the NC-surface if higher stability is required. This can be done by what is called ligand exchange [24].

The main drawbacks of NCs are their small size to efficiently absorb the incident ionizing radiation and their low Stokes shift. This means that in composites thick enough to provide good stopping power, most of the emitted light is lost due to self-absorption. The biggest challenge is to produce nanocomposites with a high filling factor of NCs while maintaining good transparency. As with organic scintillators (Section 3.2), doping with fluorescent dyes can also be useful to reduce self-absorption and thus increase light yield. In summary, choosing the right components to produce nanocomposites with high stability, excellent photophysical properties and optoelectronic efficiencies still remains a challenge.

4.4 Studied Nanoscintillators

Nanoscintillators relevant to this work are described in detail and then summarized in Table 4.1.

CsPbBr$_3$ Perovskite Nanoscintillators

Cesium lead bromide (CsPbBr$_3$) nanocrystals were embedded in poly-(methylmeth)acrylate/(poly)laurylmeth-acrylate (PMMA/PLA) with a ratio of 80:20 wt % with the addition of 2,2-dimethoxy-2-phenylaceto-phenone (0.33 wt %). Five different samples with different filling factors (see Table 4.1) were made. They were produced by the University of Milano-Bicocca (UNIMIB), Milan, Italy [27]. Each individual concentration of native CsPbBr$_3$ was dispersed in methylmethacrylate/laurylmeth-acrylate and mixed with the radical photoinitiator irgacure 651 (0.33 wt %). This mixture was then irradiated with UV light of 365 nm wavelength to initiate free radical polymerisation to produce a solid scintillator [27].

CsPbBr₃ Perovskite Nanoscintillator Platelets

In this case CsPbBr$_3$ nanocrystals were embedded in polystyrene (PS) with three different filling factors (see Table 4.1). Two sets of such nanocomposites were produced by the Czech Technical University (CTU) in Prague, Czech Republic [28]. The nanocrystals were synthesized with different surface ligands of oleic acid (OA) and oleylamine (OLAM) using a standard hot injection technique according to Protesescu et al. [23] modifying the procedure introduced by Lu et al. [29]. Then, one set was prepared using a technique [30] that exchanged ligands of didodecyldimethylammonium bromide (DDAB) on the nanocrystals. Following this PS was dissolved in toluene, mixed with each appropriate amount of CsPbBr$_3$ nanocrystals. The toluene was evaporated in air at room temperature to form a film of scintillator with a thickness of about 100 µm [28] [31]. The two sets of obtained nanocomposites are shown in Figure 4.10.
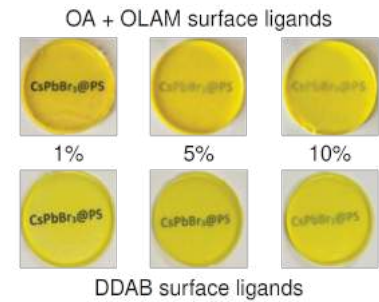

Figure 4.10: Photographs in ambient light of CsPbBr$_3$ nanocrystals embedded in PS with different filling factors and two different surface ligands, OA + OLAM and DDAB. The percentage indicates the filling factor. Figure adapted from Děcká, Frank et al. [28].

CdZnS/ZnS Nanoscintillators

Cadmium-doped zinc sulfide (CdZnS) and zinc sulfide (ZnS) nanocrystals with core/shell structure were embedded in poly(vinyltoluene) (PVT) with the addition of 4,7-bis2'-9',9'-bis[(2'''-ethylhexyl)fluorenyl]-2,1,3-benzothiadiazole (FBTF) (2 wt %). The structure of FBTF is shwon in Figure 4.11.
Five different nanocomposites with different filling factors (Table 4.1) were made. They were produced by the University of California (UCLA) in Los Angeles, USA [32]. The nanocrystals with a core of Cd$_{0.5}$Zn$_{0.5}$S of about 3.5 nm diameter and a shell of ZnS with 1.25 nm thickness were synthesized with OA ligands. Bis[2-(methacryloyloxy)ethyl] phosphate (BMEP) was introduced to partially replace the OA ligands on the surface of the nanoparticles. Each individual concentration of the modified nanocrystals was then dissolved in vinyltoluene (VT) along with FBTF. The polymerization was done by thermal curing. A schematic of the fabrication is shown in Figure 4.12 [32].
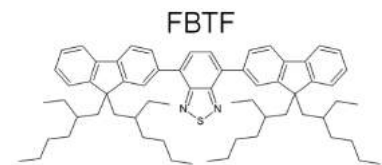

Figure 4.11: Structure of 4,7-bis2'-9',9'-bis[(2'''-ethylhexyl)fluorenyl]-2,1,3-benzothiadiazole (FBTF). Figure from Liu et al. [32].
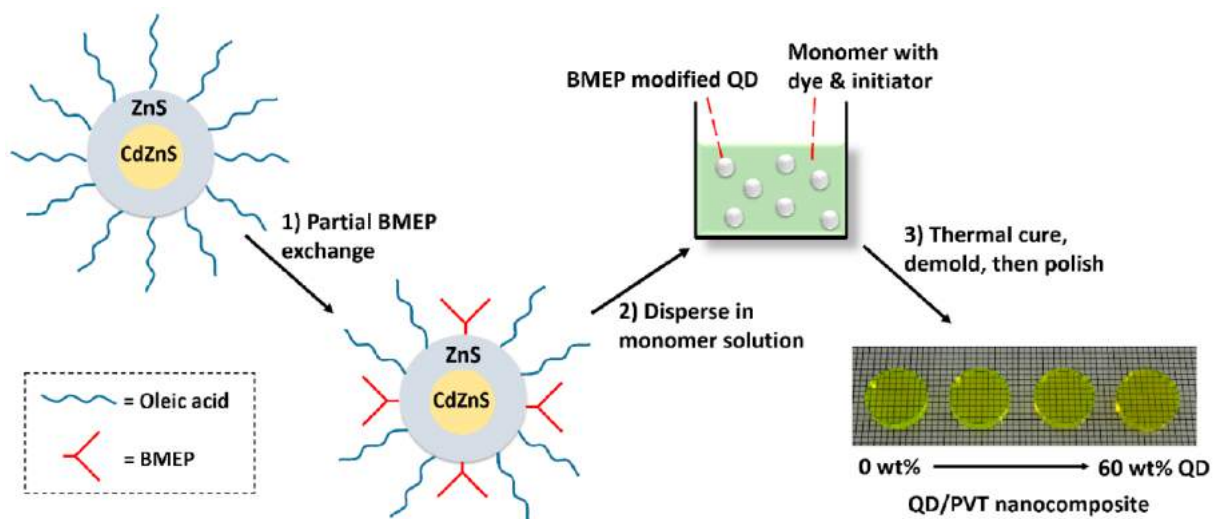

Figure 4.12: Illustration of the fabrication of CdZnS/ZnS nanocrystals with core/shell structure embedded in PVT/FBTF. The photograph on the lower right side shows the nanocomposites with 10 mm diameter and 2 mm thickness, and different filling factors, varying from 0 to 60 % at 20 % increment. Figure from Liu et al. [32].
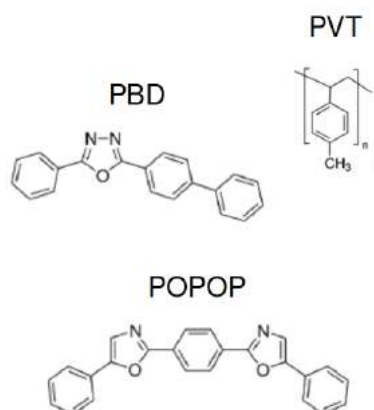
PVT

PBD

POPOP

Figure 4.13: Structures of poly(vinyltoluene) (PVT), 2-(4-tert-butylphenyl)-5-(4-biphenylyl)-1,3,4-oxadi-azole (PBD), and 1,4-bis(5-phenyl-2-oxazolyl)benzene (POPOP). Figure adapted from Han et al.[35].

HfO$_2$ Nanoscintillator

Hafnium oxide (HfO$_2$) nanocrystals were embedded in PVT with the addition of 2-(4-tert-butylphenyl)-5-(4-biphenylyl)-1,3,4-oxadi-azole (PBD) (2 wt %) and 1,4-bis(5-phenyl-2-oxazolyl)benzene (POPOP) (0.01 wt %) to form a nanocomposite with 20 wt % filling factor (see Table 4.1). The structures of single materials are shwon in Figure 4.13. This nanocomposite was produced along with the previously described samples by UCLA [33] [34]. The nanocrystals were synthesized with OLAM ligands, then modified with BMEP ligands exchange. The modified nanocrystals were then dissolved in vinyl-toluene (VT) along with PBD and POPOP. The polymerization was done by thermal curing [33].

(PEA)$_2$PbBr$_4$ Perovskite Nanoscintillators

In addition to nanocomposites a set of hybrid organic–inorganic perovskites (HOIPs) was produced by CNRS - International - NTU - Thales Research Alliance (CINTRA) at the Nanyang Technological University, Singapore [36]. These lithium doped (Li-doped) and undoped 2D perovskite crystals were prepared with a solution method. An undoped precursor solution was prepared by dissolving the same amount of phenethylammonium bromide ((PEA)Br) and lead bromide (PbBr$_2$) in dimethyl sulfoxide (DMSO). The DMSO was then evaporated at ambient temperature to form the crystal. Subsequently, the crystal was washed with diethyl ether and dried under vacuum. For the Li-doped crystal lithium bromide (LiBr) was added to the undoped precursor solution with an expected Li:Pb ratio of 4 %. The same production steps as for the undoped crystal were then followed to produce the doped crystal [37]. The structure of these crystals consists of inorganic [PbBr$_6$]$^{4-}$ - octahedra sheets separated by a layer of organic ammonium cations [36], as shown on the left in Figure 4.14. A typical characteristic of these crystals is that they are brittle and fragile and also irregular in shape and size. Photographs of Li-doped (PEA)$_2$PbBr$_4$ single crystals are shown on the right in Figure 4.14.
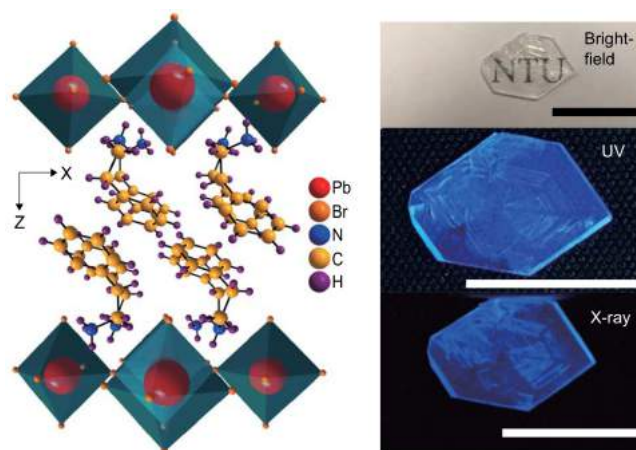
Figure 4.14: On the left, structure of (PEA)$_2$PbBr$_4$ perovskite crystals. On the right, photograph of Li-doped (PEA)$_2$PbBr$_4$ single crystals under brightfield, UV light of 365 nm, and X-ray excitation. The black and white bars are 1 cm in length. Figure adapted from Xie et al. [37].

Table 4.1: Overview of the nanoscintillators studied in this work. They mainly consist of nanocomposites, which are nanocrystals embedded in polymers. c_{NC} denotes the filling factor.

Material	Nanocrystal	c_{NC} [wt %]	Polymer	Dye	Producer
$CsPbBr_3$ in PMMA/PLA	$CsPbBr_3$	0.05	PMMA/PLMA	–	UNIMIB
$CsPbBr_3$ in PMMA/PLA	$CsPbBr_3$	0.1	PMMA/PLMA	–	UNIMIB
$CsPbBr_3$ in PMMA/PLA	$CsPbBr_3$	0.2	PMMA/PLMA	–	UNIMIB
$CsPbBr_3$ in PMMA/PLA	$CsPbBr_3$	0.4	PMMA/PLMA	–	UNIMIB
$CsPbBr_3$ in PMMA/PLA	$CsPbBr_3$	0.8	PMMA/PLMA	–	UNIMIB
$CsPbBr_3$ in PS (OA+OLAM)	$CsPbBr_3$ (OA+OLAM)	1	PS	–	CTU
$CsPbBr_3$ in PS (OA+OLAM)	$CsPbBr_3$ (OA+OLAM)	5	PS	–	CTU
$CsPbBr_3$ in PS (OA+OLAM)	$CsPbBr_3$ (OA+OLAM)	10	PS	–	CTU
$CsPbBr_3$ in PS (DDAB)	$CsPbBr_3$ (DDAB)	1	PS	–	CTU
$CsPbBr_3$ in PS (DDAB)	$CsPbBr_3$ (DDAB)	5	PS	–	CTU
$CsPbBr_3$ in PS (DDAB)	$CsPbBr_3$ (DDAB)	10	PS	–	CTU
CdZnS/ZnS in PVT/FBTF	CdZnS/ZnS	40	PVT	FBTF	UCLA
CdZnS/ZnS in PVT/FBTF	CdZnS/ZnS	50	PVT	FBTF	UCLA
CdZnS/ZnS in PVT/FBTF	CdZnS/ZnS	56	PVT	FBTF	UCLA
HfO_2 in PVT/PBD/POPOP	HfO_2	20	PVT	PBD/POPOP	UCLA
$(PEA)_2PbBr_4$	$(PEA)_2PbBr_4$	–	–	–	CINTRA
Li-doped $(PEA)_2PbBr_4$	$(PEA)_2PbBr_4$	–	–	–	CINTRA

4.5 Nanomaterials in Calorimetry

This work is focused on the investigation of nanomaterials that may later be used in calorimetry. There are two possible applications for these materials.

A classic application of nanomaterials as active material in calorimetry could be in a sampling calorimeter. Nanomaterials that feature higher stopping power and thus higher light yield, faster timing and being more resistant to radiation could replace plastic scintillators in such a calorimeter. A prerequisite here is to find suitable materials.

 A first application of nanomaterials in such a sampling calorimeter was made within the "NanoCal" project, which is discussed in detail in Chapter 7. A new concept of using nanomaterials in a so-called chromatic calorimeter [40] is also presented.

The "NanoCal" project [38] is part of the European Union's Horizon 2020 Research and Innovation programme (AIDAinnova) [39].

Characterization Methods | 5

In this chapter, materials and methods for the characterization of scintillators are presented. The readout electronics used to enable very high resolution timing measurements are explained first, followed by a description of photodetectors and the description of the measurement setups and analysis techniques to investigate the performance of nanoscintillators. The characterization includes measurements of the optical properties, light output and timing measurements. However, standard characterization methods for scintillation properties based on radiation sources with an energy range of several hundred keV, such as classical CTR measurements with 511 keV, are not suitable for most of these nanomaterials due to their low stopping power. Therefore timing measurements were made using a soft (up to 40 keV) pulsed X-ray source. This method of characterization led to a publication: "A new method to characterize low stopping power and ultra-fast scintillators using pulsed X-rays" in Frontiers in Physics [41].

5.1 Readout Electronics

A special readout electronics for low-noise and ultra-high speed for photon measurements, originally developed by Cates et al. [42] and further refined by Gundacker et al. [43], was used for most of the timing measurements in this work. Its printed circuit board (PCB) with electronic components is illustrated in Figure 5.2. A schematic of its functional principle is shown in Figure 5.1. Splitting the incoming signal into two separate branches – one for determining the energy (energy signal) and one for the time over threshold determination (timing signal) – allows to achieve the best energy and timing resolution for both cases independently, and thus enables very high resolution timing measurements.

Crucial to the amplifier's timing branch is the application of a Macom MABA-007159-000000 [44] transmission line transformer, also called balun transformer, that was already introduced by Cates et al. [42]. Two Infineon BGA616 [45] silicon germanium broadband MMIC amplifiers provide a two-stage amplification. On the other hand, amplification in the energy branch of the amplifier is made by a standard Analog Devices AD8000 [46] ultra high speed operational amplifier having negligible influence on the timing channel bandwidth nor introducing additional electronic noise [43].
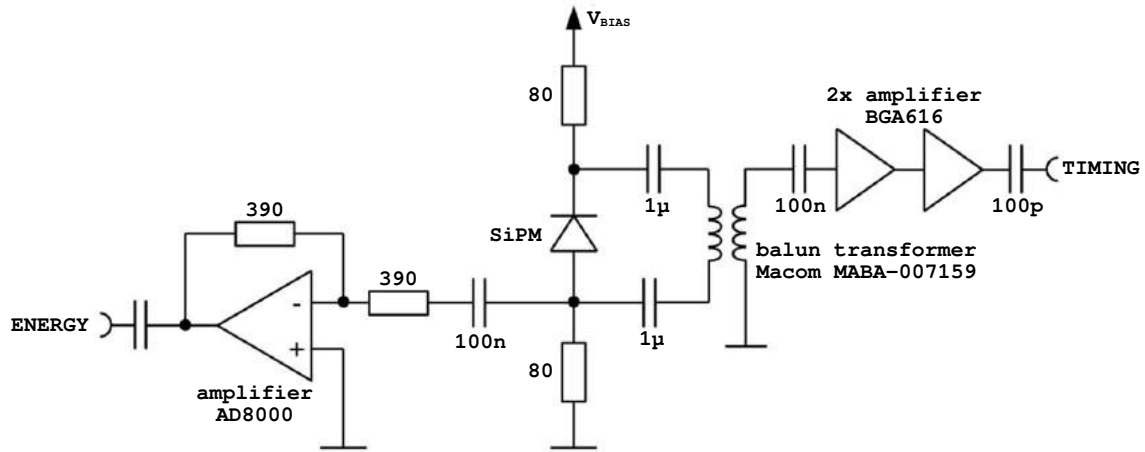
Figure 5.1: Functional Principle of the readout electronics with the energy branch to the left of the SiPM and the timing branch to the right of the SiPM. Schematic adapted from Gundacker et al. [43].
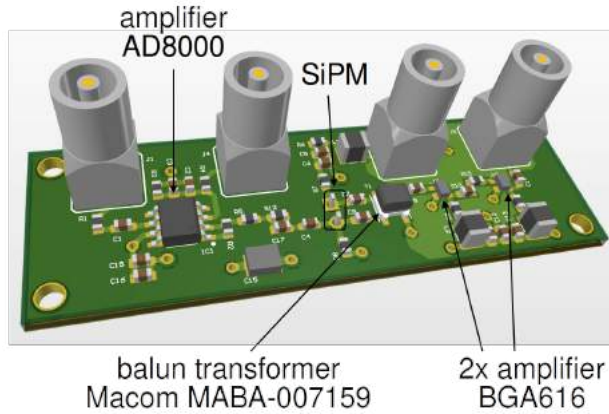

Figure 5.2: Equipped PCB of the readout electronics with electronic components. The position of the main components such as the two different amplifiers and the balun transformer as well as the pin of the SiPM on the back of the PCB are high-lighted.

The high amplification of the SiPM signal in the timing branch causes it to saturate, which can be neglected and is even intended to obtain a strong rising edge of the signal. From this rising edge the rise time can be determined. It is defined as the time difference between two voltage levels V_{th_1} and V_{th_2} belonging to two different thresholds th_1 and th_2, as illustrated in Figure 5.4 and given by
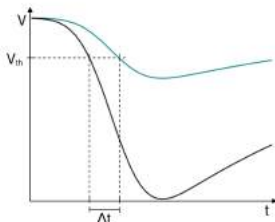

Figure 5.3: With a leading edge threshold large signals pass a given threshold V_{th} earlier than small signals. The result in a time walk Δt.

$$t_{\text{rise}} = t(V_{\text{th}_2}) - t(V_{\text{th}_1})\,, \tag{5.1}$$

with $\quad V_{\text{th}_1} < V_{\text{th}_2} \quad$ and $\quad t(V_{\text{th}_1}) > t(V_{\text{th}_2})\,.$

Having a stronger rising edge results in a smaller rise time. On the other hand, the smaller amplification of the SiPM signal in the so-called energy branch enables a higher resolution and linearity of the entire SiPM pulse and can therefore be used for the energy determination.

With a leading edge threshold large signals pass a given threshold V_{th} earlier than small signals. This results in a time walk Δt, as illustrated in Figure 5.4. All measurements will be corrected for this effect.

For a given start signal, the SiPM output is used as a stop signal, whereby the timing signal is used because it exceeds the threshold earlier than the energy signal. In that case also the time walk is reduced to a minimum. Figure 5.5 shows the two SiPM signals.
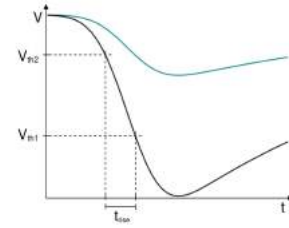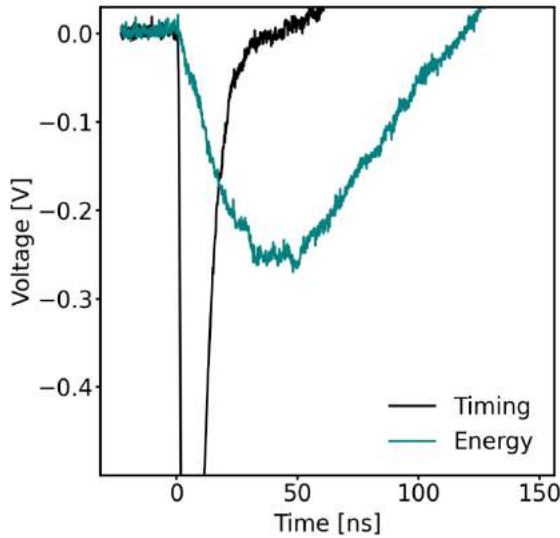

Figure 5.4: The rise time is defined as the time difference between two voltage levels V_{th_1} and V_{th_2} belonging to two different thresholds th_1 and th_2.

Figure 5.5: Both SiPM signals – timing and energy – from the readout electronics with the same division in time and voltage direction. The high amplification of the timing signal leads to a stronger rising edge and thus to a shorter rise time compared to the energy signal, in which the entire SiPM pulse is resolved. For a given start signal, the SiPM timing signal is used as a stop signal, also to reduce the time walk to a minimum.

5.2 Photodetectors

Scintillators are usually coupled to photodetectors, such as photomultiplier tubes or silicon photomultipliers which have the function to convert scintillation photons into electronic signals. The photodetector output signals are typically fed into readout electronics such as these described above or (pre)amplifiers, analyzers or computers.

Photomultiplier Tubes

Photomultiplier tubes (PMTs) belong to the class of vacuum photodetectors and are in production since the late 1930s. They are well described in literature, for example in Knoll [15]. Its functional principle is shown in Figure 5.6.

The scintillation photon enters the PMT, which is held under vacuum, through an entrance window behind which is placed the photocathode. When a photon hits the photocathode, an electron is emitted by the photoelectric effect into the vacuum. This electron is called photoelectron. The generated photoelectron is then accelerated and focused by the focusing electrode onto the first dynode, where the first multiplication of secondary electrons takes place. This secondary emission is repeated on each of the successive dynodes, where the dynode stages are biased
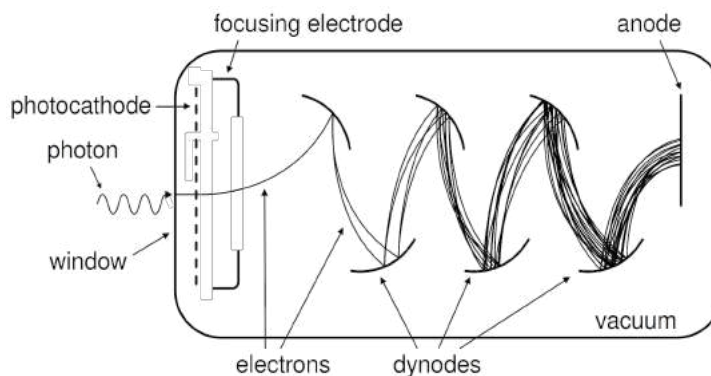
Figure 5.6: Functional principle of a photomultiplier tube.

with an increasing potential in order to create an accelerating electric field between the photocathode and the anode. The electrons emitted from the last dynode are finally collected by the anode which provides the signal current that is passed on to an external readout. PMTs have a gain typically in the range of 10^6 to 10^7 [3]. The detection efficiency of a PMT depends mainly on the quantum efficiency (QE). Therefore the QE is one of the key parameter of a PMT with typical values between 20 and 30 % [15].

It is defined as the ratio of the number of photoelectrons emitted by the cathode to the number of photons incident on the window and is usually expressed as a percentage by

$$QE = \frac{n_{\text{photoelectrons}}}{n_{\text{photons}}} \, , \tag{5.2}$$

where n_{photons} is the number of incident photons, and $n_{\text{photoelectrons}}$ the number of photoelectrons.

The quantum efficiency depends on the material of the photocathode and the wavelength of the incident photon. As an example, the QE of a Hamamatsu R205 PMT is shown in Figure 5.14.

Silicon Photomultipliers

Silicon photomultiplier (SiPMs) or multi pixel photon counters (MPPCs) are solid-state photodetectors and consist of many single avalanche photodiodes (SPADs) operating in Geiger-mode.

A SPAD is a diode or a p-n junction to which a bias voltage is applied. An incident photon to creates an electron-hole pair in the junction. Depending on the applied voltage there are three different regions of operation, as shown in Figure 5.7.

At low voltage, there is no additional multiplication of the generated electron-hole pairs, the diode operates in the photodiode range. By increasing the applied voltage, the electric field becomes high enough to enable secondary electron-hole pairs via impact ionization. This is the range where avalanche photodiodes (APDs) are operated with a gain from ten to several hundreds with very high linearity. Since the mobility of the holes is much lower than that of the electrons, they do not gain enough energy in this regime to create new electron-hole pairs
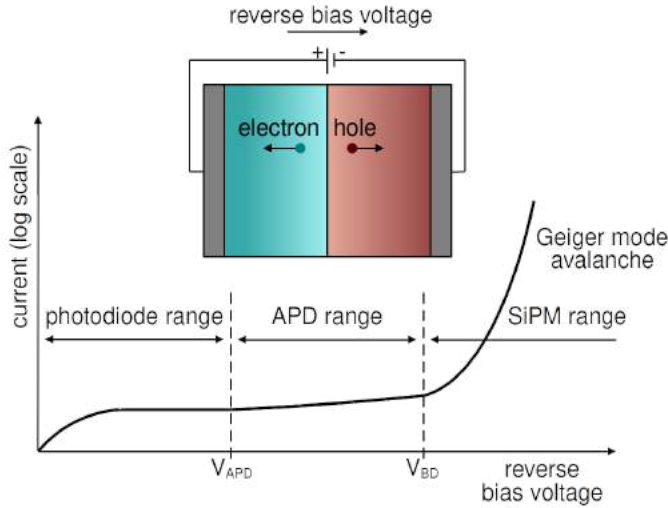
and therefore do not contribute to the signal gain of the device. The electron avalanche therefore only flows in one direction, is self-quenched, and does not require an external circuit to be stopped, as shown on the left in Figure 5.8. If the applied bias voltage is increased even further, above the so-called breakdown voltage, the device is operated in the Geiger mode, the range used in SiPMs. In this case, the holes also gain enough energy to generate new electron-hole pairs themselves. This is shown on the right of Figure 5.8. This effect makes it possible for just one photon to trigger a self-sustaining avalanche, which must be quenched by an external current-limiting circuit to become sensitive again for a subsequent photon impact.
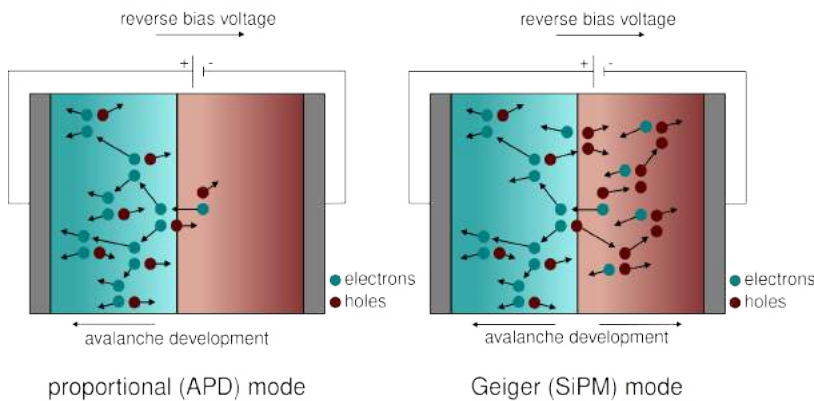
A SiPM is an array of SPADs, electrically connected in parallel, where each SPAD fires individually when hit by a photon. The device is externally biased so that the voltage on each SPAD is above its breakdown voltage to operate in Geiger mode responsible for a fast and high output signal.

The difference between the bias voltage V_{BIAS} and the breakdown voltage V_{BD} is known as overvoltage:

$$\Delta V = V_{\mathrm{BIAS}} - V_{\mathrm{BD}} \qquad \text{with} \qquad V_{\mathrm{BIAS}} > V_{\mathrm{BD}} \,. \tag{5.3}$$

It is the main adjustable parameter that controls the operation of the device.

SiPMs have a gain typically in the range of 10^5 to 10^6 [3]. The quantum efficiency of a SiPM is defined as the probability of generating an electron-hole pair per incident photon. It can reach higher values compared to PMTs, with typical values between 15 and 40 % [3]. This leads to a higher photon detection efficiency (PDE) which is defined as the probability that a SiPM produces an output signal in response to an incident photon. It is a function of overvoltage ΔV and wavelength λ of the incident photon, expressed by

$$PDE(\Delta V \mid \lambda) = f \cdot QE \cdot P_{\text{trigger}} \tag{5.4}$$

1: The geometric fill factor is the ratio between the photosensitive area and the total active area of a SiPM.

2: The avalanche trigger probability is the probability of an electron or hole to initiate an avalanche in the microcell. It is dependent on the bias overvoltage and increases with increasing bias overvoltage.

where f is the geometrical fill factor [1], QE the quantum efficiency, and P_{trigger} the avalanche trigger probability [2].

The photon detection efficiency is a key characteristic of a SiPM. Higher PDE can lead to potentially better energy and time resolution. A detailed description of SiPMs can be found in Acerbi et al. [48] and in Gundacker et al. [47].
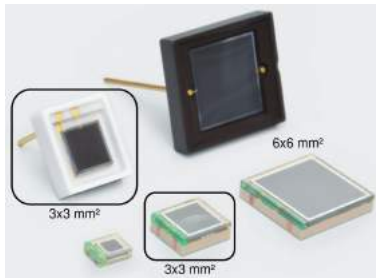
SiPMs and PMTs are similar in their properties and characteristics. Both have comparable gain, where SiPMs generally have higher dark currents. Compared to PMTs, SiPMs require a considerably lower operating voltage, achieve higher quantum efficiencies, typically up to around 70 % [4], they are also insensitive to magnetic fields, sturdier and more robust. On the other hand SiPMs are smaller in size with a considerably smaller active area which limits their use for large size scintillators. They are smaller in size, but thus also have smaller active areas, which is disadvantageous for large-size scintillators, for example.

In this work, SiPMs of type S13360 from Hamamatsu, shown in Figure 5.9, and SiPMs of type AFBR-S4N33C013 from Broadcom were mainly used, both types with an active area of $3 \times 3 \, \text{mm}^2$ size and a SPAD size of $50 \, \mu\text{m}$. To achieve the best possible time resolution the SiPMs, they are often operated at up to $10 \, \text{V}$ overvoltage.

Figure 5.9: SiPMs of type S13360 from Hamamatsu. Types S13360-3050PE and S13360-3050CS with an active area of $3 \times 3 \, \text{mm}^2$ were used in this work. They have a SPAD size of $50 \, \mu\text{m}$, a PDE of 40%, a gain of 1.7×10^6 and a breakdown voltage of $V_{\text{BD}} = 53 \, \text{V}$ [49]. Figure adapted from Hamamatsu [49].

5.3 Photoluminescence and Radioluminescence

Photoluminescence (PL) emission and excitation spectra were determined using a PerkinElmer LS55 luminescence spectrometer. A schematic of the optical system of the device is shown in Figure A.1 in Appendix A.1. The device was equipped with a xenon flash lamp operating, covering a wavelength range from 200 to 900 nm with 1 nm accuracy.Both spectra show the change in intensity as a function of wavelength. By setting a wavelength with known absorption by the scintillator, the wavelength is scanned over the desired emission range and the intensity recorded as a function of emission wavelength to obtain the emission spectrum. For the excitation spectrum the wavelength is set to a wavelength with known emission of the sample, and the wavelength is scanned over the desired excitation range and the fluorescence intensity is recorded on the detector as a function of excitation wavelength.

For the nanocomposites made of $CsPbBr_3$ embedded in PS, the PL emission and excitation spectra were determined using a Horiba Scientific FluoroMax spectrofluorometer. The device was equipped with an ozone-free xenon lamp and a R928P photon counting PMT, covering a wavelength range from 185 to 850 nm with 0.5 nm accuracy. For the same scintillators, the radioluminescence (RL) emission spectra were determined using a Horiba Scientific 5000M spectrofluorometer, equipped with a Seifert X-ray tube as excitation source, operating at 40 kV, a monochromator, and a IBH Scotland TBX-04 photodetector [28].

For the nanocomposites made of $CsPbBr_3$ embedded in PMMA/PLA, the RL emission spectra were determined using a customized device. This device was cryogenic cooled with liquid nitrogen and equipped with an UV-enhanced charge-coupled HORIBA Scientific Symphony II device, coupled to a Horiba Scientific Triax 180 spectrometer. The nanocomposites were beforehand excited with X-rays of a Philips PW2274 tungsten X-ray tube, equipped with a beryllium window, operating at 20 kV [27].

5.4 Transmission

The transmission was measured with a PerkinElmer Lambda 650 UV/VIS spectrophotometer [50], as shown in Figure 5.10. A schematic of the optical system of the device is shown in Figure A.2 in Appendix A.2. The device was equipped with a deuterium and a halogen light source whose light was passed through optical gratings to select the desired wavelength for the measurement, covering a range from 190 to 900 nm, variable in 1 nm steps. The light beam was split into two, with one beam, the reference beam, being sent/guided directly to the photodetector and the second through the scintillator to the photodetector. By comparing the light intensity with and without the scintillator the transmittance of the scintillator was determined as a function of wavelength.
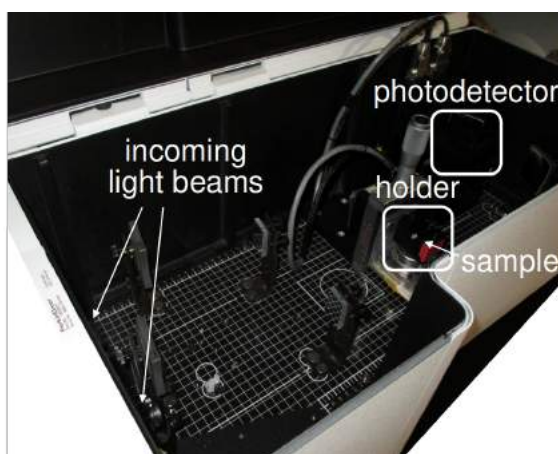

Figure 5.10: Photograph of the PerkinElmer Lambda 650 UV/VIS used for transmission measurements. In addition to the position of the incident light beams, a sample on its holder and the photodetector, parts of the optical system are also visible.

For the nanocomposites made of $CsPbBr_3$ embedded in PMMA/PLA, optical absorption measurements were made using a Cary 50 UV/VIS spectrophotometer [27].

Besides the length of a scintillator, both uneven surfaces of the scintillator and effects due to misalignment of its surface not being perfectly perpendicular to the beam can lead to losses in the transmittance. For scintillators with a refractive index different from that of air Fresnel reflection, as described in Section 3.3, occurs at the air/scintillator interface. This also leads to losses in light, appearing as a constant absorption in the transmission spectrum. In addition, the cross section of the light beam should be reduced to less than the surface area of the scintillator in order to prevent light from bypassing outside the scintillator.

5.5 Light Output with Gammas

The light output was measured using ^{137}Cs emitting gammas at 661.7 keV energy. A Hamamatsu R2059 PMT was biased at 2500 V, so as to provide sufficient gain to resolve single photoelectrons and to collect the total charge of photoelectrons generated in a 661.7 keV scintillation event. The PMT was connected to a CAEN DT5720 digitizer. An analog signal attenuator was used to avoid pulse saturation of the PMT signal. The whole setup was enclosed in a temperature controlled dark box held at a constant temperature of 18 °C ± 0.5 °C. The experimental setup is shown in Figure 5.11 and Figure 5.12.

First, a calibration was performed, measuring the signal produced by a single photoelectron escaping the photocathode to obtain the dark noise spectrum. For that the PMT was biased and covered with a lid and a measurement was done without source and scintillator. The mean of the Gaussian fit corresponds to the channel of one photoelectron, and is later used to calculate the light yield of the scintillator.

Gaussian distribution:

$$f(x) = \frac{1}{\sigma\sqrt{2\pi}} \exp\left(-\frac{1}{2}\left(\frac{x-\mu}{\sigma}\right)^2\right)$$

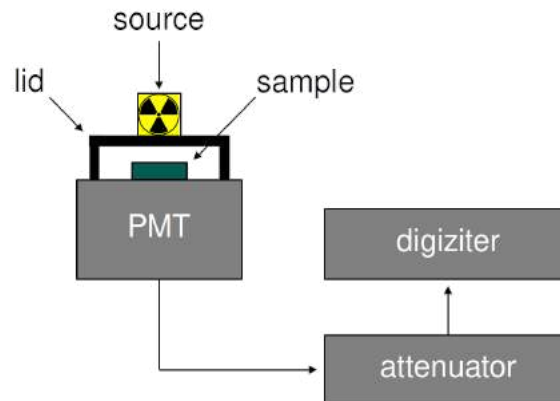with mean μ and standard deviation σ.

Figure 5.11: Schematic of the experimental setup to measure the light output of a scintillator using a ^{137}Cs source emitting gammas at 661.7 keV. An analog signal attenuator was used to avoid pulse saturation of the PMT signal.

After obtaining the dark noise spectrum, a measurement was done with the scintillator. In order to maximize the light collection, the scintillator was wrapped in Teflon on all sides except the readout side which was connected to the PMT. The scintillator was attached to the PMT window either via 'air' coupling or using Rhodorsil grease as optical coupling, having a refractive index of $n = 1.41$. To shield the PMT glass from external light, the PMT and the scintillator were covered with a lid, and the source was placed on top. Figure 5.13 shows an example of the light output spectrum.

Figure 5.12: Photograph of the experimental setup to measure the light output of a scintillator using ^{137}Cs emitting gammas at 661.7 keV energy.
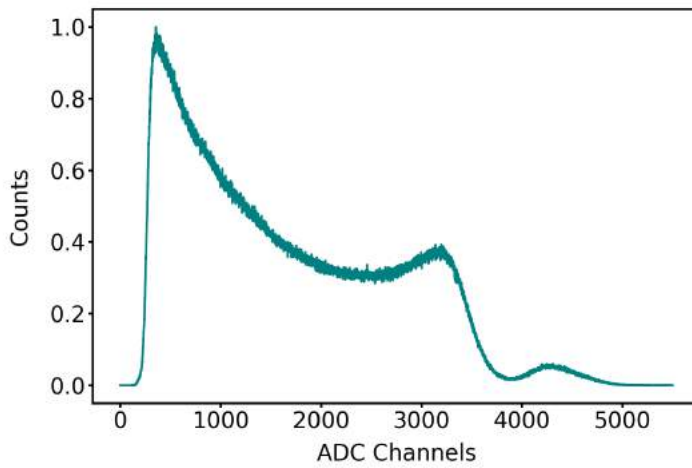

Figure 5.13: An example of an energy spectrum obtained using ^{137}Cs. The photopeak at around 4 300 ADC channels was fitted with Equation 5.5.

The photopeak in the spectrum was fitted with a function given by

$$f(x) = p_0 \cdot \exp\left[-\frac{1}{2}\left(\frac{x-p_1}{p_2}\right)^2\right] + \frac{p_3}{\sqrt{1 + \left(\frac{x}{p_4}\right)^{p_5}}} \qquad (5.5)$$

with position x in ADC channels and fit parameters p_i.

The number of photons impinging on the PMT was corrected for the average quantum efficiency of the PMT and calculated from the average of the emission spectrum of the scintillator weighted by the quantum efficiency:

$$< QE > = \frac{\int_{\lambda_{\min}}^{\lambda_{\max}} d\lambda\, QE(\lambda) \cdot I(\lambda)}{\int_{\lambda_{\min}}^{\lambda_{\max}} d\lambda\, I(\lambda)} \,, \qquad (5.6)$$
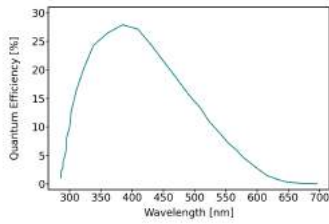
Figure 5.14: Quantum efficiency as a function of wavelength of the Hamamatsu R2059 PMT, which reaches a maximum value of 28 %.

The energy resolution in high energy physics is often given in standard deviation σ. FWHM and σ are related as follows: $FWHM = 2\sqrt{2\ln 2}\,\sigma \approx 2.355\,\sigma$.
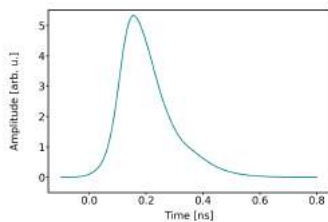
where I is the emission spectrum of the scintillator, and QE the quantum efficiency of the PMT, which is shown in Figure 5.14.

The light output LO was then calculated by

$$LO = \frac{1}{E_\gamma} \cdot \frac{\mu_{sample} \cdot C_{sample}}{\mu_{SPE} \cdot C_{SPE}} \cdot 10^{\frac{A}{20}} \cdot \frac{1}{< QE >} ,\tag{5.7}$$

where $E_\gamma = 661.7\,\mathrm{keV}$, μ_{sample} and μ_{SPE} are the ADC channels corresponding to the photopeak position of the scintillator and the single photoelectron pulse, C_{sample} and C_{SPE} are the charge sensitivity values of the digitizer used for the scintillator and single photo electron measurement, A the attenuation and $< QE >$ the mean quantum efficiency of the PMT. C_{SPE} and C_{sample} were set to 40 for all measurements.

Furthermore, the energy resolution of a scintillator can be derived from this measurement. It is defined as the ratio of the energy fluctuation ΔE at half maximum (FWHM) to the peak value E. It is usually expressed as a percentage and calculated by

$$\frac{\Delta E}{E} = \frac{FWHM(E)}{E} .\tag{5.8}$$

5.6 Scintillation Kinetics with X-rays

The properties of the scintillation kinetics such as rise and decay times were measured in time correlated single photon counting (TCSPC) mode under pulsed X-ray excitation. The experimental setup is shown in Figure 5.16 [41], and a photograph of the setup in Figure 5.21. The scintillator was excited with X-rays of a Hamamatsu XRT N5084 pulsed tungsten X-ray tube operating at 40 keV, where a PicoQuant PDL 800-B pulsed diode laser with 40 ps pulse width (FWHM) acted as the excitation source of the X-ray tube. The energy spectrum of the produced X-rays ranged from 0 to 40 keV with a pronounced peak between 9 and 10 keV, characteristic for the tungsten X-rays, and a mean energy of about 15 keV. The scintillator was placed close to the exit window of the X-ray tube. A Becker & Hickl HPM 100-07 hybrid photomultiplier tube was used to detect the arrival time of the scintillation light, which was processed by an ORTEC 9327 amplifier and timing discriminator, acting as the stop signal for a Cronologic xTDC4 time-to-digital-converter (TDC). The external trigger of the pulsed laser served as the start signal. The overall impulse response function (IRF) of the system was obtained from the convolution of the measured IRF of laser and hybrid PMT with the IRF of the X-ray tube [51], as shown in Figure 5.15, resulting in around 160 ps FWHM. To suppress potential air excitation contributions by X-rays (below around 400 nm) optical filters such as low pass filters of 420 nm or bandpass filters, according to the emission spectrum of the scintillator, were mounted in front of the hybrid PMT. An example of a scintillation distribution is shown in Figure 5.17.
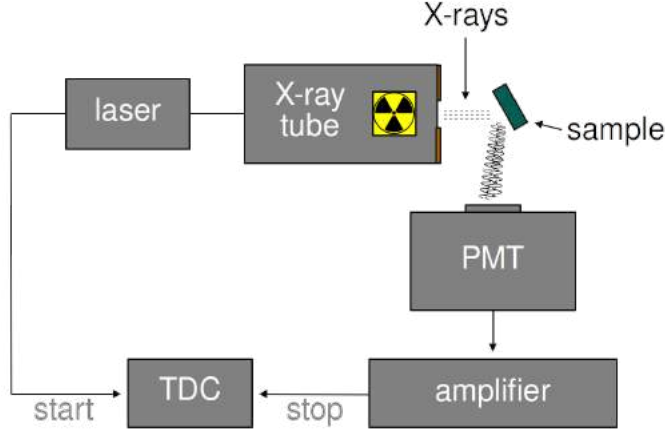

Figure 5.15: Overall impulse response function of the measurement system with X-rays. The intensity is shown as function of time. The IRF constitutes the experimental limit of the measurement and its FWHM is about 160 ps.

Rise and decay times were obtained from the fit of the scintillation distribution [52] with the convolution of the IRF (Equation 5.9) with the intrinsic scintillation rate (Equation 5.10):

$$g(t) = \frac{1}{\sigma_{\mathrm{IRF}}\sqrt{2\pi}} \, \exp\left(-\frac{(t-\mu)^2}{2\sigma_{\mathrm{IRF}}^2}\right).$$
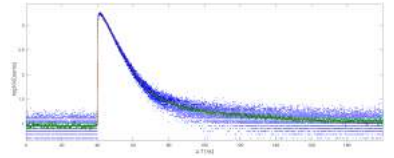
(5.9)

Figure 5.17: Example of a scintillation distribution, fitted with Equation 5.11 to obtain rise and decay times of a scintillator, given on a logarithmic scale. The blue dots are the measured data, the green line is their average, and the red curve is their fit.

$$h(t \mid \theta) = \Theta(t-\theta) \sum_{i=1}^{N} \frac{\exp\left(-\frac{t-\theta}{\tau_{\mathrm{d},i}}\right) - \exp\left(-\frac{t-\theta}{\tau_{\mathrm{r},i}}\right)}{\tau_{\mathrm{d},i} - \tau_{\mathrm{r},i}} \cdot R_i,$$

(5.10)

where t is the time, θ the time of onset of scintillation, μ the mean, σ the standard deviation, and Θ the Heavyside step function. The parameters $\tau_{\mathrm{r},i}$ and $\tau_{\mathrm{d},i}$ denote the rise and the decay times of the photon distribution, respectively, and R_i being the abundance of the i-th decay time.

Heavyside step function:
$$\Theta(t-\theta) = \begin{cases} 1, & t-\theta \geq 0 \\ 0, & t-\theta < 0 \end{cases}$$

The fit function thus results in

Convolution:
$$f_{\mathrm{conv}}(t) = g(t) * h(t)$$
$$= \int_{-\infty}^{+\infty} g(t-t')\, h(t')\, = \int_{-\infty}^{+\infty} g(t)\, h(t-t')$$

$$f_{\mathrm{conv}}(t \mid \theta) = g(t) * h(t)$$

$$= \sum_{i=1}^{N} \frac{R_i}{2(\tau_{\mathrm{d},i} - \tau_{\mathrm{r},i})} \, \exp\left(\frac{2\tau_{\mathrm{d},i}(\theta - t) + \sigma_{\mathrm{IRF}}^2}{\tau_{\mathrm{d},i}^2}\right)$$

$$\cdot \left[1 - \mathrm{erf}\left(\frac{\tau_{\mathrm{d},i}(\theta - t) + \sigma_{\mathrm{IRF}}^2}{\sqrt{2}\sigma_{\mathrm{IRF}}\tau_{\mathrm{d},i}}\right)\right]$$

(5.11)

$$- \sum_{i=1}^{N} \frac{R_i}{2(\tau_{\mathrm{d},i} - \tau_{\mathrm{r},i})} \, \exp\left(\frac{2\tau_{\mathrm{r},i}(\theta - t) + \sigma_{\mathrm{IRF}}^2}{\tau_{\mathrm{r},i}^2}\right)$$

$$\cdot \left[1 - \mathrm{erf}\left(\frac{\tau_{\mathrm{r},i}(\theta - t) + \sigma_{\mathrm{IRF}}^2}{\sqrt{2}\sigma_{\mathrm{IRF}}\tau_{\mathrm{r},i}}\right)\right].$$

The effective decay time $\tau_{d,eff}$, as already mentioned in Equation 3.10, is then expressed by

$$\frac{1}{\tau_{d,eff}} = \sum_{i=1}^{N} \frac{R_i}{\tau_{d,i}} \qquad \text{with} \qquad \sum_{i=1}^{N} R_i = 1 \,. \tag{5.12}$$

An example of a scintillation distribution is shown in Figure 5.18, zoomed in to better clarify the rise part.

Figure 5.18: Zoom of a scintillation distribution, fitted with Equation 5.11, shown on a linear scale. The blue dots are the measured data, the green line is their average, the red curve is their fit, and the dotted grey curve the IRF of the measurement system.
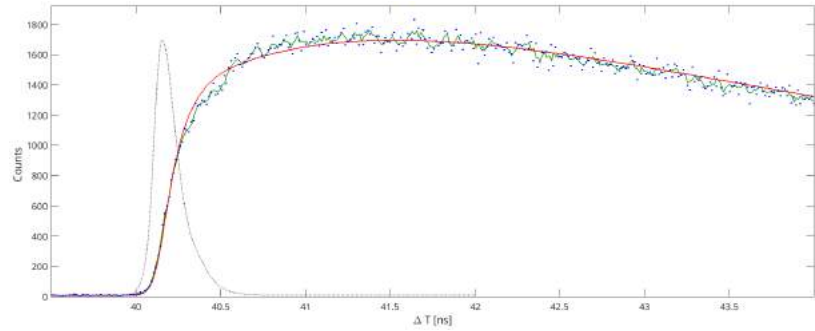
The model to fit the scintillation distribution described above is well-established for conventional scintillators and also works well for several nanomaterials. However, it is not ideal for all of them as some show very fast timing. Therefore another model was used to describe the scintillation profile of these very fast nanomaterials [28], based on a study by Gundacker et al. [51] in which Cherenkov emission was fitted on top of the scintillation distribution. It consists of adding a Dirac delta distribution to the exponential part to properly account for the (semi-)prompt Cherenkov emission. As example a scintillation distribution with prompt emission is shown in Figure 5.19, zoomed in to better clarify the rise part. The rise part is clearly inside the IRF of the system.

Figure 5.19: Zoom of a scintillation distribution with prompt emission, fitted with Equation 5.14, shown on a linear scale. The blue dots are the measured data, the green line is their average, the red curve is their fit, and the dotted grey curve the IRF of the measurement system.
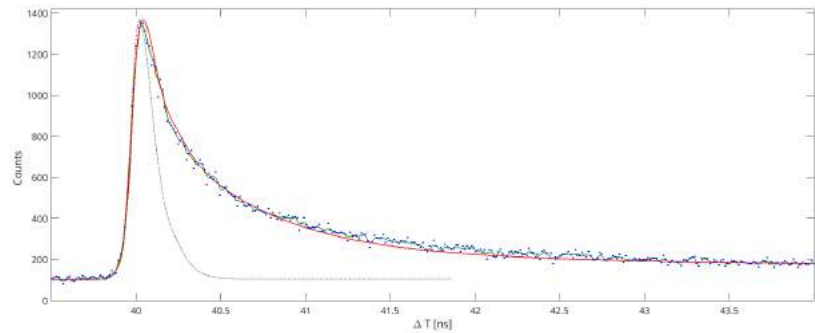
In this case the scintillation distribution was fitted by convoluting the IRF (Equation 5.9) with the sum of the intrinsic scintillation rate (Equation 5.10) and a Dirac delta function:

Dirac delta function:

$$\delta(t) = \begin{cases} \infty, & t = 0 \\ 0, & t \neq 0 \end{cases}$$

$$h_p(t \mid \theta) = h(t \mid \theta) + R_p \cdot \delta(t) \,. \tag{5.13}$$

The fit function thus results in

$$f_{\text{conv}}(t \mid \theta) = g(t) * h_{\text{p}}(t \mid \theta)$$

$$= \sum_{i=1}^{N} \frac{R_i}{2(\tau_{\text{d,i}} - \tau_{\text{r,i}})} \exp\left(\frac{2\tau_{\text{d,i}}(\theta - t) + \sigma_{\text{IRF}}^2}{\tau_{\text{d,i}}^2}\right)$$

$$\cdot \left[1 - \text{erf}\left(\frac{\tau_{\text{d,i}}(\theta - t) + \sigma_{\text{IRF}}^2}{\sqrt{2}\sigma_{\text{IRF}}\tau_{\text{d,i}}}\right)\right]$$

$$- \sum_{i=1}^{N} \frac{R_i}{2(\tau_{\text{d,i}} - \tau_{\text{r,i}})} \exp\left(\frac{2\tau_{\text{r,i}}(\theta - t) + \sigma_{\text{IRF}}^2}{\tau_{\text{r,i}}^2}\right) \qquad (5.14)$$

$$\cdot \left[1 - \text{erf}\left(\frac{\tau_{\text{r,i}}(\theta - t) + \sigma_{\text{IRF}}^2}{\sqrt{2}\sigma_{\text{IRF}}\tau_{\text{r,i}}}\right)\right]$$

$$+ \frac{R_{\text{p}}}{\sqrt{2\pi}\sigma_{\text{IRF}}} \exp\left(-\frac{(t - \theta)^2}{2\sigma_{\text{IRF}}^2}\right).$$

The effective decay time $\tau_{\text{d,eff}}$ is then expressed by

$$\tau_{\text{d,eff}} = \left(\sum_{i=1}^{N} \frac{R_i'}{\tau_{\text{d,i}}}\right)^{-1}, \qquad (5.15)$$

$$\text{with} \qquad R_{\text{p}} + \sum_{i=1}^{N} R_i = 1 \qquad \text{and} \qquad R_i' = \frac{R_i}{\sum_{i=1}^{N} R_i},$$

where R_i and R_i' are the abundances and the reduced abundances of the i-th decay time, respectively, and R_{p} the prompt photon emission/abundance of the Dirac delta distribution.

All scintillators studied in this work showed at least two decay times. For comparison, the effective decay time without the presence of prompt emission was previously calculated using Equation 5.12, where the term of the prompt emission is not existent. On the other hand if prompt emission is present the effective decay time was calculated needs to be calculated using Equation 5.15. Most scintillators showed rise times below the resolution of the IRF of the system (160 ps FWHM) and therefore could not be resolved. Thus they were set to zero. This had no effect on the fit.

5.7 Detector Time Resolution with X-rays

The experimental setup to obtain the detector time resolution (DTR) under pulsed X-ray excitation is shown in Figure 5.16 and Figure 5.21 [41]. Similar to the TCSPC setup, the laser was used as the time reference and excitation source for the X-ray tube. The readout of the light that was produced by the scintillator, on the other hand, was made by a $3 \times 3 \, \text{mm}^2$ Hamamatsu HPK S13360-3050CS SiPM, which was rated at a breakdown

voltage of $V_{BD} = 51\,V$ and operated at $V_{BIAS} = 61\,V$. The scintillator, cut to SiPM size, was coupled to the SiPM using Meltmout as optical coupling glue, having a refractive index of $n = 1.586$. The output of the SiPM was fed into the readout electronics, which are described in Section 5.1. The output signals were then digitized by a LeCroy WaveRunner 8104 oscilloscope, running at 20 GS/s with a bandwidth of 1 GHz. In combination with the start signal coming from external trigger of the laser the time delay spectrum was taken by the oscilloscope.
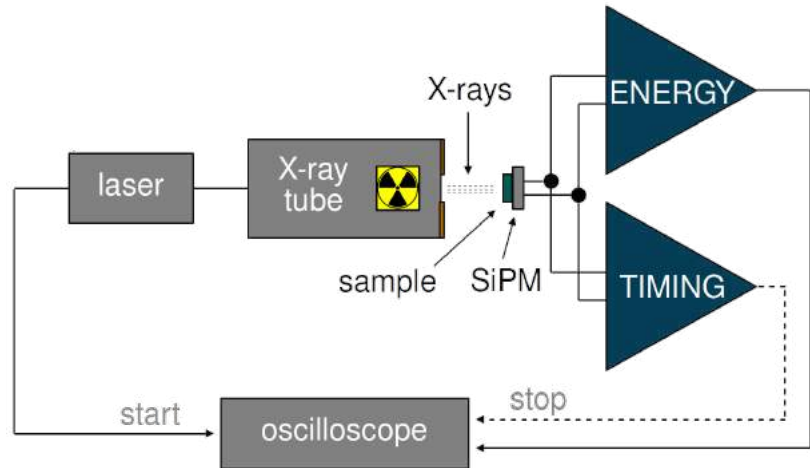

Figure 5.20: Schematic of the experimental setup for the characterization with pulsed X-rays to measure the DTR or single time resolution. The laser signal served as the start signal, the SiPM timing signal as the stop signal.
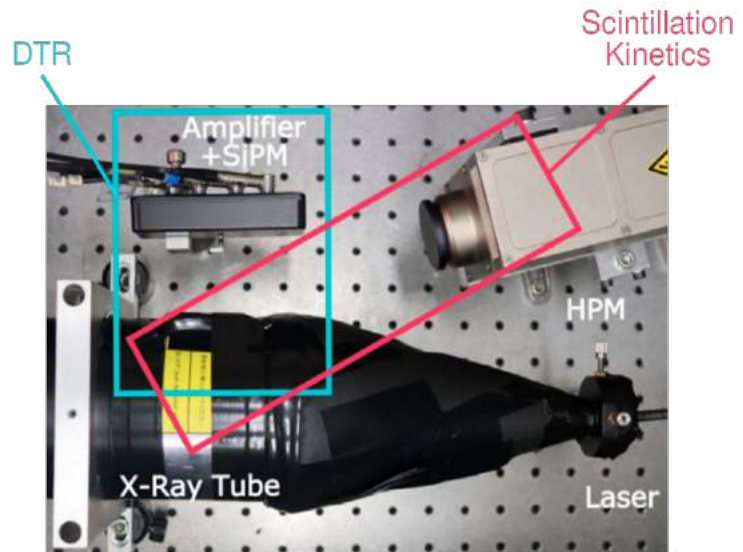

Figure 5.21: Photograph of the two co-existing setups for the characterization measurments with X-rays. Figure adapted from Pagano, Frank et al. [41].

The time delay Δt was calculated, event by event, as the time difference between the laser signal t_{Laser} and the SiPM timing signal t_{SiPM}, as already described in Section 5.1:

$$\Delta t = t_{SiPM}(V_{th(SiPM)}) - t_{Laser}(V_{th(Laser)}), \qquad (5.16)$$

$$\text{with} \qquad t_{Laser}(V_{th(Laser)}) < t_{SiPM}(V_{th(SiPM)}).$$

The time delay distribution was then fitted with a function obtained from the convolution of a Gaussian (Equation 5.17) with an exponential (Equation 5.18) probability distribution to account for the asymmetry of the distribution:

$$g(t) = \frac{1}{\sigma\sqrt{2\pi}} \exp\left(-\frac{(t-\mu)^2}{2\sigma^2}\right), \tag{5.17}$$

$$h(t) = \lambda \exp\left(-\lambda t\right). \tag{5.18}$$

The fit function thus results in

$$
\begin{aligned}
f_{\text{conv}}(t) &= g(t) * h(t) \\
&= \frac{\lambda}{2} \exp\left(\frac{\lambda}{2}\left(2\mu + \lambda\sigma^2 - 2t\right)\right) \operatorname{erfc}\left(\frac{\mu + \lambda\sigma^2 - t}{\sqrt{2}\sigma}\right) \\
&= \frac{\lambda}{2} \exp\left(\frac{\lambda}{2}\left(2\mu + \lambda\sigma^2 - 2t\right)\right) \left[1 - \operatorname{erf}\left(\frac{\mu + \lambda\sigma^2 - t}{\sqrt{2}\sigma}\right)\right],
\end{aligned}
\tag{5.19}
$$

where t is the time, μ the mean of the Gaussian distribution, σ the standard deviation, σ^2 the variance, λ the exponential parameter expressing the tail in the distribution, and erf the error function, given by

$$\operatorname{erf}(t) = \frac{2}{\sqrt{\pi}} \int_0^t e^{-x^2}\, dx. \tag{5.20}$$

The DTR was extracted as the FWHM of this fit, as shown in Figure 5.22.

Time Walk Correction

The leading edge technique is intrinsically affected by time walk, as already described in Section 5.1. Therefore, an event by event time correction was made based on the rise time of each SiPM timing signal to account for this effect. The rise time of the SiPM timing signal was extracted using Equation 5.1 in Section 5.1. Then the rise time distribution of all events was plotted and split into n intervals, each with equally large integrated areas, as shown in Figure 5.23.

For each interval, the time delay distribution was plotted and fitted with Equation 5.19. Figure 5.24 shows some fitted time delay distributions as an example. To make the difference clear, intervals with small and large rise times are shown here. In line with the above, events with larger rise times show wider distributions, and vice versa, events with smaller rise times have narrower distributions.

Convolution:
$$f_{\text{conv}}(t) = g(t) * h(t)$$
$$= \int_{-\infty}^{+\infty} g(t - t')\, h(t') = \int_{-\infty}^{+\infty} g(t)\, h(t - t')$$

Complementary error function:
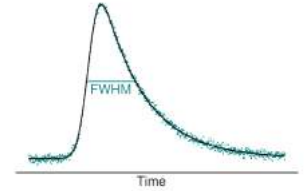$$\operatorname{erfc}(t) = 1 - \operatorname{erf}(t)$$

Figure 5.22: The detector time resolution (DTR) or single time resolution was extracted as the FWHM of fit of the time delay distribution, fitted with Equation 5.19.

Figure 5.23: The time walk correction was done based on the rise time since it is proportional to the amplitude of the signal. Therefore the rise time distribution of all events was split into n intervals, each with equally large integrated areas.
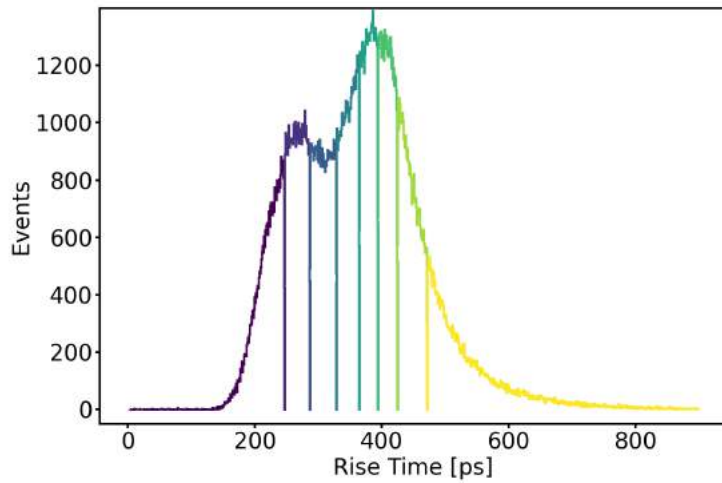
Following this, the position of the mean μ of the fit was obtained for each interval by

$$t(\mu) = t_{\text{corr}} \, , \tag{5.21}$$

and each time delay was corrected by

$$\Delta t_{\text{corr}} = \Delta t - t_{\text{corr}} \, , \tag{5.22}$$

where Δt and Δt_{corr} are the time delays, before and after the time walk correction, respectively, and t_{corr} the correction constant in each interval.

Figure 5.24: The time delays distribution of each interval were fitted with Equation 5.19. Events with larger rise times have wider time delay distributions, events with smaller rise times have narrower distributions. The position of the mean of the fit is the correction constant.
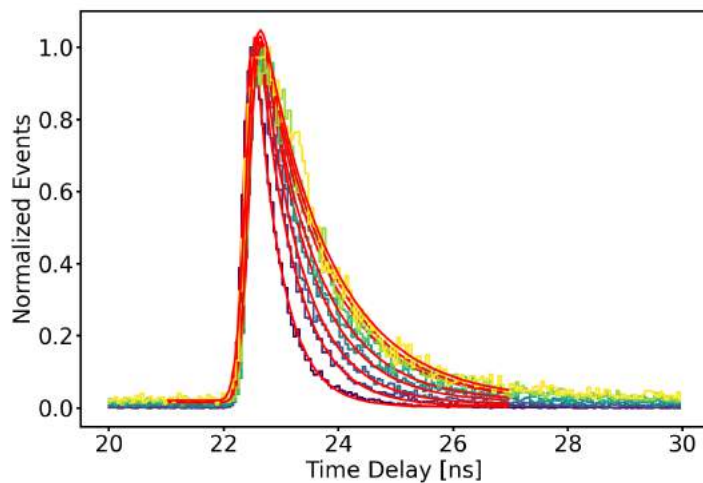
After correcting the timewalk, the time delay distribution of all events was plotted and fitted with Equation 5.19. The detector time resolution (DTR) was then evaluated as the FWHM of this fit, as shown in Figure 5.25.
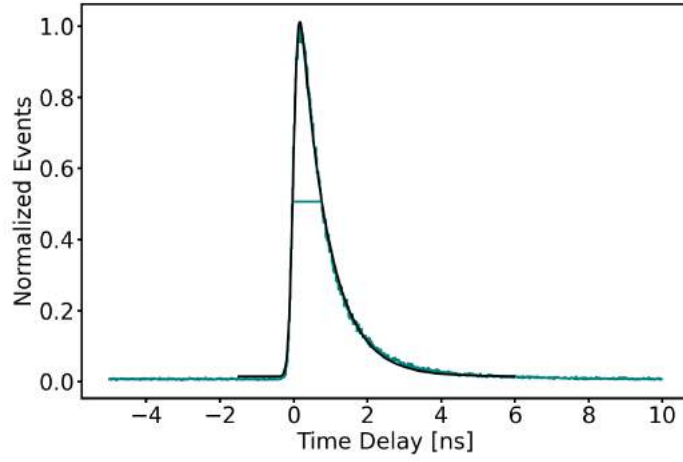
Figure 5.25: Time delay distribution with fit (Equation 5.19) to obtain the DTR as FWHM of this fit.

Finally, the measured FWHM was corrected for the IRF of the X-ray tube ($FWHM_{\text{X-rays}}$), the pulse width of the laser ($FWHM_{\text{laser}}$) and the jitter[3] of the laser trigger ($FWHM_{\text{trigger}}$). Assuming that everything is Gaussian, the DTR or single time resolution was then extracted as

3: The jitter is the timing uncertainty of pick-off signal influenced by noise in the system and by statistical fluctuations of the signals from the detector.

$$DTR = \sqrt{FWHM^2_{\text{meas}} - FWHM^2_{\text{X-rays}} - FWHM^2_{\text{laser}} - FWHM^2_{\text{trigger}}}\,,$$
(5.23)

where the contributions are given by

$$FWHM_{\text{X-rays}} = 60\,\text{ps}\,, \qquad FWHM_{\text{laser}} = 50\,\text{ps}\,, \qquad \text{and} \qquad FWHM_{\text{trigger}} = 40\,\text{ps}\,,$$

where $FWHM_{\text{meas}}$ is the FWHM obtained from the fit.

Characterization Results | 6

In this chapter the characterization results of the studied nanoscintillators, introduced in Section 4.4, are presented. The measurement setups and analysis techniques were already described in Chapter 5. The chapter is structured in the order of the individual nanoscintillators that were investigated and concludes with a summary and comparison of all results. Measurements with high energy particles in the context of calorimetry are discussed in Chapter 7.

6.1 CsPbBr$_3$ Perovskite Nanoscintillators

A set of nanocomposites of CsPbBr$_3$ nanocrystals embedded in poly-methylmethacrylate (PMMA) and polylaurylmeth-acrylate (PLA) were supplied by UNIMIB. The nanocomposites were produced by direct polymerization, as described in Section 4.4, resulting in very low filling factors, below 1%. Higher concentrations could not be achieved, for polymerization can no longer take place due to the absorption of UV light by the nanocrystals and their high self-absorption, as described in Section 4.3. As example a photograph of the CsPbBr$_3$ nanocomposite with 0.05 % filling factor is shown in Figure 6.1.

Figure 6.1: Photograph in ambient light of the CsPbBr$_3$ nanocomposite with 0.05 % filling factor.

The characterization and investigation of these perovskite nanoscintillators led to a joint publication with UNIMIB: "Ultrafast and Radiation-Hard Lead Halide Perovskite Nanocomposite Scintillators" in ACS Energy Letters [27].

Optical Properties

The radioluminescence (RL) spectra of CsPbBr$_3$ nanocrystals in PMMA/PLA are shown in Figure 6.2. As the figure shows all scintillators show a single peak with a maximum at ~ 2.4 eV, which corresponds to a wavelength of ~ 520 nm. A slight red shift with increasing filling factor can also be observed.

Figure 6.3 shows the transmission spectra of the set of CsPbBr$_3$ in PMMA/PLA with different filling factors. Below 500 nm the transmittance increases with increasing filling factor and ranges from almost 0 up to ~ 70 %, although all scintillators are nearly completely transparent for wavelengths above 500 nm. In summary, the low filling factor of less than 1 % leads to weak self-absorption, low density, and thus low stopping power, resulting in relatively high transparency. The decrease in transmittance with increasing filling factor can already seen by eye in the photographs inserted in Figure 6.2.

Figure 6.2: Radioluminescence spectra of CsPbBr$_3$ in PMMA/PLA with different fillings factors. The spectra have been shifted vertically for better clarity. Photographs of the corresponding nanocomposites are shown at each spectrum, on the left in ambient light and on the right under UV light. Figure from Erroi, Frank et al. [27].
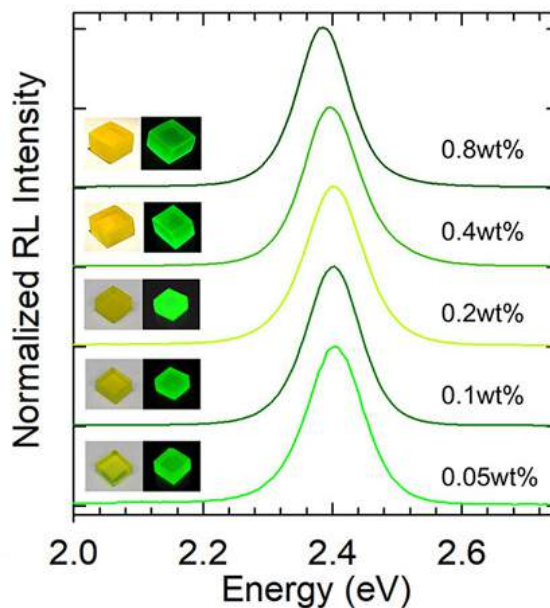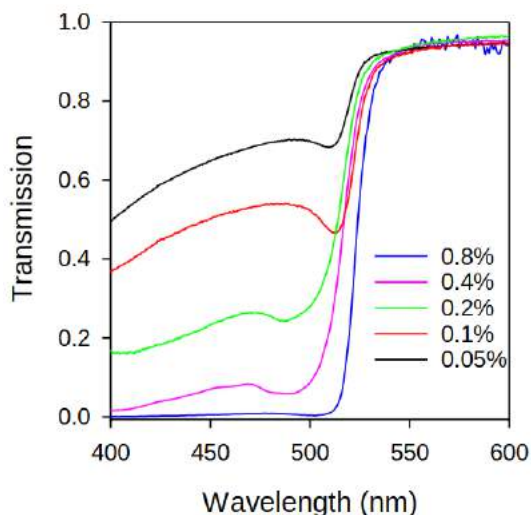

Figure 6.3: Transmission spectra of CsPbBr$_3$ nanocrystals in PMMA/PLA with different filling factors. Figure from Erroi, Frank et al. [27].

Scintillation Kinetics

The scintillation distributions for CsPbBr$_3$ nanocrystals in PMMA/PLA are shown in Figure 6.4. They were fitted with Equation 5.14, describing the ultra-fast emission, resulting in two decay times and a prompt component. For each filling factor the effective decay time was calculated using Equation 5.15. The results are summarized in Table 6.1. As the results show, the prompt component R_p (below 160 ps, but limited to the resolution of the IRF) contributes between 29 and 34 % to the scintillation distribution, and the first decay time τ_{d1} (between 580 and 620 ps) between 7 and 37 %. Both together result in 37 to 67 % of the photons emitted already within the first nanosecond. The second decay time τ_{d2} is no longer in the sub-nanosecond range, but still below 25 ns for all scintillators. The effective decay time increases with increasing filling factor, ranging from 1.1 to 4.1 ns. Therewith all nanocomposites show ultra-fast timing.
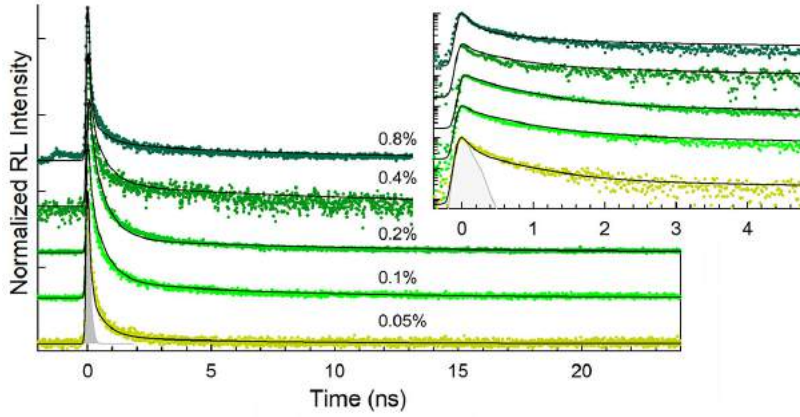
Figure 6.4: Scintillation distribution of CsPbBr$_3$ nanocrystals in PMMA/PLA with different filling factors. The scintillation decay is shown on a semi-logarithmic scale. The dotted gray line represents the IRF of the system.
Inset: Details of the ultra-fast component on a linear scale across a smaller range that is between 0 and 4 ns.
The spectra are shifted vertically for higher clarity. Figure adapted from Erroi, Frank et al. [27].

c_{NC}	R_p	τ_{d1}	R_1	τ_{d2}	R_2	$\tau_{d,eff}$
[wt %]	[%]	[ns]	[%]	[ns]	[%]	[ns]
0.05	30 ± 2	0.61 ± 0.04	37 ± 2	22.0 ± 1.1	33 ± 2	1.1 ± 0.1
0.1	32 ± 2	0.62 ± 0.04	21 ± 2	8.7 ± 0.5	47 ± 3	1.8 ± 0.1
0.2	34 ± 2	0.60 ± 0.03	22 ± 2	6.8 ± 0.5	44 ± 3	1.5 ± 0.1
0.4	29 ± 2	0.58 ± 0.03	9 ± 1	10.3 ± 0.6	62 ± 4	3.3 ± 0.2
0.8	30 ± 2	0.62 ± 0.04	7 ± 1	10.5 ± 0.6	63 ± 4	4.1 ± 0.3

Table 6.1: Results of the scintillation kinetics with X-rays of CsPbBr$_3$ nanocrystals in PMMA/PLA as a function of filling factor. The scintillation distributions were fitted with Equation 5.14, resulting in two decay times and a prompt component. c_{NC} denotes the filling factor, $\tau_{d,i}$ are the decay times and R_i their corresponding abundances, respectively. R_p is the abundance of the prompt emission, and $\tau_{d,eff}$ the effective decay time, determined with Equation 5.15. Results published in Erroi, Frank et al. [27].

Conclusion

A filling factor below 1% of CsPbBr$_3$ nanocrystals embedded in PMMA/PLA was limited by the polymerization technique owing to high self-absorption of the nanocrystals. However, it enabled large-scale production in various forms and shapes. Tiles with a size of several hundred square centimeters and thicknesses of a few millimeters have easily produced at low cost, as shown in Figure 4.9. All scintillators showed very high transmission, low self-absorption, but also very low stopping power, which is primarily due to this very low filling factor. All scintillators showed ultra-fast timing where all decay times ranged below 25 ns, with effective decay times below 5 ns and with 7 and 67 % of the photons already emitted within the first nanosecond. It has been demonstrated that even at very low filling factor, a large number of prompt photons are generated. This makes them promising candidates for fast timing applications. Nevertheless, all scintillators exhibited very low stopping power, already for low energy particles such as X-rays. However, stopping power is a prerequisite in calorimetry.

6.2 Thin CsPbBr$_3$ Perovskite Nanoscintillator Platelets

Two sets of nanocomposites of CsPbBr$_3$ perovskite nanocrystals embedded in polystyrene (PS) were supplied by CTU. Similar in composition, the nanocrystals were synthesized with two different surface ligands, a first set with oleic acid and oleylamine (OA + OLAM) and a second set

with didodecyldimethylammonium bromid (DDAB). The nanocomposites were produced by solvent evaporation, as described in Section 4.4, resulting this time in higher filling factors of 1, 5, and 10 % compared to direct polymerization, as described in Section 4.3, but with a thickness of only ~100 μm.

The characterization and investigation of these perovskite nanocomposites and the effects of using different surface ligands led to a joint publication with CTU: "Timing performance of lead halide perovskite nanocrystals embedded in a polystyrene matrix" in the Journal of Materials Chemistry C [28].

Optical Properties

As already mentioned in Section 4.3, ligands are used to passivate the surface of nanocrystals to improve their optoelectronic properties and prevent aggregation. Compared to OA + OLAM, DDAB is supposed to provide superior surface passivation of the nanocrystals, which effectively leads to higher quantum yields [23]. The photoluminescence (PL) and radioluminescence (RL) spectra of the CsPbBr$_3$ nanocrystals with both surface ligands are shown in Figure 6.5. Compared to the nanocrystals with OA + OLAM, nanocrystals with DDAB indeed showed higher intensities in both spectra, consistent with the above mentioned expectation.
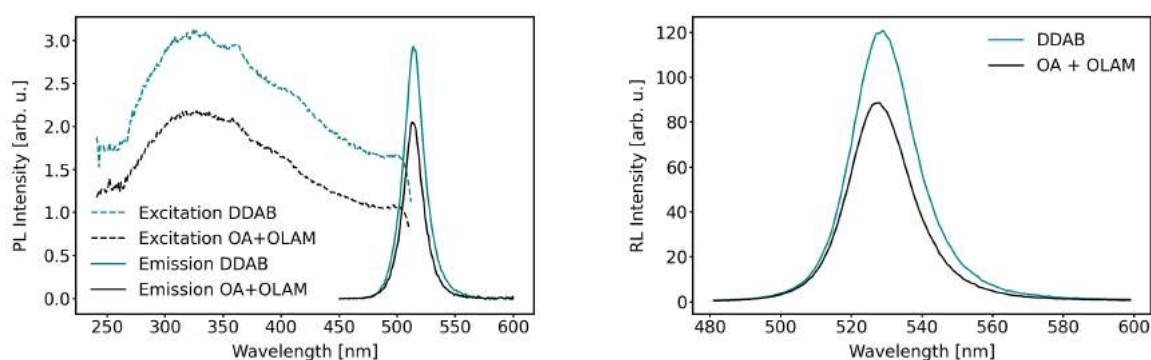

Figure 6.5: PL emission (solid lines) and excitation (dashed lines) spectra on the left, and RL spectra on the right of CsPbBr$_3$ nanocrystals with OA + OLAM and DDAB surface ligands. Figure adapted from Děcká, Frank et al. [28].

The RL spectra, after embedding the nanocrystals in PS, are shown in Figure 6.6. For both surface ligands the PL and RL spectra show only a slight increase in redshift with increasing filling factor.

Figure 6.7 shows the transmission spectra of the two sets as well as photographs of the nanocomposites. Already by eye, as the photographs show, a decrease in transparency of the nanocomposites with increasing filling factor is already observable, which was then confirmed by the transmission measurements. Overall, the scintillators with DDAB show higher transmittance for each filling factor than those with OA + OLAM. At low filling factor of 1%, the transmittance above 500 nm is only slightly higher, while at higher filling factors the transmittance visibly grows especially for nanocomposites synthesized with DDAB. On the other hand and only at the same low filling factor, the scintillators
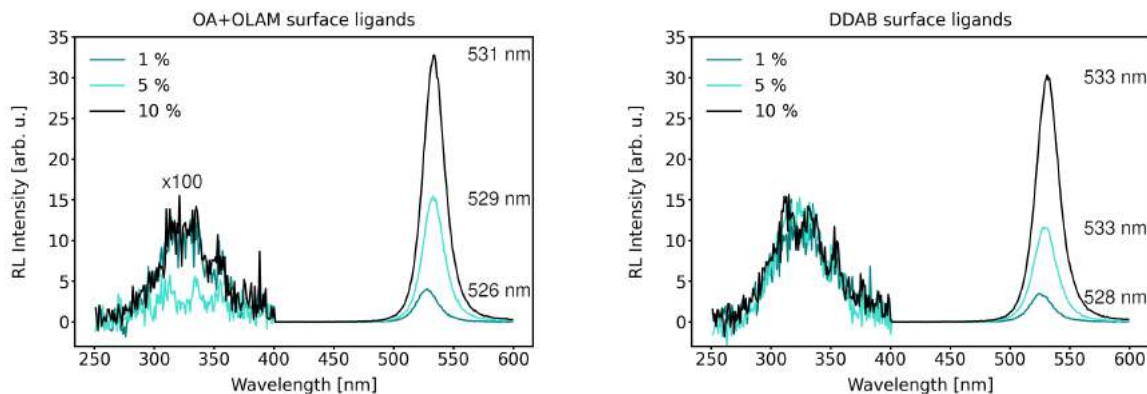
Figure 6.6: RL spectra of CsPbBr$_3$ nanocrystals in PS with different filling factors and two different surface ligands, on the left, OA + OLAM, and on the right, DDAB. The wavelength of the maximum emission is highlighted in each plot. To illustrate the weak emission contributed by PS the spectra were multiplied by a factor of 100 in the range from 250 to 400 nm. Figure adapted from Děcká, Frank et al. [28].

show satisfactory transparency in the range between 300 and 500 nm, where the scintillators synthesised with DDAB exhibit approximately two times the transmittance compared to OA + OLAM. However, at higher filling factors, both sets became essentially opaque. The low transmittance below 500 nm is due to self-absorption of the nanocrystals, visible in the PL excitation spectra on the left in Figure 6.5, while above 500 nm the transmission is mainly dominated by scattering. Higher filling factors bear the danger of leading to clustering and/or aggregation of the nanocrystals. In this context, clustering refers to the non-uniform distribution of nanocrystals within the nanocomposite, forming clusters while maintaining their shape and size. On the other hand, aggregation implies that the nanocrystals interact with their neighbors, leading to a formation of larger particles. Furthermore, from the comparison of the two sets with different surface ligands, it can be deduced that DDAB at least partially prevents clustering and/or aggregation of the nanocrystals.
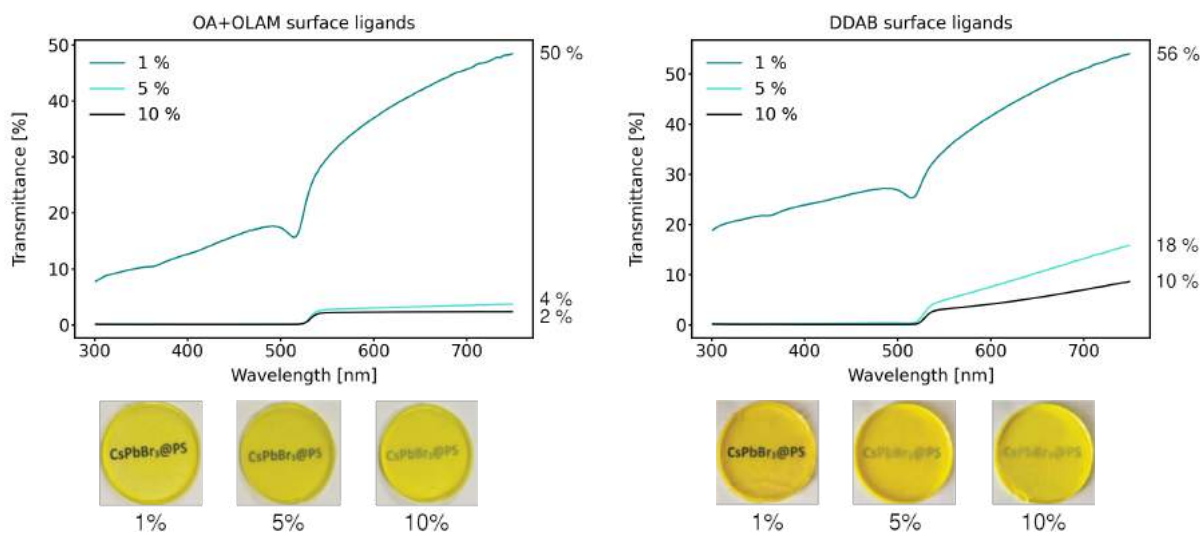

Figure 6.7: Transmission spectra of CsPbBr$_3$ nanocrystals in PS with different surface ligands, OA + OLAM (left) and DDAB (right), and different filling factors. The maximum transmittance is highlighted on the right of each plot. Photographs of the nanocomposites with their corresponding filling factor are shown below. Figure adapted from Děcká, Frank et al. [28].

Scintillation Kinetics

The scintillation distribution of $CsPbBr_3$ nanocrystals with DDAD surface ligands and 10 % filling factor embedded in PS is shown in Figure 6.8 as example of the set of $CsPbBr_3$ nanomcomposites. All scintillation distributions of the set were fitted with Equation 5.14, resulting in three decay times and a prompt component. For each filling factor the effective decay time was calculated using Equation 5.15. The results are summarized in Table 6.2.

As the results, show the prompt component R_p (below 160 ps, but limited to the resolution of the IRF) contributes with an abundance of 16 to 24 % to the scintillation distribution, and results in a first decay time τ_{d1} (between 700 and 900 ps) with a contribution of 17 to 24 %. Both together result in 33 to 42 % of the photons emitted already within the first nanosecond. The other decay times, τ_{d2} and τ_{d3}, are no longer in the sub-nanosecond range, but still below 40 ns. As the table shows, within both sets, and as a function of the filling factor, no trend becomes visible.

Table 6.2: Results of the scintillation kinetics with X-rays of $CsPbBr_3$ nanocrystals in PS with two different surface ligands, OA + OLAM and DDAB, and different filling factors. The scintillation distributions were fitted with Equation 5.14, resulting in three decay times and a prompt component. c_{NC} denotes the filling factor, $\tau_{d,i}$ are the decay times and R_i their corresponding abundances, respectively. R_p is the abundance of the prompt emission, and $\tau_{d,eff}$ the effective decay time, determined with Equation 5.15. Results published in Děcká, Frank et al. [28].

Ligand	c_{NC} [wt %]	R_p [%]	τ_{d1} [ns]	R_1 [%]	τ_{d2} [ns]	R_2 [%]	τ_{d3} [ns]	R_3 [%]	$\tau_{d,eff}$ [ns]
OA + OLAM	1	18 ± 2	0.76 ± 0.02	24 ± 4	3.0 ± 0.3	27 ± 3	11 ± 1	31 ± 7	1.9 ± 0.2
	5	24 ± 3	0.68 ± 0.02	18 ± 3	3.4 ± 0.3	30 ± 4	18 ± 2	28 ± 5	2.0 ± 0.2
	10	16 ± 2	0.69 ± 0.02	14 ± 2	4.1 ± 0.4	28 ± 4	26 ± 3	42 ± 7	2.9 ± 0.3
DDAB	1	16 ± 2	0.92 ± 0.03	18 ± 3	3.9 ± 0.4	29 ± 4	21 ± 3	37 ± 7	2.9 ± 0.3
	5	20 ± 2	0.79 ± 0.02	17 ± 3	3.5 ± 0.3	35 ± 4	18 ± 2	28 ± 5	2.4 ± 0.2
	10	20 ± 2	0.79 ± 0.02	17 ± 3	3.9 ± 0.4	27 ± 3	15 ± 2	36 ± 6	2.6 ± 0.2

Figure 6.8: Scintillation distributions of $CsPbBr_3$ nanocrystals in PS with 10 % filling factor and DDAB surface ligands. The scintillation decay is shown on a semi-logarithmic scale. The blue dots are the measured data, the green line is their average, and the red curve is the fit. Inset: Zoom of the scintillation distribution to illustrate the ultra-fast component on a linear scale. The dotted gray line represents the IRF of the system. Figure adapted from Děcká, Frank et al. [28].
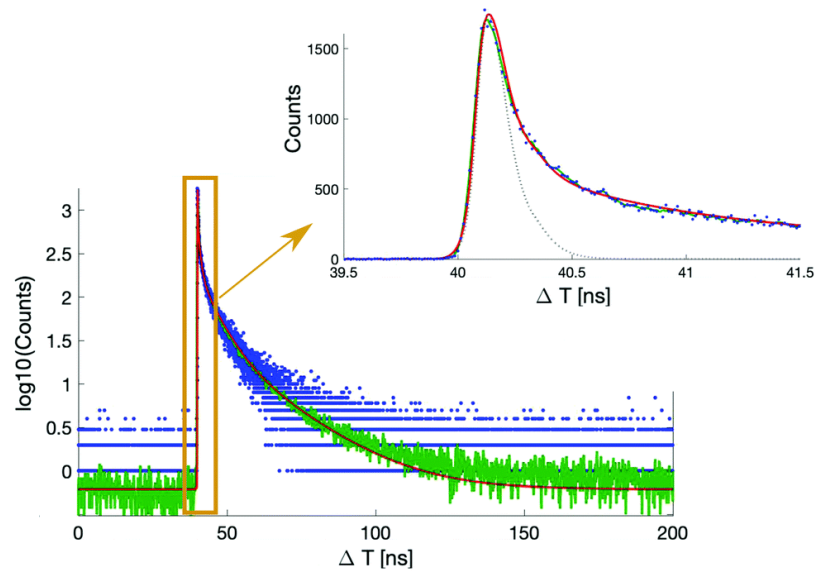
Detector Time Resolution

The time delay distributions of CsPbBr$_3$ nanocrystals in PS were fitted with Equation 5.19, as discribed in Section 5.7. The time resolutions were extracted as the FWHM of the corresponding fits. The results of the detector time resolution are summarized in Table 6.3. As an example, Figure 6.9 shows the time delay distribution of the nanocomposite with 10 % filling factor and synthesized with DDAB compared to the time delay distributions of two conventional scintillators. All scintillators showed a time resolution of ~ 300 ps with no observable difference accountable to the filling factor for both sets of surface ligands.
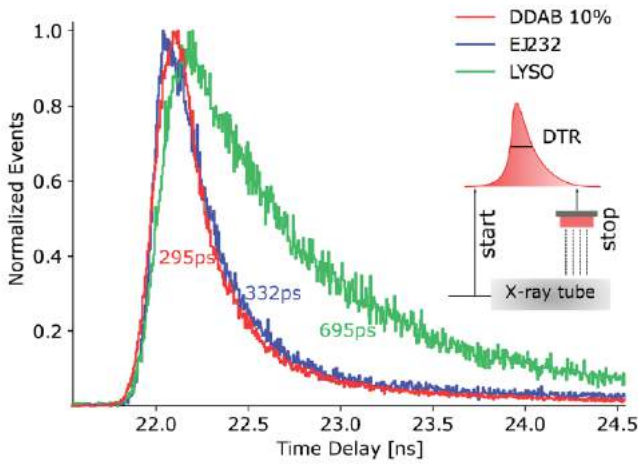
Figure 6.9: Time delay distributions of CsPbBr$_3$ nanocrystals in PS with 10 % filling factor and DDAB surface ligands in comparison to two conventional scintillators, EJ232 and LYSO. The DTR is highlighted in the plot. Figure adapted from Děcká, Frank et al. [28].

c_{NC}	Dimension	DTR	
[wt %]	[mm^3]	[ps]	
		OA + OLAM	DDAB
1	3 × 3 × 0.1	305 ± 9	308 ± 9
5	3 × 3 × 0.1	330 ± 10	309 ± 9
10	3 × 3 × 0.1	319 ± 9	295 ± 8

Table 6.3: Results of the detector time resolution (DTR) with X-rays of CsPbBr$_3$ nanocrystals in PS with two different surface ligands, OA + OLAM and DDAB, and different filling factors. c_{NC} denotes the fillings factor. The samples were coupled with Meltmount to the SiPM. The values are corrected for time walk and given in FWHM. Results published in Děcká, Frank et al. [28].

Conclusion

The polymerization technique allowed higher filling factors of up to 10 % for the production of nanocomposites of CsPbBr$_3$ perovskite nanocrystals embedded in PS. However, this technology was limited to low-scale production, allowing only the formation of thin platelets. Considering all results, an insight into the light emission of these CsPbBr$_3$ perovskite nanocomposites with increasing filling factor could be obtained. The optical measurements show higher photoluminescence and radioluminescence, but also significantly lower transmittance with increasing filling factors.

From the comparison of the two sets with different surface ligands, OA + OLAM and DDAB, it can be concluded that DDAB at least partially prevented clustering and/or aggregation of the nanocrystals. However,

the results of the two sets differed only slightly. All scintillators showed ultra-fast timing, where all decay times were below 40 ns, and effective decay times below 3 ns and 33 and 42 % of photons emitted already within the first nanosecond. Nevertheless, all scintillators exhibited very poor transparency because of high self-absorption. In terms of high energy calorimetry these scintillators do not provide sufficient stopping power because of their limited thickness and poor light transport, also suffering from poor transparency and high self-absorption. This limits the choice of these scintillators for calorimetry in high energy physics.

6.3 CdZnS/ZnS Nanoscintillators

A set of nanocomposites of cadmium doped zinc sulfide (CdZnS) and zinc sulfide (ZnS) nanocrystals with a core/shell structure embedded in polyvinyltoluene (PVT) with the addition of a fluorescent dye of 4,7-bis2'-9',9'-bis[(2"'-ethylhexyl)fluorenyl]-2,1,3-benzothiadiazole (FBTF) were supplied by UCLA. The nanocomposites were produced by direct polymerization, as described in Section 4.4. Compared to the previous nanocomposites, significantly higher filling factors of 40, 50, and 56 % were achieved. Their photographs are shown in Figure 6.10. The scintillator were of different thickness, ranging from 2.0 to 3.5 mm.
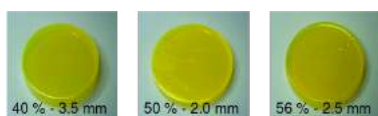
Optical Properties

The photoluminescence (PL) spectra of CdZnS/ZnS quantum dots (QDs) with core/shell structure and the dye FBTF are shown on the left in Figure 6.11. As the figure shows, the narrow emission of CdZnS/ZnS QDs (blue line), centered at 425 nm, is within the excitation spectrum of the FBTF dye (orange line). In addition, the FBTF emission spectrum (green line) hardly overlaps the excitation spectrum of the QDs (red line), making the re-absorption of FBTF-emitted photons by the QDs unlikely [32].
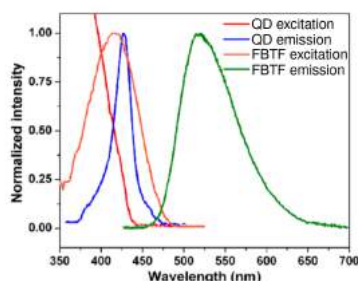
Once the nanocrystals are embedded in the polymer, the PL spectrum only shows the emission spectrum of the dye. The PL spectra overlap all with the emission spectrum of the dye at ∼ 535 nm, as shown on the left in Figure 6.17.

The transmission spectra of the nanoscintillators is shown on the right in Figure 6.17. It should be noted that all scintillators were of different lengths, so that a direct comparison of the transmittance as a function of the filling factor was unambiguously possible. Nevertheless, the low transmittance below 500 nm is due to self-absorption of the nanocrystals, visible in the PL excitation spectra in Figure 6.11. All scintillators show low transmission below 500 nm, which is in the domain of the PL emission spectra, shown on the left in Figure 6.17, and very high transmittance above 500 nm, reaching almost 80 %.

If focusing on the two nanocomposites with 50 and 56 % filling factors, respectively, and 2 and 2.5 mm thickness, respectively, higher transmittance for lower filling factor is expected because of lower self-absorption. This is shown on the right in Figure 6.17.

Since the third nanocomposite has the lowest filling factor and the greatest thickness, it is difficult to classify its transmission behavior based on

Figure 6.10: Photographs in ambient light of three CdZnS/ZnS nanocomposites of 10 mm diameter with their corresponding filling factor and thickness.

Figure 6.11: PL excitation and emission spectra of CdZnS/ZnS quantum dots (QDs) with core/shell structure and the flourescent dye FBTF in dilute solutions, with λ_{exc}(QD) = 350 nm and λ_{exc}(FBTF) = 420 nm. Figure adapted from Liu et al. [32].

these two parameters. However, the figure shows that its transmittance lies between the transmittance of the other two over the entire wavelength range.

Lacking more detailed measurements over a wider range of filling factors and possibly also at different thicknesses, no systematic behavior can be drawn from these three measurements alone.
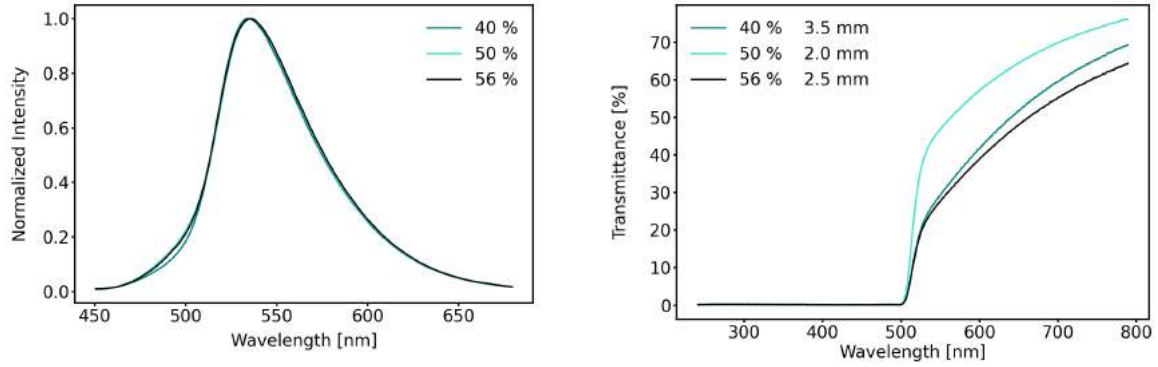

Figure 6.12: On the left, PL emission spectra of the nanocomposite made of CdZnS/ZnS quantum dots (QDs) embedded in PVT/FBTF with different filling factors. For all scintillators, a maximum emission is reached at ~ 535 nm. On the right, transmission spectra of the CdZnS/ZnS nanocomposite with different filling factors, with the maximum transmittance highlighted on the right of each plot. The scintillators were of different lengths, making a direct comparison of the transmittance as a function of filling factor impossible. Nevertheless, very high transmittance of almost 80 % was achieved for these scintillators.

Light Output

The CdZnS/ZnS nanoscomposites showed sufficiently high stopping power owing to their significantly higher filling factor such that their light output could be measured with a ^{137}Cs source. For these measurements the scintillators were wrapped in Teflon and attached to the PMT using air coupling. For each scintillator the light output was calculated with Equation 5.7, and the corresponding energy resolution deduced with Equation 5.8. The results are summarized in Table 6.4. As the table shows, already with air coupling all scintillators exhibit light outputs of approximately 5 000 ph MeV^{-1}. If optical grease is used the light output can be roughly doubled. It should be noted, however, and also in light of what was mentioned above, the light output also depends on the scintillator thickness and since all scintillators were not of equal thickness, a direct comparison of the light output as a function of the filling factor was not possible.

c_{NC}	Dimension	Light Output	Energy Resolution
[wt %]	[mm^3]	[ph MeV^{-1}]	[%]
40	$3 \times 3 \times 3.5$	$4\,548 \pm 318$	24.7 ± 1.3
50	$3 \times 3 \times 2.0$	$5\,265 \pm 369$	18.3 ± 3.1
56	$3 \times 3 \times 2.5$	$4\,884 \pm 342$	23.6 ± 1.0

Table 6.4: Results of light output and energy resolution of CdZnS/ZnS nanocrystals in PVT/FBTF as a function of filling factor using ^{137}Cs. The scintillators were wrapped in Teflon and coupled to the photodetector with air. c_{NC} denotes the filling factor.

Scintillation Kinetics

The scintillation distributions for CdZnS/ZnS nanocrystals in PVT/FBTF are shown in Figure 6.13. They were fitted with Equation 5.11, resulting in three decay times and two rise times. In contrast to the perovskite nanocomposites described above, no prompt component was observed, instead, a second rise time could clearly be resolved, which was still below 2 ns. The first rise time could not be resolved due to the limitation of the IRF and was therefore assumed within 160 ps. The effective decay time was calculated using Equation 5.12. The results of this are summarized in Table 6.5. As the table shows, none of the decay times is in the sub-nanosecond range, but still below 50 ns. The first decay time τ_{d1} of ~ 4 ns contributes with $\sim 20\%$, the second decay time τ_{d2} of ~ 7 ns dominantly with $\sim 70\%$, and the third decay time τ_{d3} of ~ 40 ns with $\sim 10\%$ abundance, resulting in an effective decay time from 6 and 7 ns. Looking at the effective decay time alone, faster scintillation kinetics are observed as the filling factor increases.
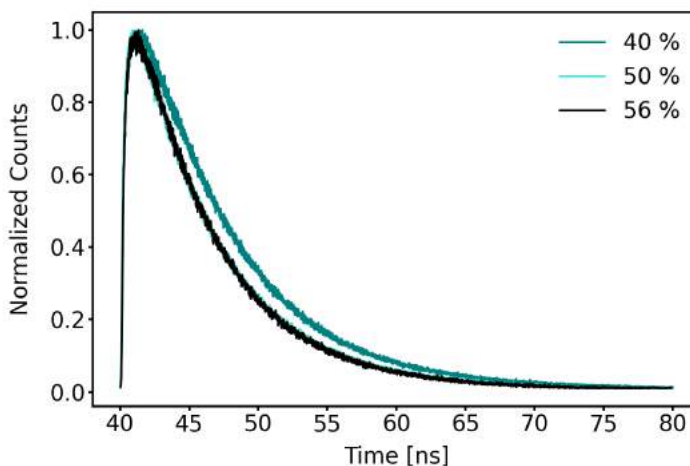
Figure 6.13: Scintillation distributions of CdZnS/ZnS nanocrystals in PVT/FBTF with different filling factors. Faster scintillation kinetics are observed as the filling factor increases.

Table 6.5: Results of the scintillation kinetics with X-rays of CdZnS/ZnS nanocrystals in PVT/FBTF. The scintillation distributions were fitted with Equation 5.11, resulting in three decay times and a resolvable rise time apart from the IRF of the system. c_{NC} denotes the filling factor, τ_r the rise time, $\tau_{d,i}$ are the decay times and R_i their corresponding abundances, respectively, and $\tau_{d,eff}$ the effective decay time, determined with Equation 5.12.

c_{NC}	τ_r	τ_{d1}	R_1	τ_{d2}	R_2	τ_{d3}	R_3	$\tau_{d,eff}$
[wt%]	[ns]	[ns]	[%]	[ns]	[%]	[ns]	[%]	[ns]
40	1.7 ± 0.1	4.6 ± 0.3	22 ± 2	7.4 ± 0.4	69 ± 4	43.2 ± 2.2	9 ± 1	7.0 ± 0.4
50	1.0 ± 0.1	4.3 ± 0.3	20 ± 1	6.7 ± 0.4	70 ± 4	39.0 ± 2.0	10 ± 1	6.4 ± 0.2
56	1.5 ± 0.1	3.2 ± 0.2	16 ± 1	6.6 ± 0.4	74 ± 4	46.2 ± 2.4	9 ± 1	6.1 ± 0.2

Detector Time Resolution

The time delay distributions of CdZnS/ZnS nanocrystals in PVT/FBTF were fitted with Equation 5.19. The time resolutions of these were extracted as the FWHM of the corresponding fits. The results of the detector time resolution are summarized in Figure 6.6. All samples showed a time

resolution of ~1 ns. Even if the different lengths of the scintillators were taken into account, no clear trend becomes visible from the effect of the filling factor.

c_{NC} [wt %]	Dimension [mm^3]	DTR [ps]
40	$3 \times 3 \times 3.5$	1374 ± 69
50	$3 \times 3 \times 2.0$	947 ± 47
56	$3 \times 3 \times 2.5$	1028 ± 51

Table 6.6: Results of the detector time resolution (DTR) of CdZnS/ZnS nanocrystals in PVT/FBTF measured with X-rays. c_{NC} denotes the filling factor. The nanocomposites were coupled with Meltmount to the SiPM. The values are corrected for time walk and given in FWHM.

Conclusion

Significantly higher filling factors of up to 56 % were achieved for nanocomposites made of CdZnS/ZnS with a core/shell structure embedded in PVT/FBTF as compared to the previously presented perovskite nanocomposites , which leads to a significantly higher stopping power. They also exhibited very high transmission of up to ~80 % despite these high filling factors. Already with air coupling reasonable light outputs were achieved. Overall, no significantly different performance was observed neither in terms of the filling factor nor of the scintillator thickness. This, however, was to be expected as the supplied nanoscintillators did not differ much in filling factor (only within a small range of 40 to 45 %). In comparison with the formally investigated perovskite nanoscintillators, these CdZnS/ZnS nanoscintillators clearly show slower scintillation kinetics with effective decay times of 6 to 7 ns, which, nonetheless, are still faster than commonly used scintillators such as LSO, as shown in Table 3.1. With these properties this set of nanocomposites could be a potential candidate for scintillators to be used in calorimetry.

6.4 HfO₂ Nanoscintillators

A nanocomposite of HfO₂ nanocrystals embedded in polyvinyltoluene (PVT) with the addition of 2-(4-tert-butylphenyl)-5-(4-biphenylyl)-1,3,4-oxadi-azole (PBD) as a primary dye and 1,4-bis(5-phenyl-2-oxazolyl)benzene (POPOP) as a secondary dye, was supplied by UCLA. The nanocomposite was produced by direct polymerization, as described in Section 4.4, resulting in a filling factor of 20 %. It should be noted that the scintillator had about twice the thickness of the commonly used scintillator pixels.

The addition of a dense material to an organic scintillator increases the stopping power of the scintillator. HfO₂ is a good candidate for such a material due to its high optical transparency in the UV and visible range, high mass density $\rho\,(HfO_2) = 9.6\,g\,cm^{-3}$ and high atomic number of hafnium $(Z\,(Hf) = 72)$ [53]. Another study of HfO₂ nanocomposites, that is HfO₂ nanocrystals embedded in polystyrene, led to a joint publication with CTU and the FZU Institute of Physics in Prague, Czech Republic: "First investigation of the morphological and luminescence properties of HfO₂ nanoparticles synthesized by photochemical synthesis" in CrystEngComm [53]. They are not considered in this work as they were in the form of thin platelets and thus not suitable for calorimetry.
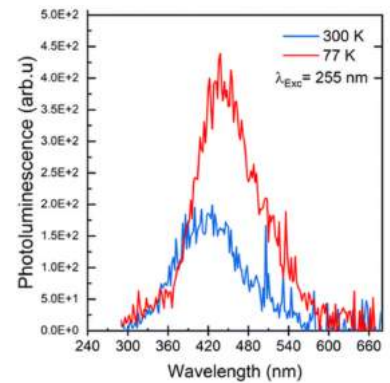
Figure 6.14: PL emission spectra of HfO₂ nanocrystals (annealed at 450 °C) under UV excitation at different temperatures. Figure adapted from Villa, Frank et al. [53].
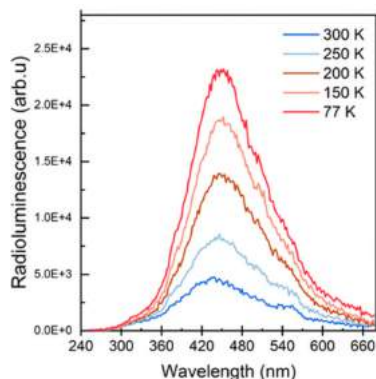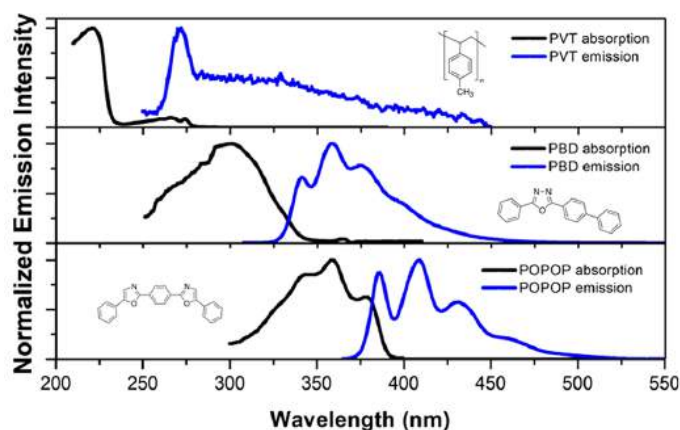
Figure 6.15: RL spectra of HfO₂ nanocrystals (annealed at 450 °C). Figure adapted from Villa, Frank et al. [53].

Figure 6.16: Excitation (black lines) and emission (blue lines) spectra of PVT in cyclohexane, PBD in cyclohexane (λ_{ex} = 303 nm), and POPOP in cyclohexane ((λ_{ex} = 358 nm). Adapted figure from Han et et. [35].

Optical Properties

The photoluminescence (PL) and radioluminescence (RL) spectra of HfO₂ nanocrystals are shown in Figure 6.14 and Figure 6.15, respectively, and measured at different temperatures. Both PL and RL spectra are from the study of HfO₂ nanocomposites mentioned above and show the wide range of optical transparency of HfO₂ nanocrystals [53]. The absorption and emission spectra of PVT and the two dyes are shown in Figure 6.16. scintillators.

The PL emission spectrum of HfO₂ nanocrystals embedded in PVT/PBD/POPOP is shown on the left in Figure 6.17. As already mentioned in Section 3.2, fluorescent dyes are used to shift the emitted light to longer wavelengths, usually in the range of visible light. The emitted light is first shifted by PBD as primary dye to ∼ 360 nm, which is then shifted to ∼ 410 nm by POPOP as the secondary dye. The effect of WLS is clearly visible in the PL spectrum of the nanocomposite on the left in Figure 6.17. The emission of the nanocomposite reaches a maximum at 423 nm, with a broadening towards higher wavelengths. This emission maximum overlaps with the emission maximum of POPOP. Since the HfO₂ emission spectrum is broad, from 360 to 540 nm as shown in Figure 6.14), this also leads to a broadening of the nanocomposite emission spectrum visible as a shoulder in the spectrum shown on the left in Figure 6.17.

The transmission spectrum of the nanocomposite is shown on the right in Figure 6.17. The scintillator shows low transmittance below 400 nm, due to self-absorption of the nanocrystals and the dyes and exhibits very high transparency above 400 nm, reaching a maximum transmittance of 87 %.
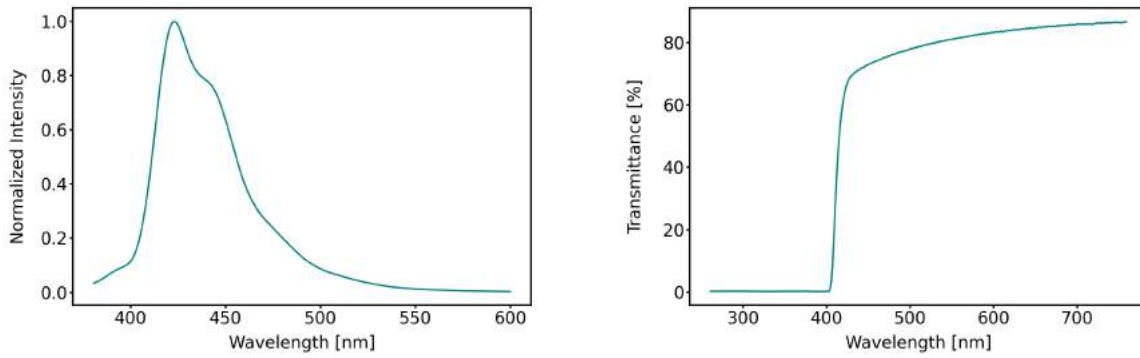
Figure 6.17: On the left, PL emission spectra of HfO$_2$ nanocrystals embedded in PVT/PBD/POPOP. On the right, transmission spectra of the same nanocomposite. It shows very high transmittance of almost 90 %.

Light Output

For the light output measurement, using ^{137}Cs, the HfO$_2$ nanocomposite was wrapped in Teflon and attached to the PMT using air coupling, similar to the light output measurements of the previously presented CdZnS/ZnS nanocomposites. The energy spectrum of the scintillator is shown in Figure 6.18. The light output was calculated with Equation 5.7, and the corresponding energy resolution with Equation 5.8. The results are summarized in Table 6.7. Already with air coupling a light output of $\sim 6\,000$ ph MeV^{-1} was reached, with an energy resolution of ~ 10 %.
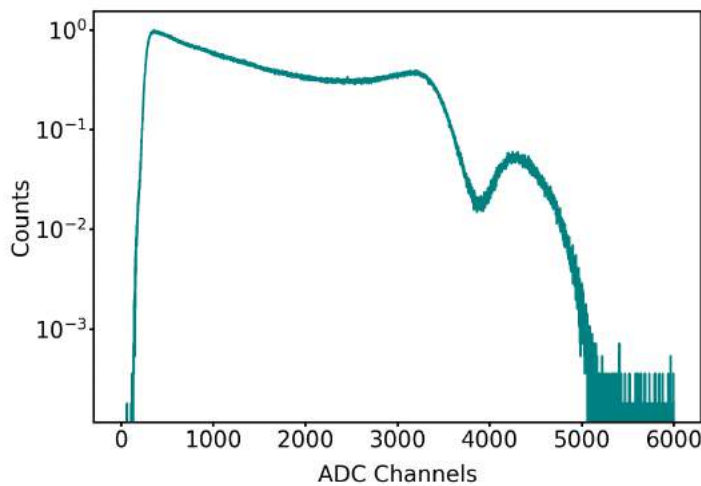
Figure 6.18: Energy spectrum of HfO$_2$ nanocrystals in PVT/PBD/POPOP using ^{137}Cs. The spectrum is shown on a logarithmic scale. The photopeak at around 4 300 ADC channels was fitted with Equation 5.5 to obtain the light output of the scintillator.

c_{NC}	Dimension	Light Output	Energy Resolution
[wt %]	[mm^3]	[ph MeV^{-1}]	[%]
20	$3 \times 3 \times 6$	5992 ± 419	11.7 ± 1.0

Table 6.7: Results of light output and energy resolution of HfO$_2$ nanocrystals in PVT/PBD/POPOP using ^{137}Cs. The scintillator was wrapped in Teflon and coupled to the photodetector with air. c_{NC} denotes the filling factor.

Scintillation Kinetics

The scintillation distribution for HfO_2 nanocrystals embedded in PVT/PBD/POPOP is shown Figure 6.19. It was fitted with Equation 5.11, resulting in three decay times and two rise times. In contrast to the perovskite nanoscintillators described above, no prompt component was observed. Instead similar to the CdZnS/ZnS nanoscintillators, a second visible rise time in the subnanosecond range was observed. The first rise time could not be resolved because limited by the IRF of the system and was therefore assumed to be below 160 ps. The effective decay time was calculated using Equation 5.12. The results are summarized in Table 6.8. Similar to the CdZnS/ZnS nanoscintillators, none of the decay times is in the sub-nanosecond range, but still below 50 ns, whereby the first decay time τ_{d1} of ~ 2 ns dominates with ~ 76 %, the second decay time τ_{d2} of ~ 3 ns with ~ 15 % and the third decay time τ_{d3} of ~ 40 ns with ~ 10 % abundance, resulting in an effective decay time of 2.3 ns.
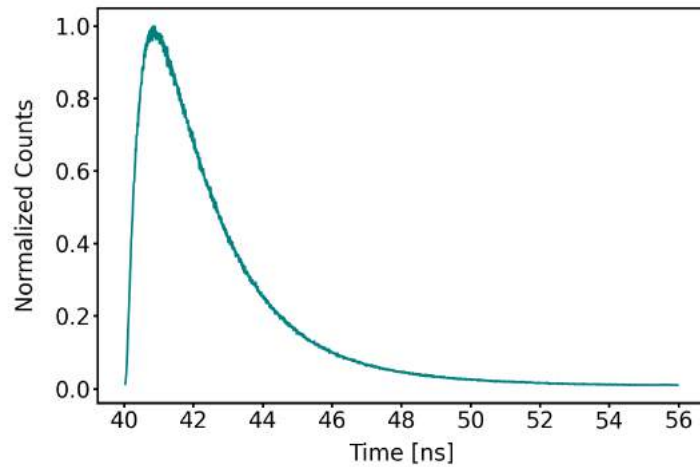
Figure 6.19: Scintillation distribution of HfO_2 nanocrystals in PVT/PBD/POPOP with 20 % filling factor.

Table 6.8: Results of the scintillation kinetics with X-rays of HfO_2 nanocrystals in PVT/PBD/POPOP. The scintillation distribution was fitted with Equation 5.11, resulting in three decay times and a resolvable rise time apart from the IRF of the system. c_{NC} denotes the filling factor, τ_r the resolvable rise time, $\tau_{d,i}$ are the decay times and R_i their corresponding abundances, respectively, and $\tau_{d,eff}$ the effective decay time, determined with Equation 5.12.

c_{NC} [wt %]	τ_r [ns]	τ_{d1} [ns]	R_1 [%]	τ_{d2} [ns]	R_2 [%]	τ_{d3} [ns]	R_3 [%]	$\tau_{d,eff}$ [ns]
20	0.62 ± 0.04	1.9 ± 0.1	76 ± 4	3.1 ± 0.2	15 ± 1	43.8 ± 2.2	10 ± 1	2.3 ± 0.1

Detector Time Resolution

The time delay distribution of the 6 mm thick HfO_2 nanocomposite was fitted with Equation 5.19. The time resolution was extracted as the FWHM of the corresponding fit, and corrected for time walk. It resulted in 791 ± 40 ps.

Conclusion

The nanocomposite made of HfO$_2$ nanocrystals embedded in PVT/PB-D/POPOP, despite its relatively large thickness of 6 mm, showed very promising optical properties with high stopping power and light output benefiting from the high density and high Z-number of HfO$_2$. In addition it exhibited fast timing with an effective decay time of 2.3 ns, yielding, however only a DTR of ∼ 800 ps. With its properties this nanocomposite could be a potential candidate for scintillators to be used in calorimetry.

6.5 (PEA)$_2$PbBr$_4$ Perovskite Nanoscintillators

A set of hybrid organic–inorganic perovskites (HOIPs) of lithium-doped (Li-doped) and undoped two-dimensional (2D) perovskite crystals made of (PEA)$_2$PbBr$_4$ (PEA) was provided by CINTRA. The characterization and investigation of the scintillators and the effects of lithium doping on scintillation and timing performance led to a joint publication with CINTRA and the Łukasiewicz Research Network-PORT Polish Center for Technology Development in Wrocław, Poland: "Sub-100- picosecond time resolution from undoped and Li-doped two-dimensional perovskite scintillators" in Applied Physics Letters [36].

Photographs of the two scintillators are shown in Figure 6.20. As the photographs show, the scintillators were irregular in shape and thickness, both with a size of ∼ 5 × 5 × 2 mm^3. The scintillators have a mass density of 2.5 g cm^{-3} and an effective atomic number of 33.

Optical Properties

The photoluminescence (PL) spectra of the two (PEA)$_2$PbBr$_4$ scintillators are shown in Figure 6.21. Both scintillators show a double peak structure with maxima at roughly 410 and 430 nm. This is an indication of a double band gap structure due to an energy difference between surface and bulk states. In addition, Li-doped (PEA)$_2$PbBr$_4$ shows a lower intensity of the emission maximum at ∼ 410 nm compared to undoped (PEA)$_2$PbBr$_4$. This effect is a result of self-absorption.
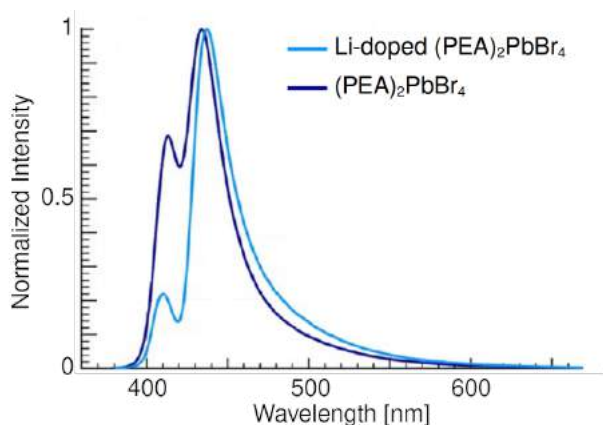

Figure 6.20: Photographs in ambient light of single crystals of Li-doped and undoped (PEA)$_2$PbBr$_4$, irregular in shape and thickness. Figure adapted from Cala', Frank et al. [36].

Figure 6.21: PL emission spectra of Li-doped and undoped (PEA)$_2$PbBr$_4$ (λ_{exc} = 350 nm). Figure adapted from Cala', Frank et al. [36].

Light Output

For the light output measurements using ^{137}Cs both (PEA)$_2$PbBr$_4$ scintillators were wrapped in Teflon and coupled to the PMT using Rhodorsil optical grease. The energy spectra of both scintillators are shown in Figure 6.22. They both exhibit two peaks, where the left one is the escape peak from the K-shell absorption edge of lead, while the right one is the photopeak at 661.7 keV. The resulting light outputs and energy resolutions are reported in Table 6.9. Doping (PEA)$_2$PbBr$_4$ with lithium increased the light output by $\sim 24\%$, reaching more than 20 000 ph MeV^{-1}. Also the energy resolution improved by $\sim 31\%$ when (PEA)$_2$PbBr$_4$ was doped with lithium.

Figure 6.22: Energy spectra of Li-doped and undoped (PEA)$_2$PbBr$_4$ using ^{137}Cs. Both scintillators exhibit two peaks, the left one is the escape peak from the K-shell absorption edge of lead, while the right one in both cases is the photopeak at 661.7 keV. Figure adapted from Cala', Frank et al. [36].
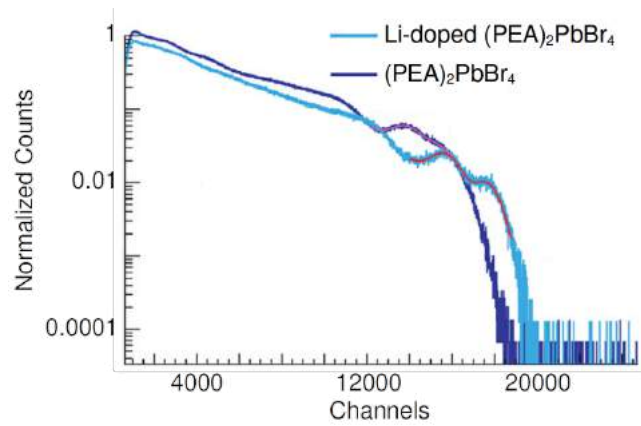
Table 6.9: Results of light output and energy resolution of Li-doped and undoped (PEA)$_2$PbBr$_4$ (PEA) using ^{137}Cs. The scintillators were wrapped in Teflon and coupled with Rhodorsil optical grease to the photodetector. Results published in Cala', Frank et al. [36].

Material	Light Output [ph MeV^{-1}]	Energy Resolution [%]
(PEA)$_2$PbBr$_4$	$17\,300 \pm 1730$	11.5 ± 1.2
Li-doped (PEA)$_2$PbBr$_4$	$21\,400 \pm 2140$	8.0 ± 0.8

Scintillation Kinetics

The scintillation distributions for the two (PEA)$_2$PbBr$_4$ scintillators are shown in Figure 6.23. They were fitted with Equation 5.14 to describe the ultra-fast emission, resulting in three decay times and a prompt component. The effective decay time was calculated using Equation 5.15. The results are summarized in Table 6.10. Faster scintillation kinetics were observed for the Li-doped (PEA)$_2$PbBr$_4$, with an effective decay time of 14.7 ± 0.8 ns in contrast to 16.1 ± 0.9 ns achieved for the undoped (PEA)$_2$PbBr$_4$ and with comparable R_p fractions. Non of the decay times is in the sub-nanosecond range, but still within 100 ns. Also the abundance of the prompt emission R_p is only $\sim 10\%$, and the first decay time (~ 2 ns) is represented with only a small abundance of $\sim 2\%$.
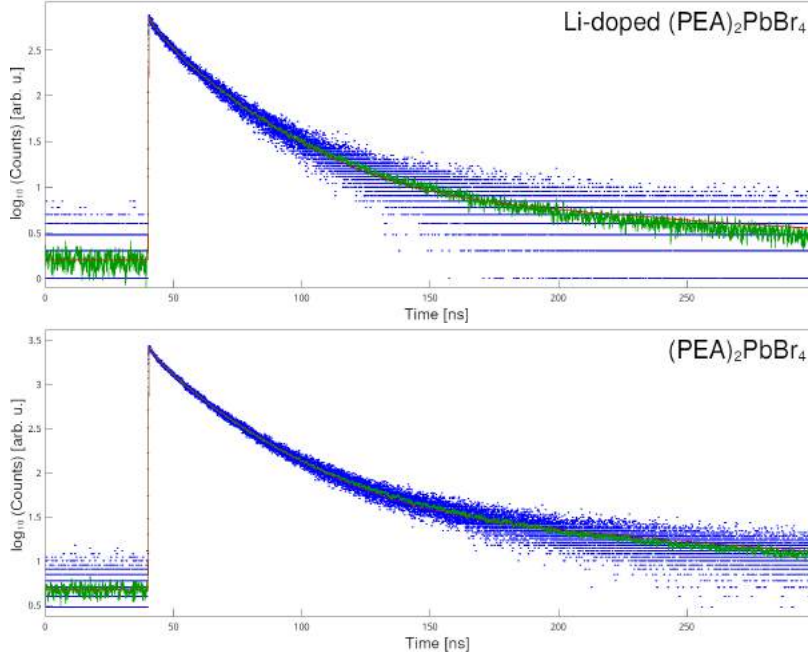
Figure 6.23: Scintillation distributions of Li-doped and undoped $(PEA)_2PbBr_4$. The scintillation decays are shown on a semi-logarithmic scale. The blue dots are the measured data, the green line is their average, and the red curve denotes the fit. Figure adapted from Cala', Frank et al. [36].

Table 6.10: Results of the scintillation kinetics with X-rays of Li-doped and undoped $(PEA)_2PbBr_4$, denoted with Li - PEA and PEA, respectively. The scintillation distributions were fitted with Equation 5.14, resulting in three decay times and a prompt component. $\tau_{d,i}$ are the decay times and R_i their corresponding abundances, respectively, R_p is the abundance of the prompt emission, and $\tau_{d,eff}$ the effective decay time, determined with Equation 5.15. Results published in Cala', Frank et al. [36].

Material	R_P [%]	τ_{d1} [ns]	R_1 [%]	τ_{d2} [ns]	R_2 [%]	τ_{d3} [ns]	R_3 [%]	$\tau_{d,eff}$ [ns]
PEA	13 ± 2	2.4 ± 0.2	2.3 ± 0.2	15.5 ± 0.8	62 ± 4	83.8 ± 4.2	20 ± 1	16.1 ± 0.9
Li - PEA	14 ± 2	2.3 ± 0.2	2.5 ± 0.2	13.7 ± 0.7	59 ± 3	68.0 ± 3.4	23 ± 2	14.7 ± 0.8

Conclusion

Doping $(PEA)_2PbBr_4$ with lithium improved all scintillation and timing properties. One of the strengths of these 2D HOIP scintillators, both doped and undoped, is the very favorable light output and energy resolution achieved with even small pixels, but at the expense of lower scintillation kinetics. Their low mass density and low effective atomic number lead to a radiation absorption length at 511 keV of 4.25 cm, which is four times longer compared to high-density LSO:Ce:Ca at 1.16 cm. Furthermore, these scintillators can be fabricated by a cost-effective solution process at low temperatures (below 100 °C) [54]. Nevertheless, a major disadvantage of this type of scintillator is the size limitation during production. So far, they cannot be manufactured on a large scale or in different dimensions, as shape control during production is poor. They are also limited in their handling as they are very fragile. This does not make them potential candidates for scintillators in calorimetry at this point in time. However, these 2D HOIP scintillators remain potential candidates for fast timing applications.

6.6 Summary and Conclusion

In this chapter, the characterization results of the studied nanoscintillators were presented. The main results are summarized in Table 6.11. The properties of two conventional scintillators are also listed for comparison. The well-known LYSO:Ce crystal was chosen as a representative of a scintillator with an extremely high light yield, while the plastic scintillator EJ232 [11] was selected for its very fast timing properties. The studied nanocomposites can simply be considered as plastic scintillators hosting a specified amounts of nanocrystals.

Table 6.11: Summary of some physical, scintillation and timing properties of the studied nanomaterials and two conventional scintillators. The light output was measured with ^{137}Cs (661.7 keV), whereby the scintillator was attached to the PMT either with air coupling * or optical coupling **. The scintillation kinetics and the time resolution (FWHM) were measured with X-rays (up to 40 keV). c_{NC} denotes the filling factor, $\tau_{d,eff}$ the effective decay time and DTR the detector time resolution.

Material	c_{NC} [wt %]	Dimension [mm^3]	Light Output [ph MeV^{-1}]	τ_{eff} [ns]	DTR [ps]
CsPbBr$_3$ in PMMA/PLA [27]	0.05	$3 \times 3 \times 3$	–	1.1 ± 0.1	–
CsPbBr$_3$ in PMMA/PLA [27]	0.1	$3 \times 3 \times 3$	–	1.8 ± 0.1	–
CsPbBr$_3$ in PMMA/PLA [27]	0.2	$3 \times 3 \times 3$	–	1.5 ± 0.1	–
CsPbBr$_3$ in PMMA/PLA [27]	0.4	$3 \times 3 \times 3$	–	3.3 ± 0.2	–
CsPbBr$_3$ in PMMA/PLA [27]	0.8	$3 \times 3 \times 3$	–	4.1 ± 0.3	–
CsPbBr$_3$ in PS $_{(OA+OLAM)}$ [28]	1	$3 \times 3 \times 0.1$	–	1.9 ± 0.2	305 ± 9
CsPbBr$_3$ in PS $_{(OA+OLAM)}$ [28]	5	$3 \times 3 \times 0.1$	–	2.0 ± 0.2	330 ± 10
CsPbBr$_3$ in PS $_{(OA+OLAM)}$ [28]	10	$3 \times 3 \times 0.1$	–	2.9 ± 0.3	319 ± 9
CsPbBr$_3$ in PS $_{(DDAB)}$ [28]	1	$3 \times 3 \times 0.1$	–	2.9 ± 0.3	308 ± 9
CsPbBr$_3$ in PS $_{(DDAB)}$ [28]	5	$3 \times 3 \times 0.1$	–	2.4 ± 0.2	309 ± 9
CsPbBr$_3$ in PS $_{(DDAB)}$ [28]	10	$3 \times 3 \times 0.1$	–	2.6 ± 0.2	295 ± 8
CdZnS/ZnS in PVT/FBTF	40	$3 \times 3 \times 3.5$	4548 ± 318 *	7.0 ± 0.2	1374 ± 69
CdZnS/ZnS in PVT/FBTF	50	$3 \times 3 \times 2.0$	5265 ± 369 *	6.4 ± 0.2	947 ± 47
CdZnS/ZnS in PVT/FBTF	56	$3 \times 3 \times 2.5$	4884 ± 342 *	6.1 ± 0.2	1028 ± 51
HfO$_2$ in PVT/PBD/POPOP	20	$3 \times 3 \times 6.0$	5992 ± 419 *	2.3 ± 0.1	791 ± 40
(PEA)$_2$PbBr$_4$ [36]	–	$\sim 5 \times 5 \times 2$	$17\,300 \pm 1730$ **	16.1 ± 0.9	–
Li-doped (PEA)$_2$PbBr$_4$ [36]	–	$\sim 5 \times 5 \times 2$	$21\,400 \pm 2\,140$ **	14.7 ± 0.8	–
EJ232	–	$3 \times 3 \times 3$	$8\,400$ [11]	1.48 ± 0.01 [41]	314 ± 5 [41]
LYSO:Ce	–	$3 \times 3 \times 3$	$41\,100$ ** [17]	38 ± 1 [41]	714 ± 18 [41]

In conclusion, the studies of scintillating nanomaterials showed the great potential of nanoscintillators especially in terms of fast timing. Prompt emission with decay times in the sub-nanosecond range was observed for most nanomaterials. A time resolution of ~ 300 ps FHWM was achieved for nanocomposites made of CsPbBr$_3$ nanocrystals in polystyrene. In terms of light output, a few nanoscintillators can already compete with conventional plastic scintillators. A light output of around $6\,000$ ph MeV^{-1} was achieved for a nanocomposite made of HfO$_2$ nanocrystals in PVT/PBD/POPOP, and more than 200000 ph MeV^{-1} for 2D perovskites of Li-doped (PEA)$_2$PbBr$_4$.

However, most of the nanoscintillators known today do not produce enough light to be used in high energy physics calorimetry or PET. This can either be due to filling factors being too low and therefore leading to insufficient stopping power for particle interactions with the scintillator materials. Another obstacle for the use of these scintillators is their often poor transparency at higher filling factors caused by self-absorption of the nanocrystals. It appears to combine both fast timing capability and high light output in one single matrix cannot be achieve at the present time. But on the other hand, the characterization results of these nanomaterials show that these devices could be tailored to the specific needs of intended applications.

Future R&D needs to focus on finding most suitable host materials and embedding techniques to achieve higher concentrations of nanocrystals within the composites while preserving the transparency of the scintillator without sacrificing its fast timing properties. This allows then efficient stopping power, high transparency as well as large-scale production.

Nanomaterials in Calorimetry | 7

This chapter describes possible applications of nanomaterials in calorimetry. First a new concept of using nanomaterials in a so-called chromatic calorimeter is presented. Measurements of the timing performance with high energy particles are described. In addition using nanomaterials in a shashlik calorimeter is presented, this work was done in the frame of the "NanoCal" project, as already introduced in Section 4.5.

7.1 Chromatic Calorimeter

An application of nanomaterials in calorimetry could be in a so-called chromatic calorimeter, a novel approach to measure the development of an electromagnetic (or hadronic) shower within a scintillator, with the possibility of obtaining a longitudinal shower profile with a single quasi monolithic device [40]. To form the calorimeter, modules of scintillating nanomaterials containing different quantum dots (QDs) emitting at different wavelengths can be assembled in series, those with the longest wavelengths at the beginning of the module and those with the shortest wavelengths at the end. This configuration was chosen since QDs show broad longitudinal absorption spectra, but rather narrow emission spectra. By measuring the scintillation photons with a spectrometer, the wavelength can be used to determine in which section they were generated so as to obtain the longitudinal shower profile. Figure 7.1 illustrates the concept of such a calorimeter. This concept led to a joint publication with the Warsaw University of Technology in Warsaw, Poland: "Quantum systems for enhanced high energy particle physics detector" in Frontiers in Physics [40].

The first, most essential and indispensable step is the development and investigation of the performance of these nanomaterials. Measurements of the timing performance made with high energy particles for already existing nanomaterials in beams tests at CERN.
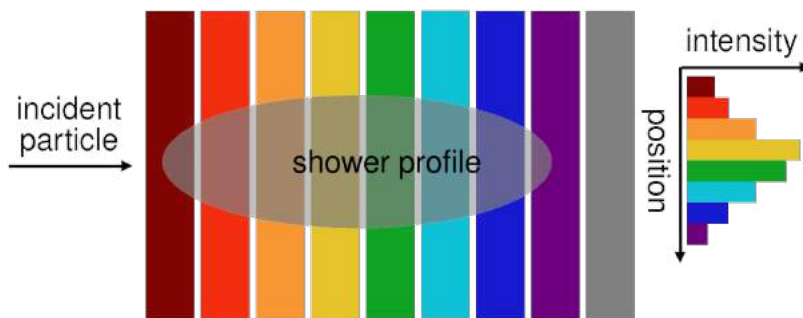
Figure 7.1: Schematic of a chromatic calorimeter using nanomaterials. A concept to measure the development of an electromagnetic (or hadronic) shower within a scintillator with the possibility of obtaining a tomography of the shower with a single quasi monolithic device. It consists of modules of scintillating nanomaterials containing different quantum dots (QDs) emitting at different wavelengths, ideally to cover the entire accessible wavelength spectrum. Figure adapted from Doser, Frank et al. [40].

7.2 Timing Performance with High Energy Particles

Characterization Methods

The CERN Super Proton Synchrotron (SPS), now principally used as a proton injector for the Large Hadron Collider (LHC), also serves as a test beam facility, providing numerous particle beams, including leptons (electrons, muons) and hadrons (pions) with variable momenta up to several hundred GeV/c, ranging from 10 to 400 GeV/c.

During the scheduled beam test activities at the SPS, selected scintillation materials were characterised in terms of their timing performance using minimum ionising particles (MIPs), in this case 150 GeV pions.
The experimental setup in the test beam area is shown in Figure 7.2, a photograph of the test beam area in Figure 7.3.
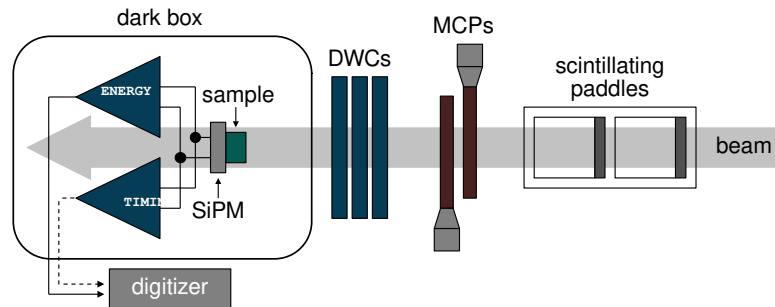
Figure 7.2: Schematic of the experimental setup for the measurements of the timing performance with 150 GeV pions.

It consisted of two plastic scintillating paddles connected to PMTs to provide in coincidence a trigger signal of the arrival of the incident particle, plus two microchannel plate detectors (MCPs) as a time reference, and complemented by three delay wire chambers (DWCs) for particle tracking, using a mixture of Ar/CO_2 and read out by a CAEN V1290N TDC. The ensemble of the detectors was read out by CAEN V1290N TDCs. The scintillators together with the readout electronics were enclosed in a temperature-controlled dark box held at a constant temperature of $16 \pm 0.5\,°C$, arranged in series so that five can be measured in one run. The setup inside the dark box is shown in 7.4. One of the scintillators was a LYSO:Ce:Ca scintillator from FLIR with a dimension of $2 \times 2 \times 3\,mm^3$ for all runs to monitor possible variations in the different runs. The scintillators were wrapped in Teflon and coupled to $3 \times 3\,mm^2$ Hamamatsu S13360-3050PE SiPMs, which were rated with a breakdown voltage of $V_{BD} = 51\,V$ and operated at $V_{BIAS} = 56\,V$, using Meltmount. The light produced by the scintillators was read out using the previously mentioned readout electronics (Section 5.1). The data acquisition system (DAQ) consisted of several electronic modules. NIM modules were employed to control trigger logic. To bias the MCPs and the DWCs, a CAEN high-voltage power supply was used, controlled remotely by a CAEN GECO2020 interface. The waveforms of the SiPM signals, as well as the PMT signals, were recording with a CAEN V1742 digitizer based on a DRS4 chip [55], running at 5 GS/s sampling rate with 500 MHz bandwidth, for offline analysis.
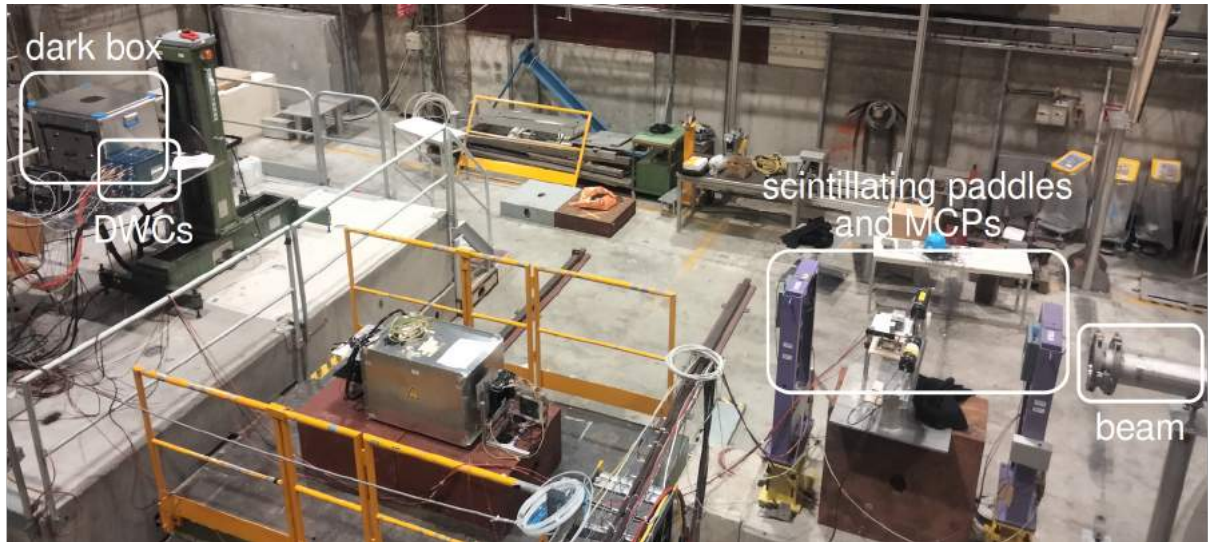
Figure 7.3: Photograph of the CERN SPS test beam area with the experimental setup for all measurements during the test beam activities.
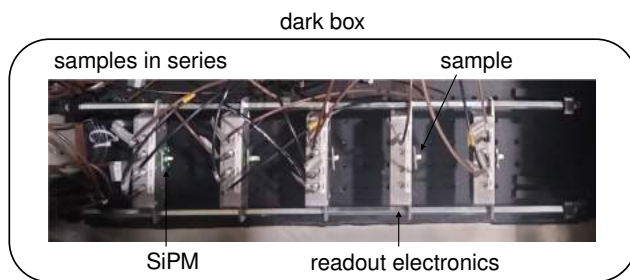
Figure 7.4: View inside the dark box to measure the timing performance in MIP configuration under 150 GeV pion irradiation. It allowed to measure five scintillators in series. One of the scintillators was a LYSO:Ce co-doped 0.4 % Ca scintillator from FLIR with a dimension of $2 \times 2 \times 3$ mm^3 for all runs to monitor possible variations in the different measurment runs. The scintillators were wrapped in Teflon and coupled with Meltmount to 3×3 mm^2 Hamamatsu S13360-3050PE SiPMs.

Data Analysis

The data analysis aimed to determine the time resolution of the scintillators and involved several steps. This section describes the involved steps as well as the exclusion criteria and applied corrections.

Event Tagging and Tracking

A preliminary event selection was made based on the energy deposition in the MCPs. In addition, the beam profile or x-y crossing point of the passing particle was determined from the tracking information of the three DWCs with a precision of 200 µm. An event was defined as the coincidence of the beam particle detected by the three DWCs together with the corresponding energy signal from the SiPM attached to the scintillator under test. An example of this is the scatter plot in 7.5. The scatter plot shows all beam events registered by a DWC together with those in coincidence with the scintillator under test, indicated by the highlighted rectangular area in the center. Only events from the DWCs overlapping with the tested scintillator were selected for subsequent analysis.

Figure 7.5: Scatter plot showing the transverse position of the incident particles in x and y direction as measured by one of the three DWCs in relation to the signal amplitude detected in a scintillator with $2 \times 2 \, mm^2$ surface area. The highlighted square area in the center shows the footprint of the scintillator in coincidence crossed by the beam particles.
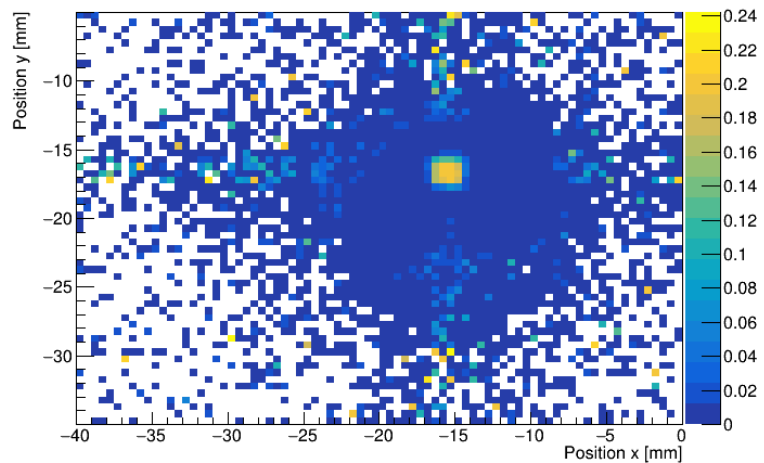
Amplitude Selection

The amplitude of the SiPM energy signal was determined, event by event, from the difference between the baseline averaged over the first 200 samples and the maximum signal amplitude. 7.6 gives an example of the amplitude distribution. I view of deriving the optimum time resolution of the detector, a cut was made around the maximum amplitude of the landau distribution, so as to keep the time walk at a minimum.

Figure 7.6: Amplitude distribution of the SiPM energy signal in the form of a landau distribution where events around the maximum, within the marked interval, were selected for subsequent analysis of the time resolution.
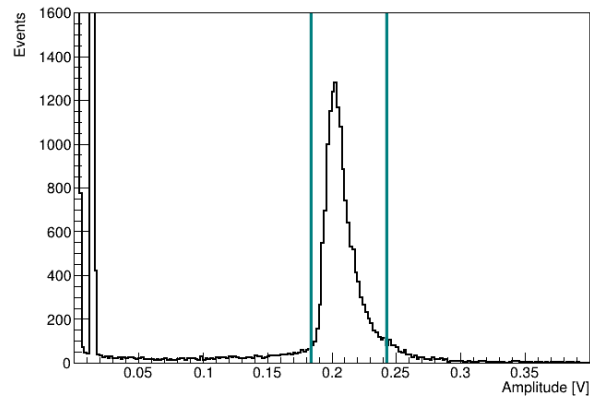
Determination of the Time Resolution

The timestamp of the two reference MCPs was determined, event by event, via constant fraction discrimination at 30 % signal amplitude, resulting in a time resolution between 13 and 15 ps (σ) for all events. The MCP signals acted as the start signals. The stop signals were obtained from the SiPM timing signals via the leading edge threshold technique, similar to the technique applied in the DTR measurements, as explained in detail in Section 5.7. The time delay Δt, an example of which is shown in Figure 7.7, was derived from the time difference between the MCP reference timestamps and the SiPM timing signals, expressed by

$$\Delta t = t_{\text{SiPM}}(th) - \frac{t_{\text{MCP}_1} + t_{\text{MCP}_2}}{2} \, , \tag{7.1}$$

where t_{MCP_1} and t_{MCP_2} are the individual timestamps of the two MCPs and t_{SiPM} is the timestamp of the SiPM timing signal at the threshold th.

The obtained time delay distributions were fitted with a Gaussian, resulting in a fit function given by

$$f(t) = \frac{1}{\sigma \sqrt{2\pi}} \, \exp\left[-\frac{1}{2} \left(\frac{t - \mu}{\sigma} \right)^2 \right] \, , \tag{7.2}$$

where μ is the mean, and σ the standard deviation.

To extract from this the timing contribution made by the scintillator the timing of the MCPs (σ_{MCPs}) was subtracted quadratically from the measured CTR (σ_{meas}), expressed by

$$\sigma_{\text{t}} = \sqrt{\sigma_{\text{meas}}^2 - \sigma_{\text{MCPs}}^2} \, . \tag{7.3}$$
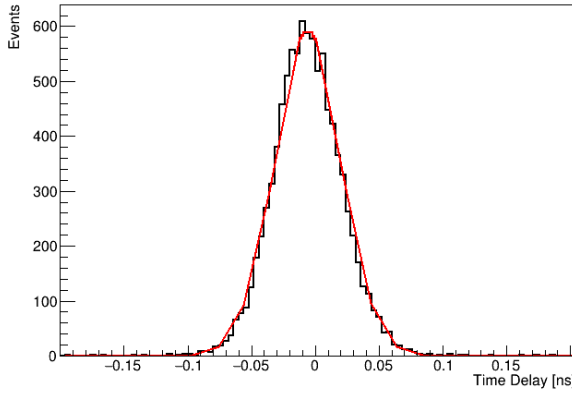
Figure 7.7: Time delay distribution, as the time difference between MCPs and SiPM timing signal, fitted with Equation 7.2.

Time Walk Correction

Signal time walk due to the large Landau fluctuations in the energy deposition of the incoming particles spoils the intrinsic time resolution. To correct for this the correlation between the signal time delay and the energy signal amplitude was used. An example of the correlation is shown in Figure 7.8.

By fitting this correlation with a linear function, given by

$$f(x) = p_1 \cdot x + p_2 \, , \tag{7.4}$$

where x is the signal amplitude, and p_i are the fitting parameters.

As expected, the time walk is smaller at higher amplitudes. Therefore, f was considered as the time walk at a certain amplitude x.

Figure 7.8: Scatter plot of the time delay Δt against the energy signal amplitude. A linear fit was used (Equation 7.4) to model the correlation between these two variables, and then used for time walk correction.
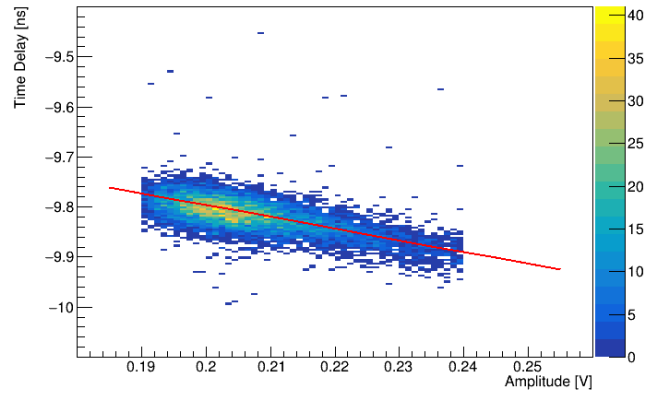
Following this, each time resolution was corrected by

$$\Delta t_{\text{corr}} = \Delta t - t_{\text{corr}} = \Delta t - p_1 \cdot x - p_2 \,, \tag{7.5}$$

where Δt and Δt_{corr} are the time resolutions before and after the time walk correction, respectively, and t_{corr} the correction constant for each event, with signal amplitude x and fitting parameters p_i obtained from Equation 7.4. Many scintillators showed a notable improvement of the time resolution with correcting for time walk .

Determination of the Optimum Time Resolution

To find the optimum time resolution a scan was made, varying the leading edge threshold th set on the SiPM timing signal. For each threshold the time delay distribution was plotted, fitted, and the time resolution extracted and corrected for time walk, as described above.

The time resolution spectrum was then fitted with a fit function given by

$$f(x) = \sqrt{q_1 \cdot x^{q_2} + q_3 \cdot x^{q_4} + q_5} \,, \tag{7.6}$$

where x is the threshold th, and q_i are the fitting parameters.

The minimum of this fit is reported as the optimum time resolution σ. An example is shown in Figure 7.9.
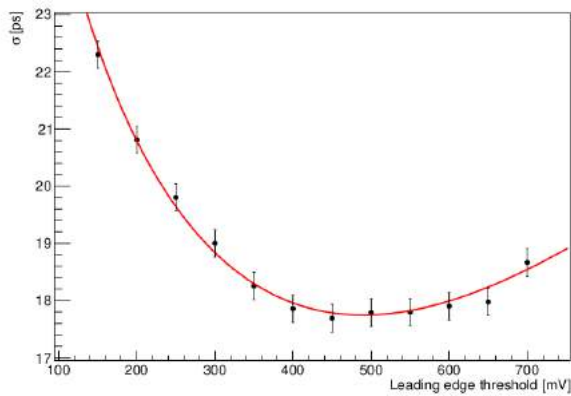
Figure 7.9: Time resolution σ as a function of leading edge threshold th. The optimum time resolution was obtained by a scan, varying the leading edge threshold. The time resolution was fitted with Equation 7.6 and the minimum of the fit taken as the optimum time resolution.

Characterization Results

In the course of this thesis, two test beam runs with high energy particles took place where, in addition to conventional standard scintillators, different newly developed scintillating materials, including nanomaterials, were tested for their timing performance.

Before investigating the timing performance of the scintillators, the SiPM bias voltage was investigated for an optimum setting using conventional scintillators. An improvement in the time resolution was observed with increasing bias voltage, owing to an improved PDE. It should be noted, however, that SiPMs operated under beam conditions and at voltages in excess of 58 V (breakdown voltage of $V_{BD} = 51$ V) over extended periods of time experienced severe signal degradation resulting in increase baseline fluctuations and noise. This finally led to severe damage of the SiPM itself. For this reason, the SiPM bias voltage was limited to 56 V for all measurements.

A $2 \times 2 \times 3\,\mathrm{mm}^3$ LYSO:Ce co-doped 0.4 % Ca crystal from FLIR was used as reference in each run in order to monitor changes in the time resolution measurements and possible signal degradation in the SiPMs (Hamamatsu S13360-3050PE), both in the monitor SiPM and in the SiPM used for the test scintillators.

For the plastic scintillator EJ232, as the reference for nanomaterials, a time resolution of 17.2 ps (σ) was achieved, although the material has a low density, resulting in only a small amount of energy deposited inside the scintillator.

Various nanomaterials were tested, with the initial focus on those showing great potential from previous characterizations or those having a minimum thickness of 2 to 3 mm. In addition, some platelets of nanomaterials were also tested which, although thinner than 1 mm, had a higher filling factor with sufficient transparency. And finally, all materials available at that time were tested within the frame of the "NanoCal" project, presented in detail in the next section. This comprised the nanocomposite of CsPbBr$_3$ in PMMA/PLA, as well as a conventional scintillator of polystyrene (PS) with the addition of p-terphenyl (PTP) (1.5 wt %) and 1,4-bis(5-phenyl-2-oxazolyl)benzene (POPOP) (0.04 wt %), abbreviated as PS/PTP/POPOP.

The obtained time resolutions (σ) are summarized in Table 7.1.

Table 7.1: Results of single detector time resolution (σ) measured in MIP configuration under 150 GeV pion irradiation. c_{NC} denotes the filling factor. The scintillators were wrapped in Teflon and coupled with Meltmount to Hamamatsu S13360-3050P SiPMs. The values are corrected for time walk. The exact composition of the materials can be found in Section 4.4. Some conventional scintillators are shown for comparison. The two scintillators labeled with * were used in the "NanoCal" project.

Material	c_{NC} [wt %]	Dimension [mm^3]	Time Resolution [ps]
CdZnS/ZnS in PVT/FBTF	40	$3 \times 3 \times 3.5$	33.9 ± 1.0
CdZnS/ZnS in PVT/FBTF	50	$3 \times 3 \times 2.0$	36.7 ± 0.7
CdZnS/ZnS in PVT/FBTF	56	$3 \times 3 \times 2.5$	33.5 ± 0.7
HfO$_2$ in PVT/PBD/POPOP	20	$3 \times 3 \times 6$	17.7 ± 0.3
CsPbBr$_3$ in PMMA/PLA*	0.2	$3 \times 5 \times 27$	35.3 ± 1.4
(PEA)$_2$PbBr$_4$	–	$\sim 5 \times 5 \times 2$	50.3 ± 2.7
Li-doped (PEA)$_2$PbBr$_4$	–	$\sim 5 \times 5 \times 2$	45.1 ± 1.3
PS/PTP/POPOP*	–	$3 \times 3 \times 2$	38.0 ± 1.0
EJ232	–	$3 \times 3 \times 3$	17.2 ± 0.2
LYSO:Ce	–	$2 \times 2 \times 10$	13.1 ± 0.4
LSO:Ce:Ca	–	$2 \times 2 \times 10$	12.1 ± 0.4
LYSO:Ce:Ca	–	$2 \times 2 \times 3$	17.1 ± 0.7

As the table shows all nanocomposites of CdZnS/ZnS in PVT/FBTF show a time resolution of $\sim$ 35 ps, whereby they were of different thickness, ranging from 2.0 to 3.5 mm. The nanocomposite of HfO$_2$ in PVT/PBD/POPOP exhibits a time resolution of less than 20 ps, which is approximately the same time resolution as that of EJ232. This a is very promising result in terms of fast timing.

First small pixels of CsPbBr$_3$ in PMMA/PLA with different filling factors were tested. As already discussed in Section 6.1, due to low filling factors these nanocomposites have a very low stopping power and therefore low particle interaction probability especially for MIPs. Remarkably, for nanocomposite pixel with 0.2 % filling factor $\sim$ 27 mm thickness, a time resolution of $\sim$ 35 ps could be achieved compared to $\sim$ 17 ps in a EJ232 scintillator with $\sim$ 3 mm thickness This clearly demonstrates the high timing potential that these nanocomposites are capable of.

As expected from the outset, all tested nanocomposite platelets, despite their higher filling factors, do not achieve sufficient stopping power because of their insufficient thickness. **This prevented to draw any conclusions of their time resolution'**

Both, Li-doped and undoped (PEA)$_2$PbBr$_4$ nanocrystals show time resolutions between 45 and 50 ps, and are thus slower than the tested nanocomposites.

7.3 Shashlik Calorimeter

This section describes the concept of a calorimeter using nanomaterials that could be arranged like a shashlik calorimeter in which light-emitting nanomaterials act as active materials stacked together with passive converters. **marginote shash** In a shashlik calorimeter, light guide fibers or wavelength shifting fibers (WLS) pass through the entire stack of this sandwich arrangement to guide the scintillation light generated in the active material to a photodetector. A schematic of such a calorimeter is shown on the left in Figure 7.10.

The "NanoCal" Project

The "NanoCal" project [38] is founded as part of the European Union's Horizon 2020 Research and Innovation programme (AIDAinnova) [39]. Within this project, different prototypes of shashlik calorimeters using different nanocomposites were developed and evaluated [56].

The calorimeter modules, similar in design to those of calorimeters used in the PANDA[1] and KOPIO[2] experiments [57], each consisted of **12** layers of 0.275 mm thick lead tiles **radiation length of 3.8 cm, ... X_0 check (about 1.5X0)** and an area of 55×55 mm^2 interspaced with scintillating tiles of different thickness. 36 WLS fibers with 1 mm diameter, arranged as shown on the right in Figure 7.10, pass through **symbol diameter** 1.3 mm holes in the scintillator/lead sandwich, bundled and squeezed into a cylindrical collector (ferrule) to be read out by the photodetector. The fiber bundle was then cut flat and coupled with optical grease to a 6×6 mm^2 Hamamatsu S13360-6050PE SiPM which was rated at a breakdown voltage of $V_{BD} = 53$ V and operated at $V_{BIAS} = 55$ V. The calorimeter modules were enclosed in a box designed to hold the tiles together and to shield them from stray light.

1: PANDA experiment at the Facility for Antiproton and Ion Research (FAIR) in Darmstadt, Germany.

2: KOPIO experiment at the Brookhaven National Laboratory (BNL) in Upton, USA.

Figure 7.10: On the left, schematic of a shashlik calorimeter. On the right, schematic of the layout of the calorimeter tiles (not to scale). Fibers with 1 mm in diameter pass through holes in the tiles with an area of 55×55 mm^2.

Three such calorimeter modules were constructed where two modules were equipped with nanocomposites to be compared with one module built with conventional plastic scintillators. Geometrically the modules were similar, only individual WLS fibers were used to adapt to the different wavelengths of the emitted light produced in the different scintillating tiles.

The module with the conventional scintillators from the PANDA prototype consisted of 1.5 mm thick scintillator tiles of polystyrene (PS) with the addition of p-terphenyl (PTP) (1.5 wt %) and 1,4-bis(5-phenyl-2-oxazolyl)benzene (POPOP) (0.04 wt %), as shown in Figure 7.11. They were produced by the Institute for High Energy Physics (IHEP) in Protvino, Russia, and were used together with Kuraray Y-11 (200) [58] WLS fibers (blue-to-green).

The first module with nanomaterials consisted of 3 mm thick nanocomposite tiles of CsPbBr$_3$ nanocrystals (0.2 wt %) embedded in PMMA/PLA, as shown in Figure 7.12. Contrary to the above module it used Kuraray O-2 (100) [58] WLS fibers (green-to-orange).

The second nanocomposite module consisted of 1.5 mm thick nanocomposite tiles of CsPb(BrCl)$_3$ nanocrystals (0.2 wt %) embedded in PMMA/PLA. In this case customized Kuraray 1 mm single clad WLS fibers, referred to as NCA-1 (200) [59], were used to adapt to the wavelength of

Figure 7.11: Photograph of conventional scintillators made of PS with the addition of PTP (1.5 wt %) and POPOP (0.04 wt %) in ambient light, used for one of the three calorimeter module. The tiles have a square matrix of 36 holes. The additional hole in the center, which was originally made to inject light from a LED for calibration, was not used for this prototype.

the emitted light. All nanocomposites and the dye for the customized fibers were supplied by UNIMIB. An overview of the used WLS fibers is given in Table 7.2. Figure 7.13 shows the three modules without their housing.
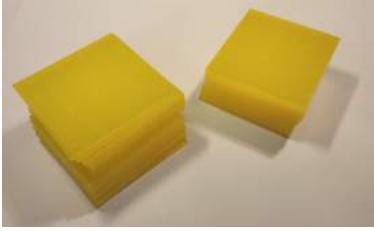
Figure 7.12: Photograph of nanoscintillators made of $CsPbBr_3$ in PMMA/PLA with 0.2 filling factor in ambient light, used for one shashlik calorimeter module. The tiles have a square matrix of 36 holes.

Figure 7.13: Photograph of the calorimeter modules without housing, using $CsPb(BrCl)_3$ nanocomposites and NCA-1 fibers (left), PS/PTP/POPOP and Y-11 fibers (middle), and $CsPbBr_3$ nanocomposites and O-2 fibers (right). The O-2 fibers on the right are already bundled. Figure from Moulson, Frank et al. [60].
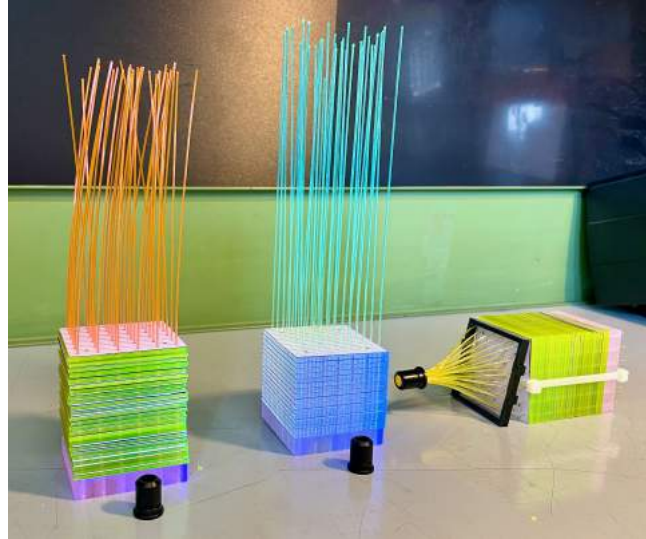
Table 7.2: Overview of used WLS fibers with their assignment to the respective scintillators, where λ_a and λ_e are the maximum absorption and emission wavelengths of the WLS fibers, and λ_{scint} the maximum emission wavelength of the scintillators.

	Scintillator	Fiber	λ_a [nm]	λ_e [nm]	λ_{scint} [nm]
conventional	PS/PTP/POPOP	Y-11 (200) [58]	430	476	425
nanomaterial	$CsPbBr_3$/PMMA/PLA	O-2 (100) [58]	535	550	520
	$CsPb(BrCl)_3$/PMMA/PLA	NCA-1(200)	550	580	520

The CERN PS is also a part of the LHC accelerator complex, used as injector for the SPS, but also serves as a test beam facility, operating numerous particle beams up to tens of GeV/c, including leptons (electrons, muons) and hadrons (pions) with variable momenta up to 15 GeV/c (T9 line).

First measurements were made in test beams at the CERN SPS, followed by further measurements at the DAFNE Beam-Test Facility (BTF) at INFN and at the Proton Synchrotron (PS) at CERN. During scheduled beam test activities at CERN, the prototypes were tested at the SPS with 80 GeV electrons and 150 GeV pions, and at the PS with 1 to 4 GeV electrons and 10 GeV muons. A photograph of two modules in the test beam area is shown in Figure 7.14.

The experimental setup consisted of the calorimeter module and two silicon strip chambers placed in front of the module. The silicon strip chambers were used for tracking and allowed a clear definition of a fiducial region for particles hitting the calorimeter module. This tracking information had sufficient position and angular resolution to resolve individual componentsso that it was possible to distinguish whether the light was generated in the WLS fibers or in the scintillators themselves. The readout of the SiPM was done using a prototype amplification circuit of the CRILIN calorimeter [61]. The output signals were recorded with a CAEN V1742 digitizer, running at 5 GS/s sampling rate.
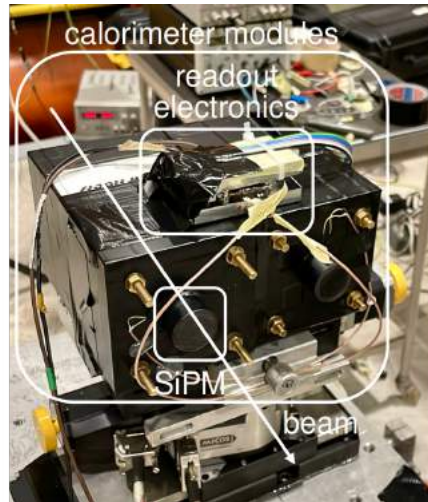
Figure 7.14: Photograph of two shashlik calorimeter modules used in test beam measurements. The modules, similar in composition except for the choice of scintillator material and the WLS fibers, were tested side by side, to allow a direct comparison. Figure adapted from Moulson, Frank [56].

Figure 7.15 shows the hit maps of only two calorimeter prototypes produced by 10 GeV muons. The first one shows the map of the conventional scintillator module and the second one made of $CsPb(BrCl)_3$ nanocomposites. On the other hand no hits other than those in the WLS fibers themselves are seen in the calorimeter module composed of the $CsPb(BrCl)_3$ nanoscintillators, as shown on the right in Figure 7.15. The bright spot in the center is the footprint of the fiber bundle only. This negative results is attributed to the very low filling factors of the nanoscintillators providing insufficient conversion probability to generate light from particle interactions. However, previous characterizations in this context show that PVT may be a more suitable host for nanocomposites, potentially leading to higher light output of the nanocomposites. New nanomaterials have already been developed as part of the "NanoCal" project, showing promising results in first evaluations given rise to new investigations in the future with focus on their use in such a calorimeter [60].
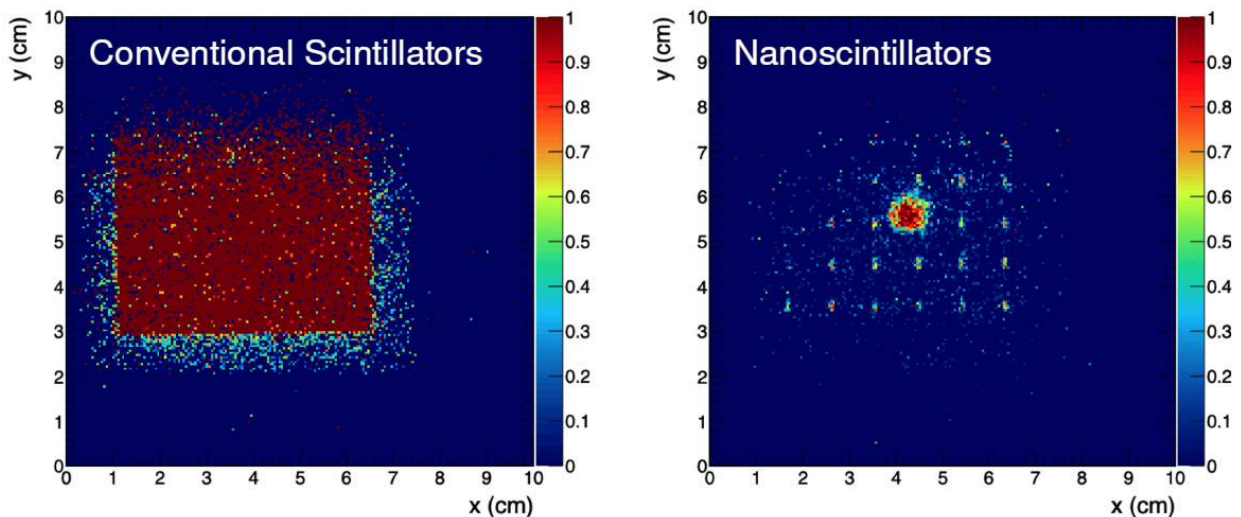
Figure 7.15: Hit maps produced with 10 GeV muons with a threshold of 5 σ_{noise}. On the left, the calorimeter module made of conventional scintillators, and on the right, one module using the $CsPbBr_3$ nanoscintillators. Figure adapted from Moulson, Frank et al. [60].

7.4 Summary and Conclusion

In this chapter, possible applications of nanomaterials in calorimetry have been presented.

The concept of a chromatic calorimeter was presented where scintillating nanomaterials would act both as converter and active material. By using nanoscintillator layers with different optical properties, the vertex can be determined on the basis of the color or wavelength of the emitted photons as well as the longitudinal shower profile. This concept is still in its infancy, however the results obtained so far from the characterization of scintillating nanomaterials could be a starting point for further R&D in this domain to prove the principle of this concept, especially with regard to nanomaterials with higher stopping power.

Promising nanomaterials were investigated in terms of timing under high energy particle irradiation of 150 GeV pions. Several nanoscintillators showed sufficient stopping power to be characterized with high energy particles so that particle interactions can take place within the limited size of the scintillators. The HfO_2 nanocomposite with 20 % filling factor exhibited a time resolution of around 18 ps with a scintillator thickness of 6 mm and was therefore competitive with the conventional scintillators EJ232 and LYSO:Ca:Ce, each of 3 mm thickness. The $CsPbBr_3$ nanocomposite with only 0.2 % filling factor already showed ultra-fast timing in earlier characterization measurements. To increase the particle interaction probability a 35 mm thick scintillator of the same material was tested and reached a time resolution of around 35 ps. This results underlined their potential for timing detectors.

As part of the "NanoCal" project, the feasibility of a shashlik calorimeter made of nanomaterials was investigated. However, compared to the calorimeter module with conventional scintillators, this detector showed some weaknesses in terms of light output. In view of these shortcomings, new nanomaterials are currently being investigated and will be characterized in future beam tests.

Summary and Outlook | 8

The goal of this thesis was to explore innovative scintillating nanomaterials with fast timing for potential applications in high energy experiments at future colliders.

This research was carried out in collaboration with the CERN Quantum Technology Initiative, the CERN Crystal Clear Collaboration and the CERN EP R&D section. The NanoCal project has received funding from the European Union's Horizon 2020 Research and Innovation programme (AIDAinnova) under GA no 101004761. This research led to several publications in scientific journals [27] [28] [36] [40] [41] [53] [62] [63] [64], from which some parts of this work were taken.

The first part of this work comprised the development and characterization of fast scintillating nanomaterials, primarily for their possible utilization in fast timing detectors. Indeed, nanocrystals with size-dependent bandgap structures are capable to meet many of the challenges in the current R&D of scintillating detectors. They exhibit tunable optoelectronic properties, high quantum yields and ultra-fast decay times in the subnanosecond range. However, embedded in polymers, many nanoscintillators show only poor light output. Therefore, future R&D needs to focus on finding the most suitable host materials and embedding techniques to utilize these excellent properties of nanocrystals also embedded in their host materials.

The second part comprised the investigation for their possible application in calorimeters in high energy physics. Promising nanomaterials were investigatedn terms of timing under high energy particle irradiation. In terms of timing, they can already compete with conventional scintillators.

Are these Nanomaterials suitable for Calorimetry?

At the present time, there are two main aspects limiting the use of scintillating nanomaterials in high energy physics calorimetry: size and light output.

A fundamental prerequisite for calorimeters are materials at realistic dimensions. Not only the surface area of a scintillator plays an important role, but also its thickness to provide sufficient stopping power for particle interactions. A common assumption is that high filling factors in nanocomposites translate to higher light output and also higher stopping power. On the other hand, increasing the number of nanocrystals in the polymer also increases their self-absorption and leads to a reduction in light output. It is therefore necessary to identify an optimum between an adequate filling factor of a nanoscintillator and its achievable light output. At this time, scintillating nanomaterials cannot compete with classical materials used in calorimetry.
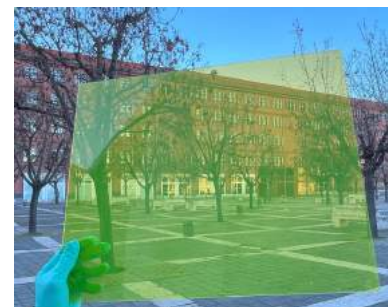
Notwithstanding the above shortcomings of nanoscintillators, the studied nanoscintillators in this work have shown excellent timing performance, a feature that could also be exploited in terms of "timing layers" in a calorimeter independent of energy sampling.

APPENDIX

A

Appendix

A.1 PerkinElmer LS55 Luminescence Spectrometer

Figure A.1 shows a schematic of the optical system of the PerkinElmer LS55 luminescence spectrophotometer, used for photoluminescence measurements to obtain the emission and excitation spectra of the scintillators.
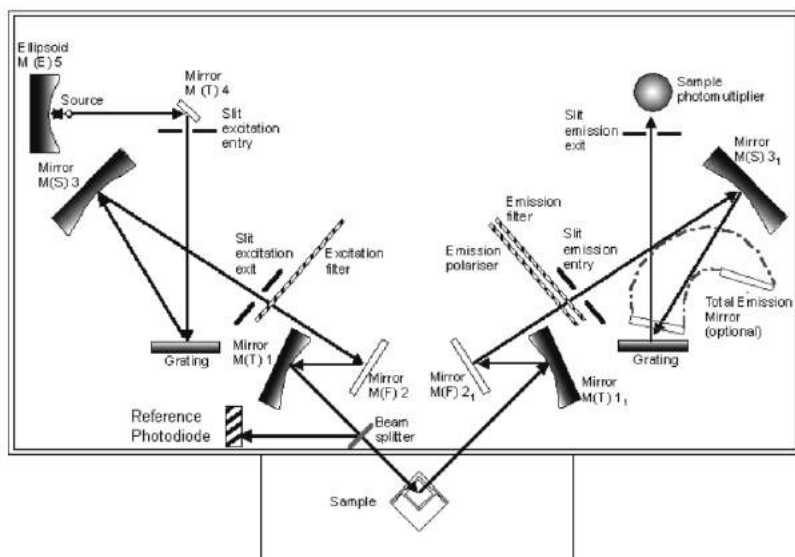
Figure A.1: Schematic of the optical system of the PerkinElmer LS55 luminescence spectrophotometer. Figure taken from PerkinElmer [65].

A.2 PerkinElmer Lambda 650 UV/VIS Spectrophotometer

Figure A.2 shows the schematic of the optical system of the PerkinElmer Lambda 650 UV/VIS spectrophotometer, used to measure the transmission of the scintillators.
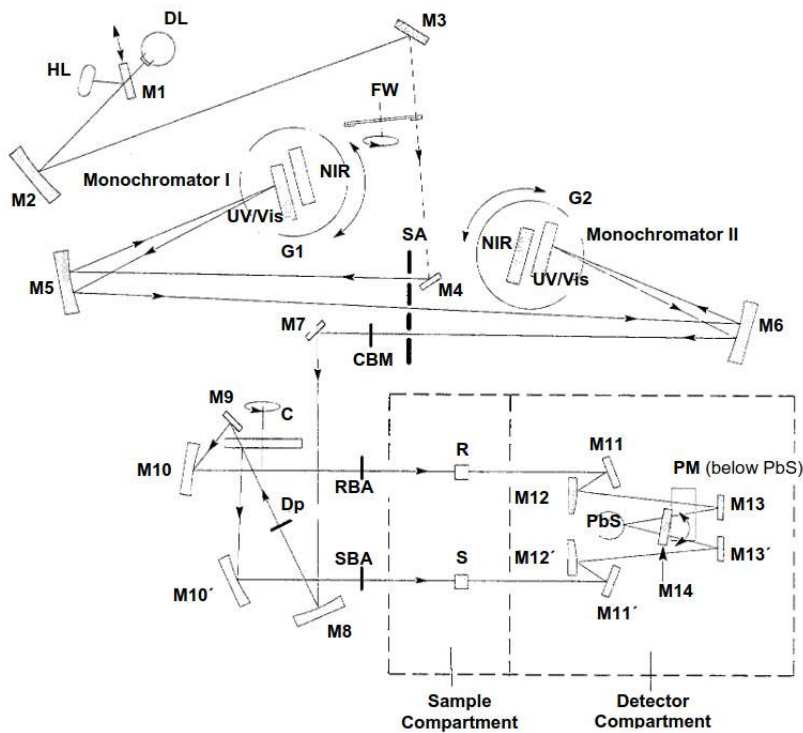
Figure A.2: Schematic of the optical system of the PerkinElmer Lambda 650 UV/VIS sectrophotometer. Figure taken from PerkinElmer [66].

Bibliography

[1] M. Jeitler, 'The upgrade of the CMS trigger system,' *Journal of Instrumentation*, vol. 9, 2014. DOI: `10.1088/1748-0221/9/08/C08002`.

[2] S. Min, H. Kang, B. Seo, J. Cheong, C. Roh, and S. Hong, 'A Review of Nanomaterial Based Scintillators,' *Energies*, vol. 14, p. 7701, 2021. DOI: `0.3390/en14227701`.

[3] R. L. Workman *et al.*, 'Review of Particle Physics,' *PTEP*, vol. 2022, p. 083C01, 2022. DOI: `10.1093/ptep/ptac097`.

[4] E. Groom, N. V. Mokhov, and S. I. Striganov, 'Muon Stopping Power and Range Tables 10 MeV - 100 TeV,' *Atomic Data and Nuclear Data Tables, Vol. 76, No. 2, July 2001*, vol. 76, no. 2, p. 253, 2001. DOI: `LBNL-44742`.

[5] B. Rossi, *High Energy Particles*. New York : Prentice-Hall, 1952.

[6] R. Wigmans, *Calorimetry: Energy Measurement in Particle Physics*. Oxford Science Publications, 2017.

[7] M. Adinolfi and et al., 'The KLOE electromagnetic calorimeter,' *Nuclear Instruments and Methods in Physics Research Section A: Accelerators, Spectrometers, Detectors and Associated Equipment*, vol. 482, no. 1, pp. 364–386, 2002. DOI: `10.1016/S0168-9002(01)01502-9`.

[8] *ATLAS liquid-argon calorimeter: Technical Design Report* (Technical design report. ATLAS). Geneva: CERN, 1996. [Online]. Available: `https://cds.cern.ch/record/331061`.

[9] *CMS Physics: Technical Design Report Volume 1: Detector Performance and Software* (Technical design report. CMS). Geneva: CERN, 2006, There is an error on cover due to a technical problem for some items. [Online]. Available: `https://cds.cern.ch/record/922757`.

[10] M. Hamel, *Plastic Scintillators*. Springer, 2021. [Online]. Available: `https://doi.org/10.1007/978-3-030-73488-6`.

[11] ELJEN Technology, Accessed 2024-01-31. [Online]. Available: `https://eljentechnology.com/`.

[12] P. Lecoq, A. Gektin, and M. Korzhik, *Inorganic Scintillators for Detector Systems*. Springer, 2016.

[13] M. Nikl, 'Scintillation detectors for x-rays,' *Measurement Science and Technology*, vol. 17, no. 4, R37, 2006. DOI: `10.1088/0957-0233/17/4/R01`.

[14] R. H. Pots, E. Auffray, and S. Gundacker, 'Exploiting Cross-Luminescence in BaF2 for Ultrafast Timing Applications Using Deep-Ultraviolet Sensitive HPK Silicon Photomultipliers,' *Frontiers in Physics*, vol. 8, 2020. DOI: `10.3389/fphy.2020.592875`.

[15] G. F. Knoll, *Radiation Detection and Measurements (4th ed.)* John Wiley, 2010.

[16] Y. Shao, 'A new timing model for calculating the intrinsic timing resolution of a scintillator detector,' *Physics in Medicine Biology*, vol. 52, no. 4, p. 1103, 2007. DOI: `10.1088/0031-9155/52/4/016`.

[17] S. Gundacker, R. Martinez Turtos, N. Kratochwil, *et al.*, 'Experimental time resolution limits of modern SiPMs and TOF-PET detectors exploring different scintillators and Cherenkov emission,' *Physics in Medicine Biology*, vol. 65, no. 2, p. 025001, 2020. DOI: `10.1088/1361-6560/ab63b4`.

[18] S. Vinogradov, 'Approximations of coincidence time resolution models of scintillator detectors with leading edge discriminator,' *Nuclear Instruments and Methods in Physics Research Section A: Accelerators, Spectrometers, Detectors and Associated Equipment*, vol. 912, pp. 149–153, 2018. DOI: `10.1016/j.nima.2017.11.009`.

[19] M. Born and E. Wolf, *Basic properties of the electromagnetic field (7th ed.)* Cambridge University Press, 2019.

[20] L. Jacak, P. Hawrylak, and A. Wójs, *Quantum Dots*. Springer, 1998.

[21] F. T. Rabouw and C. de Mello Donega, 'Excited-State Dynamics in Colloidal Semiconductor Nanocrystals,' *Topics in Current Chemistry*, vol. 374, 5 2016. DOI: `10.1007/s41061-016-0060-0`.

[22] V. I. Klimov, *Nanocrystal Quantum Dots (2nd ed.)* CRC Press, 2010.

[23] L. Protesescu, S. Yakunin, M. I. Bodnarchuk, *et al.*, 'Nanocrystals of Cesium Lead Halide Perovskites (CsPbX3, X = Cl, Br, and I): Novel Optoelectronic Materials Showing Bright Emission with Wide Color Gamut,' *Nano Letters*, vol. 15, no. 6, pp. 3692–3696, 2015. DOI: `10.1021/nl5048779`.

[24] F. Haydous, J. M. Gardner, and U. B. Cappel, 'The impact of ligands on the synthesis and application of metal halide perovskite nanocrystals,' *J. Mater. Chem. A*, vol. 9, pp. 23 419–23 443, 41 2021. DOI: `10.1039/D1TA05242J`.

[25] N. Baig, I. Kammakakam, and W. Falath, 'Nanomaterials: a review of synthesis methods, properties, recent progress, and challenges,' *Mater. Adv.*, vol. 2, pp. 1821–1871, 6 2021. DOI: `10.1039/D0MA00807A`.

[26] A. Anand, M. L. Zaffalon, A. Erroi, F. Cova, F. Carulli, and S. Brovelli, 'Advances in Perovskite Nanocrystals and Nanocomposites for Scintillation Applications,' *ACS Energy Letters*, vol. 9, no. 3, pp. 1261–1287, 2024. DOI: `0.1021/acsenergylett.3c02763`.

[27] A. Erroi, S. Mecca, M. L. Zaffalon, *et al.*, 'Ultrafast and Radiation-Hard Lead Halide Perovskite Nanocomposite Scintillators,' *ACS Energy Letters*, vol. 8, no. 9, pp. 3883–3894, 2023. DOI: `10.1021/acsenergylett.3c01396`.

[28] K. Děcká, F. Pagano, I. Frank, *et al.*, 'Timing performance of lead halide perovskite nanoscintillators embedded in a polystyrene matrix,' *J. Mater. Chem. C*, vol. 10, pp. 12 836–12 843, 35 2022. DOI: `10.1039/D2TC02060B`.

[29] C. Chang Lu, M. W. Wright, X. Ma, *et al.*, 'Cesium Oleate Precursor Preparation for Lead Halide Perovskite Nanocrystal Synthesis: The Influence of Excess Oleic Acid on Achieving Solubility, Conversion, and Reproducibility,' *Chemistry of Materials*, vol. 31, no. 1, pp. 62–67, 2019. DOI: `10.1021/acs.chemmater.8b04876`.

[30] M. Imran, P. Ijaz, L. Goldoni, *et al.*, 'Simultaneous Cationic and Anionic Ligand Exchange For Colloidally Stable CsPbBr3 Nanocrystals,' *ACS Energy Letters*, vol. 4, no. 4, pp. 819–824, 2019. DOI: `10.1021/acsenergylett.9b00140`.

[31] K. Děcká, J. Král, F. Hájek, *et al.*, 'Scintillation Response Enhancement in Nanocrystalline Lead Halide Perovskite Thin Films on Scintillating Wafers,' *Nanomaterials*, vol. 12, p. 14, 2021. DOI: `10.3390/nano12010014`.

[32] C. Liu, Z. Li, T. J. Hajagos, D. Kishpaugh, D. Y. Chen, and Q. Pei, 'Transparent Ultra-High-Loading Quantum Dot/Polymer Nanocomposite Monolith for Gamma Scintillation,' *ACS Nano*, vol. 11, no. 6, pp. 6422–6430, 2017. DOI: `10.1021/acsnano.7b02923`.

[33] C. Liu, T. J. Hajagos, D. Kishpaugh, *et al.*, 'Facile Single-Precursor Synthesis and Surface Modification of Hafnium Oxide Nanoparticles for Nanocomposite γ-Ray Scintillators,' *Advanced Functional Materials*, vol. 25, no. 29, pp. 4607–4616, 2015. DOI: `10.1002/adfm.201501439`.

[34] H. Yu, I. Winardi, Z. Han, D. Prout, A. Chatziioannou, and Q. Pei, 'Fast Spectroscopic Gamma Scintillation Using Hafnium Oxide Nanoparticles–Plastic Nanocomposites,' *Chemistry of Materials*, vol. 36, no. 1, pp. 533–540, 2024. DOI: `10.1021/acs.chemmater.3c02631`.

[35] Z. Han, H. Yu, and Q. Pei, 'Fluorene Derivatives for Efficient Prompt Scintillation in Plastic Scintillators,' *ACS Applied Polymer Materials*, vol. 4, no. 6, pp. 4424–4431, 2022. DOI: `10.1021/acsapm.2c00391`.

[36] R. Cala', I. Frank, F. Pagano, *et al.*, 'Sub-100-picosecond time resolution from undoped and Li-doped two-dimensional perovskite scintillators,' *Applied Physics Letters*, vol. 120, no. 24, 2022, 241901. DOI: `10.1063/5.0093606`.

[37] A. Xie, C. Hettiarachchi, F. Maddalena, *et al.*, 'Lithium-doped two-dimensional perovskite scintillator for wide-range radiation detection,' *Communications Materials*, vol. 1, no. 37, pp. 2662–4443, 2020. DOI: `10.1038/s43246-020-0038-x`.

[38] The NanoCal Project, Accessed 2024-01-31. [Online]. Available: `https://aidainnova.web.cern.ch/paving-way-new-generation-fine-sampling-calorimeters-using-nanocomposite-scintillating-materials/`.

[39] AIDAinnova, Accessed 2024-01-31. [Online]. Available: `https://aidainnova.web.cern.ch/`.

[40] M. Doser, E. Auffray, F. M. Brunbauer, *et al.*, 'Quantum Systems for Enhanced High Energy Particle Physics Detectors,' *Front. Phys.*, vol. 10, 2022. DOI: `10.3389/fphy.2022.887738`.

[41] F. Pagano, N. Kratochwil, I. Frank, *et al.*, 'A new method to characterize low stopping power and ultra-fast scintillators using pulsed X-rays,' *Front. Phys.*, vol. 10, 2022.

[42] J. W. Cates, S. Gundacker, E. Auffray, P. Lecoq, and C. S. Levin, 'Improved single photon time resolution for analog SiPMs with front end readout that reduces influence of electronic noise,' *Phys. Med. Biol.*, vol. 63, no. 18, p. 185 022, 2018. DOI: `10.1088/1361-6560/aafd52`.

[43] S. Gundacker, R. Martinez Turtos, E. Auffray, M. Paganoni, and P. Lecoq, 'High-frequency SiPM readout advances measured coincidence time resolution limits in TOF-PET,' *Phys. Med. Biol.*, vol. 64, no. 5, p. 055 012, 2019. DOI: `10.1088/1361-6560/aafd52`.

[44] *E-Series RF 1:1 Transmission Line Transformer*, MABA-007159-000000, Rev. V5, Macom. [Online]. Available: `https://cdn.macom.com/datasheets/MABA-007159-000000.pdf`.

[45] *Silicon Germanium Broadband MMIC Amplifier*, BGA616, Rev. 2.1, Infineon, 2011. [Online]. Available: `https://www.analog.com/media/en/technical-documentation/data-sheets/AD8000.pdf`.

[46] *1.5 GHz Ultrahigh Speed Op Amp*, AD8000, Rev. C, Analog Devices, 2016. [Online]. Available: `https://www.analog.com/media/en/technical-documentation/data-sheets/AD8000.pdf`.

[47] S. Gundacker and A. Heering, 'The silicon photomultiplier: fundamentals and applications of a modern solid-state photon detector,' *Physics in Medicine Biology*, vol. 65, no. 17, 17TR01, 2020. DOI: `10.1088/1361-6560/ab7b2d`.

[48] F. Acerbi and S. Gundacker, 'Understanding and simulating SiPMs,' *Nuclear Instruments and Methods in Physics Research Section A: Accelerators, Spectrometers, Detectors and Associated Equipment*, vol. 926, pp. 16–35, 2019, Silicon Photomultipliers: Technology, Characterisation and Applications. DOI: `10.1016/j.nima.2018.11.118`.

[49] *Hamamatsu s13360*, S13360, Accessed 2024-01-31, Hamamatsu. [Online]. Available: `https://www.hamamatsu.com/content/dam/hamamatsu-photonics/sites/documents/99_SALES_LIBRARY/ssd/s13360_series_kapd1052e.pdf`.

[50] *Perkinelmer lambda 650 uv/vis spectrophotometer*, Accessed 2024-01-31. [Online]. Available: `https://resources.perkinelmer.com/lab-solutions/resources/docs/BRO_Lambda950850650Americas.pdf`.

[51] S. Gundacker, R. Martinez Turtos, E. Auffray, and P. Lecoq, 'Precise rise and decay time measurements of inorganic scintillators by means of X-ray and 511 keV excitation,' *Nuclear Instruments and Methods in Physics Research Section A: Accelerators, Spectrometers, Detectors and Associated Equipment*, vol. 891, pp. 42–52, 2018. DOI: `10.1016/j.nima.2018.02.074`.

[52] S. Gundacker, E. Auffray, K. Pauwels, and P. Lecoq, 'Measurement of intrinsic rise times for various L(Y)SO and LuAG scintillators with a general study of prompt photons to achieve 10 ps in TOF-PET,' *Phys. Med. Biol.*, vol. 61, no. 7, p. 2802, 2016. DOI: `10.1088/0031-9155/61/7/2802`.

[53] I. Villa, L. P. Procházková, E. Miháková, *et al.*, 'First investigation of the morphological and luminescence properties of HfO2 nanoparticles synthesized by photochemical synthesis,' *CrystEngComm*, vol. 25, pp. 4345–4354, 30 2023. DOI: `10.1039/D3CE00320E`.

[54] F. Maddalena, L. Tjahjana, A. Xie, *et al.*, 'Inorganic, Organic, and Perovskite Halides with Nanotechnology for High–Light Yield X- and γ-ray Scintillators,' *Crystals*, vol. 9, no. 2, 2019. DOI: `10.3390/cryst9020088`.

[55] S. Ritt, 'Design and performance of the 6 ghz waveform digitizing chip drs4,' in *2008 IEEE Nuclear Science Symposium Conference Record*, 2008, pp. 1512–1515. DOI: `10.1109/NSSMIC.2008.4774700`.

[56] The Birth of NanoCal, Accessed 2024-01-31. [Online]. Available: `https://ep-news.web.cern.ch/content/birth-nanocal/`.

[57] G. S. Atoian, G. I. Britvich, S. K. Chernichenko, *et al.*, 'An improved Shashlyk calorimeter,' *Nuclear Instruments and Methods in Physics Research Section A: Accelerators, Spectrometers, Detectors and Associated Equipment*, vol. 584, no. 2, pp. 291–303, 2008. DOI: `10.1016/j.nima.2007.10.022`.

[58] Kuraray, Accessed 2024-01-31. [Online]. Available: `https://www.kuraray.com/`.

[59] M. Gandini, I. Villa, M. Beretta, *et al.*, 'Efficient, fast and reabsorption-free perovskite nanocrystal-based sensitized plastic scintillators,' *Nature Nanotechnology*, vol. 15, pp. 462–468, 6 2020. DOI: `10.1038/s41565-020-0683-8`.

[60] M. Moulson , *et al.*, 'AIDAinnova – WP8 Face-to-Face Meeting,' Accessed 2024-01-24. [Online]. Available: `https://indico.cern.ch/event/1344030/#4-task-831`.

[61] S. Ceravolo, F. Colao, C. Curatolo, *et al.*, 'Crilin: A CRystal calorImeter with Longitudinal InformatioN for a future Muon Collider,' *Journal of Instrumentation*, vol. 17, no. 9, P09033, 2020. DOI: `10.1088/1748-0221/17/09/P09033`.

[62] C. Cantone, S. Carsi, S. Ceravolo, *et al.*, 'Beam test, simulation, and performance evaluation of PbF2 and PWO-UF crystals with SiPM readout for a semi-homogeneous calorimeter prototype with longitudinal segmentation,' *Frontiers in Physics*, vol. 11, 2023. DOI: `10.3389/fphy.2023.1223183`.

[63] J. Perego, C. X. Bezuidenhout, I. Villa, *et al.*, 'Highly luminescent scintillating hetero-ligand MOF nanocrystals with engineered Stokes shift for photonic applications,' *Nature Communications*, vol. 13, no. 3504, 2022. DOI: `10.1038/s41467-022-31163-0`.

[64] A. Erroi, F. Carulli, F. Cova, *et al.*, 'Ultrafast and Radiation-Hard Lead Halide Perovskite Nanocomposite Scintillators,' *under review in ACS Energy Letters*, 2024.

[65] *User guide of the perkinelmer ls55 luminescence spectrometer*, Accessed 2024-01-31. [Online]. Available: `https://www.s4science.at/wordpress/wp-content/uploads/2019/04/LS-55-Users-Guide.pdf`.

[66] *Hardware guide of the perkinelmer lambda 650 uv/vis spectrophotometer*, Accessed 2024-01-31. [Online]. Available: `https://cmdis.rpi.edu/sites/default/files/UVVis-PerkinElmer-Lambda950-HardwareGuide.pdf`.

List of Figures

List of Tables

List of Abbreviations

APD	Avalanche photodiode
ATLAS	A Toroidal LHC Apparatus
BaF_2	Barium fluoride (BaF_2)
BD	Breakdown
BGO	Bismuth germanium oxide ($Bi_4Ge_3O_{12}$)
BMEP	Bis[2-(methacryloyloxy)ethyl] phosphate ($C_{15}H_{18}N_2O_6$)
BTF	DAFNE Beam-Test Facility
Ca	Calcium
CdS	Cadmium sulfide (CdS)
CdSe	Cadmium selenide (CdSe)
CdZnS	Cadmium-doped zinc sulfide (CdZnS)
Ce	Cerium
CERN	European Organization for Nuclear Research
CFD	Constant fraction discrimination
CINTRA	CNRS-International-NTU-Thales Research Alliance
CMS	Compact Muon Solenoid
$CsPbBr_3$	Cesium lead bromide ($CsPbBr_3$)
$CsPb(BrCl)_3$	Cesium lead bromide/chloride ($CsPb(BrCl)_3$)
CTR	Coincidence time resolution
CTU	Czech Technical University in Prague, Czech Republic
DAQ	Data acquisition system
DDAB	Didodecyldimethylammonium bromide ($C_{26}H_{56}BrN$)
DTR	Detector time resolution
ECAL	Electromagnetic calorimeter
EJ232	Fast timing plastic scintillator from ELJEN Technology
FBTF	4,7-bis2-9,9-bis[(2-ethylhexyl)fluorenyl]-2,1,3-benzothiadiazole
FRET	Förster resonance energy transfer
FWHM	Full width at half maximum
HCAL	Hadronic calorimeter
HEP	High energy physics
HfO_2	Hafnium oxide or hafnia (HfO_2)
HI	Hot injection
HPM	Hybrid photomultiplier tube
IHEP	Institute for High Energy Physics, Protvino, Russia
INFN	Laboratori Nazionali di Frascati
IRF	Impulse response function
KLOE	K^0_LLOng Experiment
LARP	Ligand-assisted reprecipitation
LHC	Large hadron collider
LED	Light-emitting diodes
Li	Lithium
LO	Light output
LSO	Lutetium oxyorthosilicate (Lu_2SiO_5)
LTE	Light transfer efficiency

LY	Light yield
LYSO	Lutetium yttrium oxyorthosilicate ($Lu_{2(1-x)}Y_{2x}SiO_5$)
MCP	Microchannel plate detector
MIP	Minimum ionizing particle
MPPC	Multi-pixel photon counter
NC	Nanocrystal
NUV-HD	Near ultraviolet high density
OA	Oleic acid ($C_{18}H_{34}O_2$)
OLAM	Oleylamine ($C_{18}H_{37}N$)
PBD	2-(4-tert-butylphenyl)-5-(4-biphenyl)-1,3,4-oxadiazole ($C_{24}H_{22}N_{20}$)
PCB	Printed circuit board
PDE	Photon detection efficiency
PEA	Bis(phenylethylammonium) lead bromide ($C_{16}H_{24}N_2$)
PET	Positron emission tomography
PLA	(poly)laurylmeth-acrylate ($[C_{16}H_{30})_2]n$)
PL	Photoluminescence
PMT	Photomultiplier tube
PMMA	Poly(methylmeth)acrylate ($[C_5H_8)_2]n$)
POPOP	1,4-Bis(5-phenyl-2-oxazolyl)benzene ($C_{24}H_{16}N_2O_2$)
PS	Proton synchrotron
PS	Polystyrene
PTP	P-terphenyl ($C_{18}H_{14}$)
PTS	Photon travel spread
PVT	Poly(vinyltoluene) ($[CH_2CH(C_6H_4CH_3)]n$)
PWO	Lead tungstate ($PbWO_4$)
QC	Quantum confinement
QD	Quantum dot
QE	Quantum efficiency
R&D	Research and development
SiPM	Silicon photomultiplier
SMD	Surface mount device
SPAD	Single photon avalanche diode
SPTR	Single photon time resolution
SPS	Super proton synchrotron
TCSPC	Time correlated single photon counting
TDC	Time-to-Digital-Converter
TOF	Time of flight
UCLA	University of California, Los Angeles, USA
UNIMIB	University of Milano-Bicocca, Milan, Italy
UV	Ultraviolet
VIS	Visible
WLS	Wavelength shifting
wt	Weight
ZnS	Zinc sulfide (ZnS)
0 D	Zero-dimensional

1 D	One-dimensional
2 D	Two-dimensional
3 D	Three-dimensional

List of Publications

Parts of this thesis are published in the following reviewed articles:

Andrea Erroi, Francesco Carulli, Francesca Cova, Isabel Frank, Matteo Zaffalon, Jordi Llusar, Sara Mecca, Alessia Cemmi, Ilaria Di Sarcina, Francesca Rossi, Luca Beverina, Francesco Meinardi, Ivan Infante, Etiennette Auffray, Sergio Brovelli, "Ultrafast nanocomposite scintillators based on Cd-enhanced CsPbCl3 nanocrystals in polymer matrix", under review in *ACS Energy Lett.*, 2024.

A. Erroi, S. Mecca, M. Zaffalon, I. Frank, F. Carulli, A. Cemmi, I. Di Sarcina, D. Debellis, F. Rossi, F. Cova, K. Pauwels, M. Mauri, J. Perego, V. Pinchetti, A. Comotti, F. Meinardi, A. Vedda, E. Auffray, L. Beverina and S. Brovelli, "Ultrafast and Radiation-Hard Lead Halide Perovskite Nanocomposite Scintillators", *ACS Energy Lett.*, 8, 9, 3883–3894, 2023.

C. Cantone, S. Carsi, S. Ceravolo, E. Di Meco, E. Diociaiuti, I. Frank, S. Kholodenko, S. Martellotti, M. Mirra, P. Monti-Guarnieri, M. Moulson, D. Paesani, M. Prest, M. Romagnoni, I. Sarra, F. Sgarbossa, M. Soldani and E. Vallazza, "Beam test, simulation, and performance evaluation of PbF_2 and PWO-UF crystals with SiPM readout for a semi-homogeneous calorimeter prototype with longitudinal segmentation", *Front. Phys.*, 11, 2023.

I. Villa, L. Prouzová Procházková, E. Mihóková, V. Babin, R. Král, P. Zemenová, A. Falvey, V. Čuba, M. Salomoni, F. Pagano, R. Calà, I. Frank, E. Auffray and M. Nikl, "First investigation of the morphological and luminescence properties of HfO_2 nanoparticles synthesized by photochemical synthesis", *CrystEngComm*, 25, 4345-4354, 2023.

F. Pagano, N. Kratochwil, I.Frank, S. Gundacker, M. Paganoni, M. Pizzichemi, M. Salomoni and E. Auffray, "A new method to characterize low stopping power and ultra-fast scintillators using pulsed X-rays", *Front. Phys.*, 10, 2022.

K. Děckà, F. Pagano, I. Frank, N. Kratochwil, E. Mihóková, E. Auffray and V. Čuba, "Timing performance of lead halide perovskite nanocrystals embedded in polystyrene matrix", *J. Mater. Chem. C*, 10, 12836-12843, 2022.

M. Doser, E. Auffray, F. Brunbauer, I. Frank, H. Hillemanns, G. Orlandini and G. Kornakov, "Quantum systems for enhanced high energy particle physics detector", *Front. Phys.*, 10, 2022.

R. Cala', I. Frank, F. Pagano, F. Maddalena, C. Dang, M. D. Birowosuto and E. Auffray, "Sub-100-picosecond time resolution from undoped and Li-doped two-dimensional perovskite scintillators", *Appl. Phys. Lett.*, 120, 241901, 2022.

J. Perego, Charl X. Bezuidenhout, I. Villa, F. Cova, R. Crapanzano, I. Frank, F. Pagano, N. Kratochwill, E. Auffray, S. Bracco, A. Vedda, C. Dujardin, P. E. Sozzani, F. Meinardi, A. Comotti and A. Monguzzi, "Highly luminescent scintillating hetero-ligand MOF nanocrystals with engineered Stokes shift for photonic applications", *Nature Communications*, 13, 3504, 2021.

Awards

IEEE Valentin T. Jordanov Grant, IEEE NSS MIC RTSD Conference 2023